

**TRANSPARENT CIRCULARLY POLARIZED ANTENNA FOR
AUTOMOTIVE APPLICATIONS**

by

Alireza Gharaati Jahromi

A thesis submitted in partial fulfillment of the requirements for the degree of

Master of Science

in

Electromagnetics and Microwaves

Department of Electrical and Computer Engineering
University of Alberta

© Alireza Gharaati Jahromi, 2021

Abstract

The purpose of this dissertation is to generate better solutions for the existing problems in the wireless communications and navigation systems by designing antennas with special characteristics such as circular polarization (CP), tilted beam, transparency, high gain, front to back ratio (FBR) and so forth, suitable for inclined surfaces especially in automotive applications.

The first chapter provides an overview of the existing problem and a literature review about the previous studies, containing global navigation satellite system (GNSS), and especially global positioning systems (GPS) antennas and their characteristics, circularly polarized antennas and their advantages over the linearly polarized (LP) ones, antennas with tilted beams and some examples of such antennas, and also transparent antennas and different methods for reaching transparency. As the final part of this chapter, the aims of the current research and the thesis organization will be presented.

Chapter 2 outlines a wideband circularly polarized antenna with a simple geometry, which covers the GNSS/GPS frequency bands. The antenna can be used for GNSS/GPS applications, but it lacks some characteristics that are needed for such applications, which are discussed both in the research aims and the conclusion of the chapter in more details.

In chapter 3, a dual-band circularly polarized antenna is proposed for GNSS/GPS applications. The impedance and axial ratio (AR) bandwidths cover the entire GNSS/GPS bands. Although the performance of this antenna, especially in terms of front to back ratio (FBR), for GNSS/GPS applications has been improved compared to the one discussed in Chapter 2, still some additional characteristics such as tilted beam and transparency are needed to be added to these types of GNSS antennas for the end goal.

In chapters 4 and 5, two novel wideband transparent circularly polarized antennas with tilted beams are proposed. The antennas cover the entire GNSS frequency bands in terms of both impedance and axial ratio bandwidths. The beams of the antennas are tilted for about 30 degrees, suitable to be mounted on the windshield of vehicles. A transparent reflector has been introduced and designed in order to be placed under the antenna on the glove compartment or dashboard of the vehicle in order to increase the FBR.

Finally, in chapter 6, a brief discussion about possible future works is presented.

Additional information and simulation results such as the characteristic mode analysis (CMA), conformability results on curved surfaces, tolerance, and upper and lower hemisphere energy division for proposed antennas of chapter 4 and 5 have been presented in the appendix.

Preface

This thesis is an original work by Alireza Gharaati Jahromi submitted in partial fulfillment of the requirements for the degree of Master of Science.

For chapter 1, I was responsible for the literature review with the assistance of M.S. Ghaffarian.

Chapter 2 of this thesis has been published as A. Gharaati, M.S. Ghaffarian, H. Saghlatoon, M. Behdani, and R. Mirzavand, “A low-profile wideband circularly polarized CPW slot antenna,” *AEU-International Journal of Electronics and Communications*, vol. 129, p. 153534, 2021. I was responsible for designing the antenna, doing analysis, writing the manuscript, fabrication, and measurement of the antenna. M.S. Ghaffarian, H. Saghlatoon, and M. Behdani assisted with the fabrication, measurements, and revisions. R. Mirzavand assisted with generating ideas and the revisions, and had the supervisory role throughout the work.

Chapter 4 of this thesis has been accepted for publication as A. Gharaati, M.S. Ghaffarian, and R. Mirzavand, “Transparent Wideband Circularly Polarized GNSS Antenna for Vehicular Applications” in *IEEE Access Journal*. I was responsible for designing the antenna, doing analysis, writing the manuscript, fabrication, and measurement of the antenna. M.S. Ghaffarian assisted with the fabrication, measurements, and revisions. R. Mirzavand assisted with generating ideas and the revisions, and had the supervisory role throughout the work.

For chapters 3 and 5, I was responsible for designing the antennas, doing the analysis, writing, fabrications, and measurements. M.S. Ghaffarian assisted with the fabrication, measurements, and revisions. R. Mirzavand assisted with generating ideas and the revisions, and had the supervisory role throughout the work.

Acknowledgments

First of all, I would like to express my sincere gratitude to Professor Pedram Mousavi, my former supervisor, who passed away in a tragic plane crash with his lovely family, Professor Mojgan Daneshmand and their daughters. His supports and encouragements always motivated me to move on and forward my career. Thank you Pedram for everything.

I would like to express my special thanks to my technical supervisor, Dr. Rashid Mirzavand for his endless support, guidance and patience throughout my studies. His help and assistance towards my career were more than a supervisory role.

I would like to express my special thanks to Dr. Mohammad Saeid Ghaffarian whose continuous and kind guidance during my works paved the way for accomplishing this work.

My special thanks goes to Prof. Yindi Jing and Prof. Ivan Fair for their support and taking the supervisory role after my former supervisor.

I would take this opportunity to thank all my group members, colleagues and friends for their help and assistance throughout my program.

And last but not the least, my special appreciation goes to my beloved family for all their supports and motivations throughout my life.

Table of Contents

1.	Chapter 1: Introduction	1
1.1	Overview	1
1.2	Literature Review.....	2
1.2.1	GNSS/GPS Antennas.....	2
1.2.2	Circularly Polarized Antennas	6
1.2.3	Tilted Beam Antennas.....	8
1.2.4	Transparent Antennas	9
1.3	Research Aims.....	13
2.	Chapter 2: A Low-profile Wideband Circularly Polarized CPW Slot Antenna	16
2.1	Introduction	16
2.2	Antenna Design and Configuration.....	17
2.2.1	Antenna Development Stages.....	17
2.2.2	CP Mechanism	22
2.2.3	Redesigning the antenna	24
2.2.4	Parametric Study.....	25
2.3	Simulation and Measurement Results	29
2.4	Conclusion.....	34
3.	Chapter 3: Compact Dual-Band Circularly Polarized Antenna with Octagonal-Shaped Slotted Reflector for GNSS Applications	35
3.1	Introduction	35
3.2	Antenna Geometry and Analysis.....	36
3.2.1	Antenna Configuration.....	36
3.2.2	Antenna Analysis	36
3.2.3	Parametric Study.....	41

3.3	Fabricated Prototype and Experimental Results	45
3.4	Conclusion.....	48
4.	Chapter 4: Wideband Transparent Circularly Polarized Rectangular Slot GNSS Antenna for Vehicular Applications	49
4.1	Introduction	49
4.2	Configuration and Development of the Proposed Antenna	50
4.2.1	Antenna Geometry	50
4.2.2	Antenna Development Stages	53
4.3	Antenna Analysis and Transparent Reflector.....	55
4.3.1	CP Mechanism	55
4.3.2	Antenna Beam.....	56
4.3.3	Parametric Study.....	58
4.3.4	Transparent Reflector.....	61
4.4	Fabrication of Prototypes and Discussion of Simulation and Measurement Results	
	63	
4.4.1	Fabrication Process	63
4.4.2	Results and Discussion	64
4.4.3	Comparison with Previous Works in Literature	69
4.4.4	Results on a Car Model.....	69
4.4.5	Effects of Mesh Defects on the Performance of the Antenna.....	72
4.5	Conclusion.....	74
5.	Chapter 5: Wideband Transparent Circularly Polarized Spiral Slot Antenna with Tilted Beam for Automotive Applications	75
5.1	Introduction	75
5.2	Antenna Configuration and Development.....	76
5.2.1	Antenna Geometry	76

5.2.2	Antenna Development Stages	77
5.3	Antenna Development Analysis and CP mechanism.....	81
5.3.1	Transparent Reflector.....	83
5.3.2	Parametric Study.....	84
5.3.3	Mesh Grid and Optical Transparency	87
5.4	Fabrication and Measurements.....	87
5.4.1	Prototype and Manufacturing Process	87
5.4.2	Study of Measurement Results	88
5.4.3	Results on a Car Model.....	91
5.4.4	Comparison with Previous Works	94
5.5	Conclusion.....	96
6.	Future works	97
	Bibliography	99
7.	Appendices.....	109
7.1	Characteristic Mode Analysis of the Rectangular Slot Antenna.....	109
7.2	Characteristic Mode Analysis of the Spiral Slot Antenna.....	117
7.3	Conformability Results	122
7.3.1	Rectangular Slot Antenna	122
7.3.2	Spiral Slot Antenna.....	125
7.4	Tolerance.....	128
7.4.1	Investigation of the Effects of Different Thicknesses and Different Substrate Permittivity Values on Rectangular Slot Antenna	128
7.4.2	Investigation of the Effects of Different Thicknesses and Different Substrate Permittivity Values on Spiral Slot Antenna	129
7.5	Upper and Lower Hemispheres Energy Division	130

List of Tables

Table 2-1: Comparison between some wideband CP antennas in literature and the proposed CPW slot antenna.....	33
Table 3-1: Parameters of Antenna Configuration (values in mm).....	43
Table 3-2: Comparison between dual-band CP antennas in literature and the proposed antenna	44
Table 4-1: Comparison between some single, dual, and wideband antennas in literature and the proposed antenna.....	70
Table 5-1: Comparison between some single, dual, and wideband antennas in literature and the proposed antenna.....	95
Table 7-1: Effects of different thicknesses on rectangular slot antenna	128
Table 7-2: Effects of different dielectric constants on rectangular slot antenna.....	128
Table 7-3: Effects of different thicknesses on spiral slot antenna	129
Table 7-4: Effects of different dielectric constants on spiral slot antenna.....	129
Table 7-5: Amount of energy percentage in upper and lower hemispheres at L2 and L1 center frequency bands.	130

List of Figures

Figure 1.1: GNSS navigational frequency bands (taken from [4]).....	2
Figure 1.2: A simple metal mesh pattern with enlarged section of a single mesh element	11
Figure 2.1: Proposed antenna structure, (a) top view, (b) side view. $h = 0.64$, $w = 4$, $w_1 = 3.65$, $g = 1.35$, $L_{cpw1} = 17.53$, $L_{cpw2} = 22$, $W_{s1} = 27.4$, $W_{s2} = 17.8$, $W_{s3} = 43.5$, $L_{s1} = 14.8$, $L_{s2} = 35.3$, $L_{s3} = 33.2$, $X_{s1} = 11.2$, $X_{s2} = 14$, $Y_{s1} = 41.43$, and $Y_{s2} = 22.37$ (units are in mm).	17
Figure 2.2: Evolution stages of the proposed antenna, (a) Antenna 1, (b) Antenna 2, (c) Antenna 3, (d) Proposed antenna.	18
Figure 2.3: Simulation results for four evolution stages of the proposed antenna, (a) Reflection coefficient, (b) AR.....	19
Figure 2.4: Analysis of antenna 3, (a) the way in which antenna 3 has been cut for obtaining corresponding reflection coefficients, (b) equivalent circuit of antenna 3 showing the RLC model of the slot.....	21
Figure 2.5: Reflection coefficient of antenna 3 using equivalent circuit model and full wave simulation.....	21
Figure 2.6: Magnitude ratio and phase difference of orthogonal field components E_x and E_y , (a) magnitude ratio, (b) phase difference (the unit is in degree).	22
Figure 2.7: The surface current distribution of the proposed antenna at 900 MHz, (a) 0° , (b) 90° , (c) 180° , (d) 270°	23
Figure 2.8: The surface current distribution of the proposed antenna at 1.6 GHz, (a) 0° , (b) 90° , (c) 180° , (d) 270°	24
Figure 2.9: Simulated redesigned antennas for different scaled sizes, (a) S_{11} , (b) Axial Ratio.....	25
Figure 2.10: Parametric analysis of the proposed antenna in terms of reflection coefficient and axial ratio.....	27
Figure 2.11: The flowchart design procedure of the proposed antenna.....	28
Figure 2.12: Fabrication and measurement of the proposed antenna, (a) photograph of the fabricated antenna prototype, (b) measurement of the antenna in an anechoic chamber.	29

Figure 2.13: Simulated and measured parameters of the proposed antenna, (a) S_{11} , (b) Axial Ratio at $\theta = 0^\circ$ and $\phi = 0^\circ$.	30
Figure 2.14: Simulated and measured RHCP gain of the proposed antenna.	30
Figure 2.15: Simulated and measured normalized radiation patterns of the proposed antenna for two different planes of $\phi = 0^\circ$ and $\phi = 90^\circ$ at, (a) 1.6 GHz, (b) 2.4 GHz, (c) 3.1 GHz.	32
Figure 3.1: Geometry of the proposed antenna, (a) top view, (b) bottom view, (c) enlarged feeding section, (d) side view.	37
Figure 3.2: Reflection coefficient, axial ratio, and FBR of different states of the antennas, (a) reflection coefficient, (b) axial ratio, (c) FBR.	38
Figure 3.3: Magnitude ratio and phase difference of orthogonal field components E_x and E_y for different states, (a) magnitude ratio, (b) phase difference (the unit is in degree)...	39
Figure 3.4: The surface current distribution of the proposed antenna at 1.227 GHz, (a) 0° , (b) 90° , (c) 180° , (d) 270° .	40
Figure 3.5: The electric field distribution at the octagonal-shaped slot from the top view at 1.227 GHz, (a) 0° , (b) 90° , (c) 180° , (d) 270° .	41
Figure 3.6: Simulation results of the proposed antenna for different values of "e", (a) reflection coefficient, (b) axial ratio.	42
Figure 3.7: Simulation results of RHCP and LHCP gain of the proposed antenna for different values of " W_s " at $\theta = 0^\circ$, $\phi = 0^\circ$ and $\theta = 180^\circ$, $\phi = 0^\circ$ respectively.	43
Figure 3.8: Fabricated prototype and measurement of the proposed antenna, (a) isometric view, (b) bottom view, (c) measurement of the proposed antenna in anechoic chamber.	45
Figure 3.9: Simulation and measurement results of reflection coefficient and axial ratio the proposed antenna.	46
Figure 3.10: Simulation and measurement results of RHCP and LHCP gain of the proposed antenna at $\theta = 0^\circ$, $\phi = 0^\circ$ and $\theta = 180^\circ$, $\phi = 0^\circ$, respectively along with the FBR.	46
Figure 3.11: Normalized radiation patterns of the proposed antenna in two different frequencies of GPS L2 and L1 bands at two different planes of $\phi = 0^\circ$ and $\phi = 90^\circ$.	47
Figure 4.1: Geometry of the proposed antenna, (a) top view (b) side view. $h=1$ (dimensions in mm).	51

Figure 4.2: Enlarged sections of the proposed antenna, (a) section A (b) section B (c) section C (d) section D (e) enlarged section of feedline. $W=63$, $L=17$ (all dimensions are in mm)..... 52

Figure 4.3: Definition of the new coordinate system while the antenna is placed on the windshield..... 52

Figure 4.4: Antenna evolution stages, (a) Ant1 (b) Ant2 (c) Ant3 (d) Ant4 (e) proposed antenna 54

Figure 4.5: Reflection coefficient and axial ratio of Ant1-Ant4 and the proposed antenna, (a) reflection coefficient (b) axial ratio at $\theta' = 0^\circ$, $\phi = 0^\circ$ 55

Figure 4.6: Magnitude ratio and phase difference (PD) of orthogonal field components E_x and E_y , (a) magnitude ratio, (b) phase difference (PD unit is in degree)..... 55

Figure 4.7: Electric fields distribution of the proposed antenna at four different time instants at GPS L2 center frequency (1.227 GHz), (a) 0° (b) 90° (c) 180° (d) 270° (e) the way proposed antenna is observed for the electric fields distribution. 56

Figure 4.8: RHCP beam direction of the diagonal-slot antenna for different values of "P" in the primary coordinate system at $\phi = 0^\circ$ for two different GPS frequency bands..... 57

Figure 4.9: RHCP beam direction of the diagonal-slot antenna for different frequencies in the primary coordinate system at two different planes, (a) $\phi = 0^\circ$ (b) $\phi = 90^\circ$ 58

Figure 4.10: Simulation of Ant4 for different values of "L", (a) reflection coefficient (b) axial ratio. 60

Figure 4.11: Simulation of Ant4 for different values of "W", (a) reflection coefficient (b) axial ratio. 60

Figure 4.12: RHCP radiation patterns of the proposed antenna for different scale factors in the primary coordinate system at 1.575 GHz at $\phi = 0^\circ$ 61

Figure 4.13: Transparent reflector and the way it is placed under the proposed antenna, (a) transparent reflector using mesh grid (b) one mesh element (c) isometric view of the reflector under the antenna (d) side view of the reflector and antenna (units in mm)..... 63

Figure 4.14: Fabrication and measurement of the proposed antenna, (a) fabrication process (b) proposed antenna before integration (c) fabricated transparent reflector (d) fabricated antenna on the inclined stage (e) measurement of the fabricated antenna in anechoic

chamber (f) measurement of reflection coefficient of the proposed antenna on the windshield of vehicle.	65
Figure 4.15: Simulation and measurement results of the proposed antenna, (a) reflection coefficient (b) axial ratio at $\theta' = 0^\circ$ and $\phi = 0^\circ$ (while mounted on the inclined stage).65	65
Figure 4.16: Normalized radiation pattern of the proposed antenna while placed on the inclined stage in the new coordinate system at two different frequencies, (a) 1.227 GHz (b) 1.575 GHz.	67
Figure 4.17: Normalized radiation pattern of the proposed antenna while placed on the inclined stage with the reflector below the antenna, in the new coordinate system at two different frequencies, (a) 1.227 GHz (b) 1.575 GHz.	68
Figure 4.18: Simulation and measurement results of RHCP gain of the proposed antenna with and without the reflector at $\theta' = 0^\circ$ and $\phi = 0^\circ$	68
Figure 4.19: Proposed antenna with the reflector on a car model for re-simulation, (a) front view (b) isometric view (c) side view.	71
Figure 4.20: Simulated normalized radiation pattern of the proposed antenna on the car model at two different frequencies with the reflector under the antenna, (a) 1.227 GHz (b) 1.575 GHz.	71
Figure 4.21: Two different states showing different types of defects on the mesh grid shown in red dash lines, (a) state 1 (b) state 2.	72
Figure 4.22: Simulation results of the proposed antenna and two states in which defects exist in the mesh layer, (a) reflection coefficient (b) axial ratio (c) RHCP gain at $\theta' = 0^\circ$	73
Figure 5.1: The configuration of the proposed antenna and its different parts, (a) final design, (b) enlarged view of the middle section (c) one mesh element (d) enlarged view of the feedline (all dimensions in mm).	77
Figure 5.2: Two initial steps for realizing the proposed antenna, (a) spiral arms of the slot spiral (b) the spiral slot on the conductive layer after the rotation (c) side view of the antenna. $h = 1$, $r_0 = 15.6$, $d = 25.3$ (units are in mm), and $Start1 = 1.1$, $Start2 = -4.3$, $End1 = 3.2$, $End2 = 3.1$ (units are in rad).	78

Figure 5.3: Evolution steps of the proposed antenna and the enlarged L-shaped radiator, (a) Ant1 (b) Ant2 (c) Ant3 (d) proposed antenna. $W=170$, $L=122$, $L_{s1}=68$, $L_{s2}=17.6$, $W_{s1}=24.2$, $W_{s2}=14.5$, $W_{s3}=12$, $W_f=0.8$ (units are in mm). 79

Figure 5.4: The proposed antenna while placed on the windshield introducing a new coordinate system..... 80

Figure 5.5: Reflection coefficient and axial ratio of Ant1-3 and the proposed antenna, (a) reflection coefficient, (b) axial ratio. 80

Figure 5.6: Magnitude ratio and phase difference of orthogonal field components E_x and E_y , (a) magnitude ratio (b) phase difference (the unit is in degree). 82

Figure 5.7: Surface currents distribution of Ant3 at four different time instants at 1.227 GHz, (a) 0° (b) 90° (c) 180° (d) 270° (e) observation of the proposed antenna for the electric fields distribution. 83

Figure 5.8: Surface currents distribution of Ant3 at four different time instants at 1.575 GHz, (a) 0° (b) 90° (c) 180° (d) 270° (e) observation of the proposed antenna for the electric fields distribution. 83

Figure 5.9: The proposed reflector, (a) full reflector (b) transparent reflector (c) width and length of mesh elements used in transparent reflector. $m=100$, $p=0.1$, $q=5.4$ (all dimensions in mm). 85

Figure 5.10: Arrangement of the reflector and the proposed antenna, (a) isometric view (b) front view (c) bottom view (all dimensions in mm). 85

Figure 5.11: Simulated results of the proposed antenna with different values of $End1 \& 2$, (a) reflection coefficient (b) axial ratio. 86

Figure 5.12: Simulated results of the proposed antenna with different values of “ a ”, (a) reflection coefficient (b) axial ratio. 86

Figure 5.13: Fabricated prototype and measurements, (a) fabrication process (b) fabricated prototype before integration (c) inclined stage with fabricated reflector (d) proposed antenna measurement in anechoic chamber (e) reflection coefficient measurement of the proposed antenna while placed on the windshield..... 89

Figure 5.14: Simulation and measurement results of the proposed antenna in terms of reflection coefficient and axial ratio, (a) simulation and measurement results of the

reflection coefficient in lab and on the inclined windshield (b) axial ratio, while it is mounted on the inclined stage without the reflector at $\theta' = 0^\circ$, $\phi = 0^\circ$	90
Figure 5.15: Normalized radiation pattern of the proposed antenna while mounted on the inclined stage without the reflector at (a) 1.227 GHz, (b) 1.575 GHz.....	92
Figure 5.16: Normalized radiation pattern of the proposed antenna while mounted on the inclined stage with the reflector at (a) 1.227 GHz , (b) 1.575 GHz.....	93
Figure 5.17: RHCP gain of the proposed antenna at $\theta' = 0^\circ$, $\phi = 0^\circ$ while it has been mounted on the stage, with and without the reflector.	93
Figure 5.18: Proposed antenna mounted on a car model for re-simulation, (a) isometric view, (b) side view.....	93
Figure 5.19: Normalized radiation pattern of the proposed antenna while mounted on the windshield of the car model backed by the reflector at (a) 1.227 GHz, (b) 1.575 GHz. ..	94
Figure 7.1: Characteristic mode analysis of Ant2 (a) modal significance (b) characteristic angle (c) surface current and directivity of modes 2 and 4 ($J_2 + J_4$) at 1.75 GHz (d) surface current and directivity of modes 4 and 6 ($J_4 + J_6$) at 2.35 GHz.	112
Figure 7.2: Characteristic mode analysis of Ant3, (a) modal significance (b) characteristic angle (c) surface current and directivity of mode 2 and 4 ($J_2 + J_4$) at 1.75 GHz, (d) surface current and directivity of mode 3 and 6 ($J_3 + J_6$) at 2.2 GHz (e) surface current and directivity of mode 4 and 6 ($J_4 + J_6$) at 2.45 GHz.....	114
Figure 7.3: Surface current of three different modes of Ant3 at their resonance frequencies, (a) mode 2 at 1.4 GHz (b) mode 3 at 1.9 GHz (c) mode 4 at 2.1 GHz.	115
Figure 7.4: Characteristic mode analysis of the proposed antenna, (a) modal significance (b) characteristic angle (CA unit is in degree).....	116
Figure 7.5: Far-field radiation pattern of the different modes of proposed antenna at three different frequencies, (a) 1.5 GHz (b) 1.85 GHz.	116
Figure 7.6: Surface currents of different modes of Ant4 at three different frequencies, (a) 1.5 GHz (b) 1.85 GHz.....	117
Figure 7.7: Modal significance of the first five modes of the proposed antenna.....	119
Figure 7.8: Characteristic angle of the first five modes of the proposed antenna	119
Figure 7.9: Directivity of the proposed antenna in two different frequencies.	121

Figure 7.10: Surface currents of mode 1 and mode 3 at 1.15 GHz, and mode 2 and mode 5 at 1.65 GHz of Ant3.....	121
Figure 7.11: Rectangular slot antenna curved with a radius curvature of 300 mm, (a) side view (b) isometric view.	122
Figure 7.12: Reflection coefficient, axial ratio, and RHCP gain of the curved rectangular antenna in the second coordinate system ($\theta' = 0^\circ$ and $\phi = 0^\circ$), while the antenna is curved with a radius curvature of 300 mm.	123
Figure 7.13: Normalized radiation patterns of the curved rectangular slot antenna with a radius curvature of 300 mm at two different planes of $\phi = 0^\circ$ and $\phi = 90^\circ$ (a) 1.227 GHz (b) 1.575 GHz.	124
Figure 7.14: Spiral slot antenna curved with a radius curvature of 200 mm, (a) side view (b) isometric view.	125
Figure 7.15: Reflection coefficient, axial ratio, and RHCP gain of the curved spiral antenna in the second coordinate system ($\theta' = 0^\circ$ and $\phi = 0^\circ$), while the antenna is curved with a radius curvature of 200 mm.	126
Figure 7.16: Normalized radiation patterns of the curved spiral slot antenna with a radius curvature of 200 mm at two different planes of $\phi = 0^\circ$ and $\phi = 90^\circ$ (a) 1.227 GHz (b) 1.575 GHz.	127

List of Abbreviations

Abbreviation	First Use
AgGL : Silver Grid Layer	11
AR : Axial Ratio	14
AZO : Aluminum Zinc Oxide.....	10
BDS : BeiDou Navigation Satellite System.....	1
CMA : Characteristic Mode Analysis.....	49
CP : Circularly Polarized	5
CPW : Coplanar Waveguide.....	16
FBR : Front to Back Ratio	3
FTO : Fluorine Tin Oxide.....	10
GLONASS : Global'naya Navigatsionnaya Sputnikovaya Sistema	1
GNSS : Global Navigation Satellite System.....	1
GPS : Global Positioning System	1
HPBW : Half Power Beam Width	13
ITO : Indium Tin Oxide.....	10
LHCP : Left-Handed Circularly Polarized	3
LoS : Line of Sight.....	7
LP : Linearly Polarized	7
RFID : Radio Frequency Identification	6
RHCP : Right-Handed Circularly Polarized.....	3
SATNAV : Satellite Navigation	2
TCO : Transparent Conductive Oxide	10
WBAN : Wireless Body Area Networks	6
WiMAX : Worldwide Interoperability for Microwave Access	7
WLAN : Wireless Local Area Networks	6
WPAN : Wireless Personal Area Networks.....	6
WPT : Wireless Power Transmission	7

1. Chapter 1: Introduction

1.1 Overview

Communication systems are changing quickly due to rapidly changing technologies. Many researchers and scientists have dedicated considerable attention to different aspects of wireless systems. One of the most popular topics in antenna engineering is the antennas used in automotive applications. Nowadays, we can find many different antennas placed inside or on the vehicles like the roof, trunk, hood, windows, etc. [1]. These antennas might have different applications such as radio frequency reception which had been popular for a long time, car-to-car communication, and car-to-infrastructure communication which has become popular recently [1]. For location tracking of the vehicles, the Global Navigation Satellite System (GNSS) including Europe's Galileo, the USA's NAVSTAR Global Positioning System (GPS), Russia's Global'naya Navigatsionnaya Sputnikovaya Sistema (GLONASS) and China's BeiDou Navigation Satellite System (BDS), provide signals which could be received by any GNSS receivers, among them are antennas which work in GNSS frequency bands. These antennas though should have specific characteristics in order to be suitable for reception.

In this introductory chapter, an overview of GNSS/GPS antennas and three other types of antennas which are more important and useful in this work is first provided. Then, the research aims of this thesis are presented.

1.2 Literature Review

1.2.1 GNSS/GPS Antennas

Satellite navigation (SATNAV) systems use satellites to provide autonomous geospatial positioning and are accurate. These systems are limited to the line of sight (LoS) signal, but could be developed in a way to overcome this limitation [2]. GNSS includes all SATNAV systems, containing BDS, GLONASS, GPS, and some other systems for other countries and regions [2]. The main goal of the GNSS is to provide position with high accuracy (on the order of centimeters or sub-centimeters) [3], and also the velocity of a user. Each system has a pre-defined frequency range. Fig 1.1 shows the allocation of the frequencies for each different system.

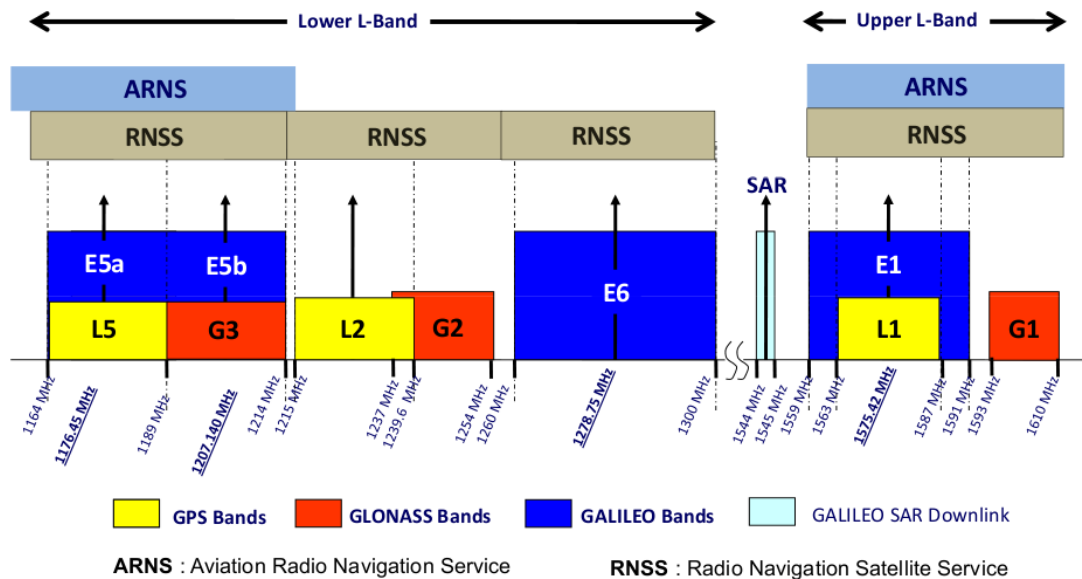


Figure 1.1: GNSS navigational frequency bands (taken from [4]).

The GPS which provides position and velocity to the users, lies in the GNSS frequency bands, and is comprised of three segments: a) satellite constellation, b)

Chapter 1: Introduction

ground control/monitoring network, and c) user receiving equipment [2]. The GPS signals are transmitted on two different frequencies called Link 1 (L1) which is the primary frequency, and Link 2 (L2), the secondary one, which are at 1575.42 MHz and 1227.6 MHz, respectively. Also, the new GPS band, namely L5 with a center frequency of 1176.45 MHz which is for safety-of-life transportation and other high-performance applications, is another GPS frequency band available in recent years.

GNSS antennas should have special characteristics in order to receive the data and work in a desired way. An ideal GNSS antenna should have a perfectly matched 50- Ω output impedance with a gain of more than unity with respect to an isotropic right-handed circularly polarized (RHCP) antenna with a gain of 0 dBic. Also, the gain should remain constant in the bandwidth, over the upper hemisphere in an elevation angle from zenith to a cut-off angle above the horizon, between 5 to 15 degrees. Moreover, the antenna should be able to prevent left-handed circularly polarized (LHCP) signal, coming from different directions due to the multipath effect [2]. Here, the term front to back ratio (FBR) is defined, meaning the ratio of power gain between the front and rear of a directional antenna, or in other words, the ratio of signal strength transmitted in a forward direction to that transmitted in a backward direction. For a GNSS or GPS antenna, the higher FBR, the better performance the antenna has, especially for antennas with a boresight beam direction, since the maximum RHCP and LHCP gains directions are completely opposite to each other. One of the most popular methods for increasing the FBR is to utilize a ground plane or reflector, usually with a quarter-wavelength distance below the antenna. Ideally, by applying the image theory and by having an infinite ground plane, the pattern of the antenna

Chapter 1: Introduction

would become unidirectional. But, in most of the cases, the situation would not be the ideal one. Furthermore, size and cost of the antennas matter. It is preferred to have antennas with low cost and compact size.

There have been many attempts to design GNSS (or GPS) antennas in recent years. Different types of antennas are used for implementation. The feeding structure also can be either single feed or multiple feed, depending on the structure and geometry of the antennas. In the following, several examples of microstrip antennas working in GNSS or GPS bands are presented. In [5], a proximity-fed stacked patch antenna is presented, working in three GPS frequencies, as well as E5a and E5b bands for the Galileo system with an RHCP polarization. To reduce the size of the antenna, a high permittivity dielectric is used. To achieve an RHCP polarization, two feeding ports have been used. The overall size of the antenna has been minimized to $\lambda/8$ at the L5 band. In reference [6], a GPS dual-band microstrip patch antenna with reduced susceptibility to low-angle multipath is introduced for high-precision applications. In another attempt [7], a dual-band dual-layer dual-feed stacked annular-ring patch antenna is introduced. Here, the antenna is excited by two orthogonal H-shaped slots which are fed by a 3-dB hybrid. The overall size of the antenna is $140 \times 140 \text{ mm}^2$. For reaching a dual-band characteristic, two concentric annular rings are designed with different radii on the top of the substrate. However, the radiation pattern of the antenna is bidirectional. Also, having a dual-feed antenna enhances the complexity of the design. It is preferable to diminish the complexity of the structure as much as possible. To render a unidirectional pattern, a ground plane or reflector is needed below the antenna. As an example, in [8], a dual-band circularly polarized single feed cavity-

Chapter 1: Introduction

backed annular slot antenna for GPS receivers is introduced, working in L1 and L2 bands of GPS. Here, by attaching a cavity to the backside of the antenna, the front to back ratio has increased to almost 10 dB. However, the size of the antenna is $100 \times 100 \text{ mm}^2$ with a height of 20 mm which is around $0.4 \lambda_0 \times 0.4 \lambda_0 \times 0.08 \lambda_0$ at the lowest frequency of 1.227 GHz (λ_0 is the wavelength at free space).

As another example of microstrip antennas, a dual-band circularly polarized antenna for GPS bands containing a high impedance surface ground plane is proposed [9]. The effect of the surface is to realize a unidirectional radiation pattern by placing it under the radiator. Although the size of the antenna is large ($100 \times 100 \times 18 \text{ mm}^3$), a high FBR of 21 dB is obtained.

As an example of compact and low-profile GNSS antenna, YUAN et al. has proposed a compact meandered ring patch antenna loaded with four parasitic-grounded patches and a slotted ground [10]. The patch size is $0.169 \lambda_g \times 0.169 \lambda_g$ and the overall size of the proposed antenna is $0.285 \lambda_g \times 0.285 \lambda_g \times 0.035 \lambda_g$, where λ_g denotes the guide wavelength at the center frequency. To reduce the antenna size, several techniques are employed such as small square patch parasitic inserts with grounded vias, the ground plane with a slot cut and corner cuts, and meandered ring patch.

The abovementioned examples were all planar structures with either single or multi layers, while some other nonplanar structures have been reported recently. In [11], a nonplanar CP dual-band antenna working in GPS, GLONASS, and Galileo E5a/b and E1 has been proposed with the capability of integration within the body of a cylinder. This conformal antenna also has a wide angular coverage which is desirable for GNSS

applications. The antenna is fed with two additional feeds for suppressing the higher order modes.

All the abovementioned examples of GNSS/GPS antennas have a common characteristic which is the circular polarization of the antenna.

In the next section, CP antennas which have a key role in GNSS/GPS applications will be discussed in more details.

1.2.2 Circularly Polarized Antennas

The polarization of an antenna is defined as “the polarization of the wave transmitted (radiated) by the antenna in a given direction. If the direction is not mentioned, then the polarization in the maximum gain direction is taken into consideration [12]. Three different kinds of polarizations can be defined: a) linear, b) circular, and c) elliptical. In circular polarization, the magnitude of the two electric (or magnetic) components are the same, and the time-phase difference between them is odd multiples of $\pi/2$ [12]. If the rotation of the electric field vector is clockwise (as observed along the direction of propagation), then the wave is an RHCP wave. If the rotation is counter-clockwise, then the wave is an LHCP wave [12].

A circularly polarized (CP) antenna is a type of antenna which has a circular polarization. In recent years, CP antennas have been widely used in different wireless systems, among them are GNSS, radio frequency identification (RFID), wireless local area networks (WLAN), wireless body area networks (WBAN), wireless personal area networks (WPAN), Worldwide Interoperability for Microwave Access

Chapter 1: Introduction

(WiMAX), mobile and satellite communications, wireless power transmission (WPT), and many other wireless systems [13].

Circularly polarized antennas have several advantages over the linearly polarized (LP) ones. One of the advantages of using a CP antenna is to reduce the complexity of the systems which are used for adjusting the antenna alignments in point-to-point communications. As a result of using CP antennas, the orientation of the transmitter and receiver antennas do not matter anymore. Also, reducing the “Faraday rotation” effect which happens due to the ionosphere and maintaining the sense of polarization is another advantage of CP antennas over the LP antennas [14], [15]. Furthermore, CP antennas are capable of reducing the multipath signal effects. By reflecting the main signal from different surfaces and objects, the sense of polarization of the signal changes, i.e., if the LoS signal is an RHCP signal, then the reflected wave is an LHCP signal. Hence, taking this change in sense of polarization into consideration, it is desirable to remove the reflected wave by stopping the reception of the multipath signal, as these signals make errors in most of the applications.

Several types of CP antennas have been introduced, among them are microstrip patch antennas [16], wire antennas [17], helix antennas [18], spiral antennas [19], slot antennas [20], horn antennas [21], and so on.

Most of the GNSS antennas have a boresight radiation pattern, having a maximum gain at zenith (zero elevation angle). Nonetheless, there are many other structures in which the maximum radiation pattern occurs at other elevation angles, rather than zenith. These antennas are called *tilted beam* antennas, which will be discussed in the next section.

1.2.3 Tilted Beam Antennas

So far, the antennas mentioned above were all assumed to have boresight radiation pattern, meaning that the maximum gain of the antenna occurs at zenith ($\theta = 0^\circ$). However, there are some other types of antennas in which the radiation pattern is tilted from the zenith, known as *tilted beam* antennas, which have many applications in emerging wireless communication systems such as mobile communication systems, satellite communications systems, WLAN systems, and so forth [22]. Tilting the beam of the antenna will reduce the use of mechanical instruments which traditionally were used for changing the direction of the beam of the antennas. Also, in some other cases, changing the direction of the antenna would be a solution for transmitting or receiving signals in a direction rather than zenith.

There are several techniques which have been used recently for beam tilting. The first technique is to use an antenna capable for producing a tilted beam. There are several antennas which can be used for beam steering or beam tilting. Helix and spiral antennas are two kinds of the most common antennas in this field. As an example of spiral antennas, a single-arm spiral antenna radiating a tilted beam is proposed in [23]. The spiral peripheral length is within $2\lambda_g < C < 3\lambda_g$, while it radiates an axial beam when the peripheral length is within $\lambda_g < C < 2\lambda_g$, where λ_g is the guided wavelength of the current. In other attempts, parasitic plates are used to tilt the beam [24]. A single-feed antenna with a wide beam and two parasitic loop-based plates are used in this work. The electromagnetic waves which are radiated from the antenna will have a phase shift when they are passing through the plates. For the two-plate system a tilted beam angle of 54 degrees in elevation plane is observed.

Chapter 1: Introduction

For microstrip antennas, one of the most important factors that should be considered here is to induce surface currents in a way that it causes asymmetry in the current distribution of the antenna. In this way, the asymmetric current distribution will cause a tilted radiation pattern. In [25], by introducing a new geometrical configuration of a bow-tie antenna, a tilted radiation pattern is obtained. The tilted angle can be controlled by changing certain parameters, like the flare angle of the ground. The tilted angle can alter from 0° to 60° in elevation across the bandwidth. There are also many other ways which can help making the beam tilted.

As the desired antenna in this work is going to be placed on the windshield of a car, it is preferable to have a semi-transparent antenna (or ideally, full-transparent). In the next section, transparent antennas are reviewed in detail.

1.2.4 Transparent Antennas

In the past years, transparent antennas have been given considerable attention because of their numerous applications in the wireless communication systems [26]. These types of antennas were designed and proposed many years ago. In 1989, a wideband transparent antenna was proposed for receiving frequency modulation (FM) signals in order to be integrated on the windshield of vehicles [27]. In 1991, another transparent antenna was proposed for mobile wireless communication applications on a transparent substrate [28]. Moving on to the past recent years, many different transparent antennas with different topologies have been designed and proposed [29]. First of all, to design a transparent microstrip antenna, the substrate must be transparent itself. This implies the usage of transparent materials as the substrate of

Chapter 1: Introduction

the antennas. Two common materials which have been used as the substrate are glass and plastics [29]. Acrylic is also another type of transparent material which can be used as the substrate [30]. Many transparent conductive materials have been studied and used in the past years. Optically transparent conductors are typically distinguished in terms of their optical performance (usually characterized by their transmittance), and their electrical performance (usually sheet or surface resistance). The ideal transparent conductive material has a transmittance of 100 % with an infinite conductivity, i.e., no sheet resistance. However, as no such ideal material exists, tradeoffs should be considered when choosing a conductive material. These materials can be divided into two main categories: The first one is transparent conductive oxides (TCO), and the second one is metal mesh. Different TCOs have been introduced in the past years. Indium Tin Oxide (ITO) is one of the most commonly used examples of introduced TCOs in the past years. The sheet resistance of ITOs vary between 1.3 to 19.8 Ω/sq [31]. Aluminum Zinc Oxide (AZO) is another type of TCO with a sheet resistance of between 3.8 to 7.1 Ω/sq and transparency between 76 to 96.5 % [32] [33] [34]. Other transparent conductive materials also have been used and investigated like Fluorine Tin Oxide (FTO) [35], AgHT coated film [36], ITO/Cu/ITO multilayer [37], and so on. The sheet resistance of TCOs is much higher than the surface resistance of good conductors like silver and copper, causing a high transmission loss. Another problem of using TCOs as the conductive layer is the scarcity and expensiveness of these materials [33].

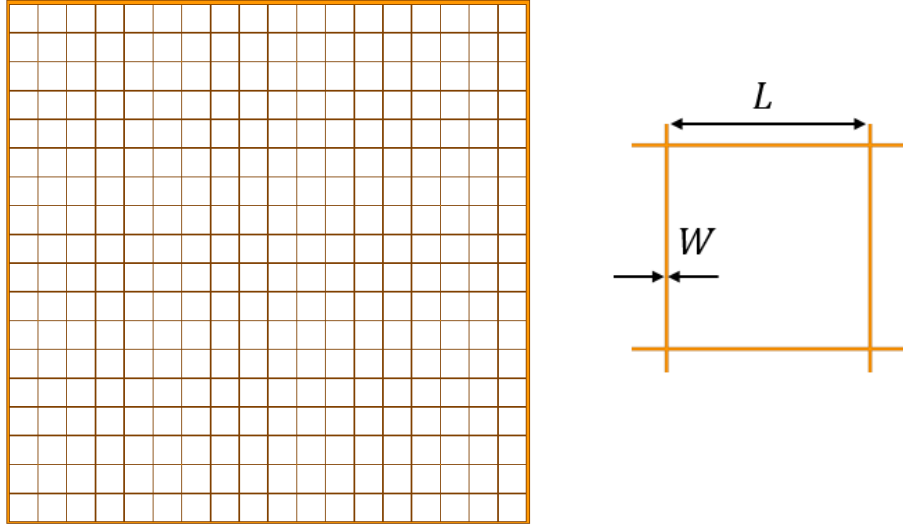


Figure 1.2: A simple metal mesh pattern with enlarged section of a single mesh element

The second category of transparent conductors are metal mesh grids, which physically consist of metals forming a periodic mesh pattern. Fig. 1.2 shows a simple mesh pattern along with a single mesh element, showing the length and width of each one. Using metal mesh for electromagnetic interference shielding was proposed in [38], [39]. In high frequency RF applications, metal mesh is more preferable (depending on the conductivity of the metal) in comparison to TCOs. Published works show that the mesh surface resistance differs between 0.018 to 0.36 Ω/sq [29]. Also, since the geometry of the conductor does not change in regard with the optical wavelength, the transmittance is more stable over a high frequency range, compared to TCO materials. Furthermore, the sheet resistance of mesh grids are 22 times less than that of AZO and ITO with the same resistance [29]. Taking all above-mentioned discussion into consideration, metal mesh conductors are more preferred to be used than the TCO materials for RF high frequency applications. Many transparent antennas with metal mesh grids have been proposed in recent years. In [40], a silver grid layer (AgGL) deposited on a Corning glass substrate later is proposed for design and fabrication of

Chapter 1: Introduction

an H-shaped multilayer slot antenna. In another attempt [30], a transparent patch antenna using metal mesh is proposed. The antenna consists of a metal mesh grid layer used to make the antenna transparent. The transparency then is calculated by the ratio of open area and the whole area of the antenna. As another example, an optically transparent antenna used for mobile devices is proposed in [41]. The metal mesh grid consists of diamond shaped elements rather than common square and rectangular shaped elements.

To increase the transparency of the metal mesh grid, the width of the traces can be reduced (consequently increase the length of each element). However, this cannot be an arbitrary number. For a simple microstrip structure, the preferred spacing should be much less than a wavelength [29]. Moreover, by decreasing the width of the traces, the fabrication of the antenna would become much harder.

Therefore, as stated earlier, a metal mesh grid pattern is more preferred for using in high frequency RF applications.

In the next section, the research aims and how it has been completed are discussed.

1.3 Research Aims

The objective of this work is to design, fabricate, and test antennas suitable for vehicular platforms. The main goal is to design a GNSS/GPS antenna suitable for placing on the windshield of vehicles. Based on the literature review, the antenna is desired to have the following characteristics simultaneously:

1- Circularly polarized in the desired GNSS bandwidth

- a. The antenna should have an RHCP radiation pattern in order to receive the GNSS/GPS signals from the satellites.
- b. As discussed earlier in “*GNSS/GPS Antennas*” section, the LHCP gain should be minimized since receiving the LHCP signals can have unwanted effects and interference on the system.

2- Having a tilted beam in the desired GNSS bandwidth

- a. The beam of the antenna is desired to have a tilted angle of around 30 degrees since most of the cars’ windshields are inclined for about 30 degrees in elevation.
- b. The half power beam width (HPBW) of the antenna is also desired to be as high as possible, to enhance the performance of the signal reception by connecting to more satellites.

3- Semi-Transparent

- a. As the antenna is going to be placed on the windshield, it is desired to be transparent as much as possible, not to block the vision of the driver
- b. Based on the literature review, the metal mesh grid is chosen for the transparent conductive layer, instead of using TCOs

Chapter 1: Introduction

In the following chapters, several antennas designed for GNSS/GPS applications are proposed. In order to satisfy the above-mentioned criteria simultaneously, the antenna designed in each chapter is an improvement upon the previous one.

In chapter 2, a wideband CP antenna is proposed. The antenna operates in a wideband frequency range, covering the GNSS/GPS bands as well. Also, the HPBW of the antenna is acceptable (more than 60 degrees) in the desired GPS bands. The RHCP and LHCP gains of the antenna are almost equal in GNSS frequency bands, or in other words, with 0 dB of front to back ratio. Moreover, the antenna does not have a tilted beam and is not transparent. Although this antenna does not have all the desired characteristics at the same time, it gives some clues and information about how to design antennas with wide impedance and axial ratio (AR) bandwidths. Therefore, for the next step, an antenna having a wide impedance and axial ratio bandwidth with a high FBR covering GNSS/GPS bands is desired to be designed.

In chapter 3, a dual-band CP antenna is proposed working in GNSS/GPS frequency bands. This antenna works in GNSS/GPS with circular polarization, showing a very good and acceptable FBR (more than 20 dB), with a proper HPBW (more than 60 degrees), which is an improvement from the previous step. By designing this antenna, we get closer to the end goal. The only remaining features for the desired antenna are tilted beam and transparency.

Chapter 1: Introduction

In chapters 4 and 5, two different antennas suitable for the desired aims have been proposed. Both antennas are wideband, circularly polarized and have tilted beams of about 30 degrees in elevation. Moreover, both antennas are transparent, in which conductive silver mesh grid is used as the conductive layer. A transparent reflector also has been proposed in order to be placed under the antennas with certain distances in order to decrease the LHCP gain of the antenna (or in other words, increase the FBR). By designing these two antennas, the end goal has been achieved.

Finally, chapter 6 talks briefly about the future possible works.

2. Chapter 2: A Low-profile Wideband Circularly Polarized CPW Slot Antenna

2.1 Introduction

A small and simple wideband CP planar coplanar waveguide (CPW) slot antenna is proposed in this chapter. To create CP radiation in the proposed antenna, three asymmetrical rectangle slots, which are fed at the open end of a CPW line, are used. The 10-dB impedance bandwidth of the antenna is 129.5 % while the 3-dB axial ratio bandwidth remains 112 % within the operating impedance bandwidth. Also, the 3-dB gain bandwidth is about 108 % (0.9-3.05 GHz). The superiority of the designed antenna is achieved by using a simple and compact configuration which leads to the widest overlapping impedance and AR bandwidth while the obtained antenna size is only $0.07\lambda_0^2$ at the lowest frequency band of interest. In addition, the antenna design procedure is explained using easy-to-follow steps, which is shown in the antenna design flowchart. It should be mentioned that based on the simple configuration and also straight forward design steps, the antenna parametric study and optimization time reduced significantly. To the best of authors' knowledge, there are not any other small wideband CP antennas with comparable performances (112 % impedance and AR BWs) in the literature. The rest of this chapter is organized as follows. The antenna configuration and design procedure are explained in Section 2.2. Then, the fabricated antenna and the experimental results are discussed in Section 2.3. Finally, the chapter is summarized in Section 2.4.

2.2 Antenna Design and Configuration

The geometry of the proposed antenna is shown in Fig. 2.1. It has been designed on a Rogers RO3006 substrate with $\epsilon_r = 6.15$, $\tan\delta = 0.0025$, thickness of 0.64 mm and overall size of $89.9 \times 88 \text{ mm}^2$ ($0.27\lambda_0 \times 0.26\lambda_0 \times 0.002\lambda_0$). The CPW line is fed by a 50Ω coaxial feedline. The antenna consists of three slots and a feedline. The development stages of the antenna and the CP mechanism are discussed in the next sections.

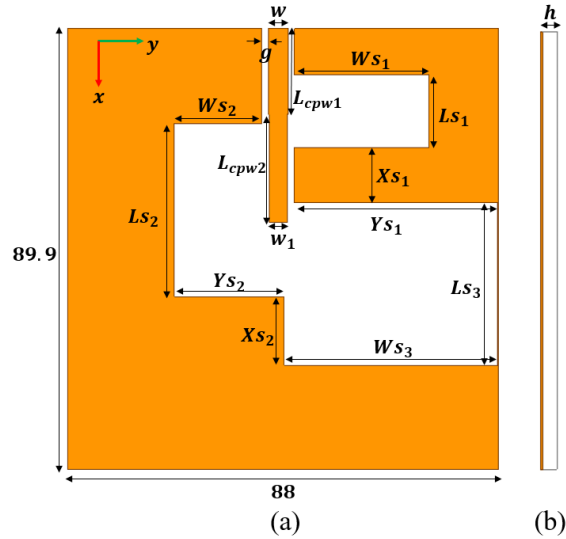


Figure 2.1: Proposed antenna structure, (a) top view, (b) side view. $h = 0.64$, $w = 4$, $w_1 = 3.65$, $g = 1.35$, $L_{cpw1} = 17.53$, $L_{cpw2} = 22$, $W_{s1} = 27.4$, $W_{s2} = 17.8$, $W_{s3} = 43.5$, $L_{s1} = 14.8$, $L_{s2} = 35.3$, $L_{s3} = 33.2$, $X_{s1} = 11.2$, $X_{s2} = 14$, $Y_{s1} = 41.43$, and $Y_{s2} = 22.37$ (units are in mm).

2.2.1 Antenna Development Stages

The antenna development consists of four stages illustrated in Fig. 2.2.

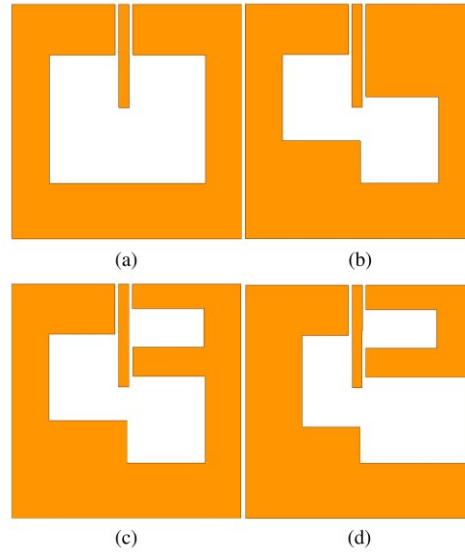


Figure 2.2: Evolution stages of the proposed antenna, (a) Antenna 1, (b) Antenna 2, (c) Antenna 3, (d) Proposed antenna.

As can be seen in Fig. 2.2, at the first stage, a slot with the dimension of $60 \times 50 \text{ mm}^2$ is etched and a feedline with a length of $L_{cpw1} + L_{cpw2}$ is printed on the substrate (Antenna 1). The feedline excites the etched slot, which causes two resonances near 2.5 and 4 GHz as can be seen in Fig. 2.3 (a). The resonances are coming from the slot dimensions and the open ended CPW line. However, the antenna is LP in the desired frequency range. To make the antenna CP, two rectangular strips are added to diagonal edges of the slots, which cause asymmetry (Antenna 2). This improves the axial ratio but not enough to obtain an acceptable circular polarization ($< 3 \text{ dB}$), while worsens the reflection coefficient. One solution would be introducing a perturbation (slot) in the conductive layer of the antenna in order to get the phase difference between E_x and E_y close to 90 degrees. On the other hand, antenna 2 is not matched to a 50Ω feedline as can be seen from Fig. 2.3 (a). From the theory of matching networks, when there is a circuit which is not matched to a transmission line with a specific

characteristic impedance, the circuit can be matched by using or introducing a matching network, either by using lumped capacitive and inductive elements or by using the elements which have the capacitive and inductive effects. Usually, this matching network is added at the beginning of the circuit, between the transmission line and the circuit. Hence, by adding a slot at the beginning of the antenna, two main goals would be reached simultaneously. First, it causes a phase difference between the E_x and E_y components. Secondly, it improves the impedance matching by adding the slot as a matching circuit. By taking all into consideration, adding a slot at the beginning of the antenna will cause both the impedance matching and the axial ratio to improve. Thus, to improve the impedance and AR bandwidths, a rectangular slot is etched with an offset of 9.5 mm (Antenna 3). As can be seen in Fig. 2.3, both S_{11} and axial ratio have been improved significantly. The generation of circular polarization will be discussed later.

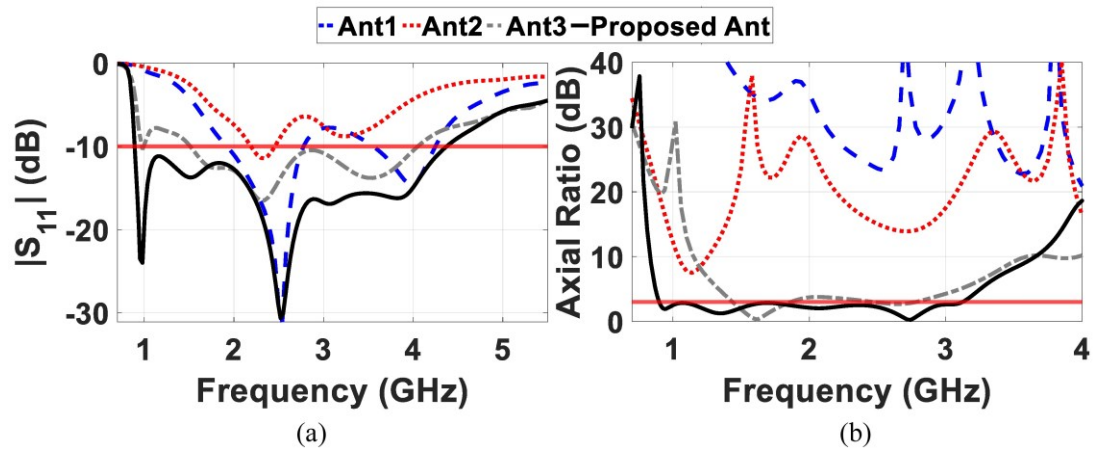


Figure 2.3: Simulation results for four evolution stages of the proposed antenna, (a) Reflection coefficient, (b) AR.

To have a better understanding of how the slot is operating as a matching circuit, antenna 2 has been split into two sections, showed in Fig. 2.4 (a). By having the S-

Chapter 2: A Low-profile Wideband Circularly Polarized CPW Slot Antenna

parameters of upper and lower sections of the antenna, the matching circuit (slot) can be shown by a combination of R, L, and C connected to the S-parameters' responses of the two sections. The matching circuit (slot) is assumed to improve the antenna's matching to a 50Ω input feed. The slot can be shown by a combination of parallel RLC. However, as the antenna is working in a wide bandwidth, one set of RLC components might not be enough to model the slot. Also, by adding a slot, the electric coupling between the slot and S-parameters of the lower section of the split antenna arises.

This can be modeled by mutual capacitance and inductance effects. Additionally, the radiation of the antenna can be modeled with resistors. The final equivalent circuit of antenna 3 which includes the lumped element is shown in Fig. 2.4 (b).

To prove the concept, the reflection coefficient of antenna 3 using the equivalent circuit and full wave simulation has been shown in Fig. 2.5. In the final stage, an optimization is done to enhance the impedance and axial ratio bandwidths. The reflection coefficient and axial ratio of antennas 1, 2, 3, and the proposed antenna are shown in Fig. 2.3.

For generating circular polarization, the orthogonal field components of E_x and E_y should have equal magnitudes and should be 90° out of phase in the frequency band of interest. To have a better understanding about circular polarization generation, the absolute magnitude ratio of two electric field components of E_x and E_y and their phase difference for antennas 1-3 and the proposed antenna have been depicted in Fig. 2.6.

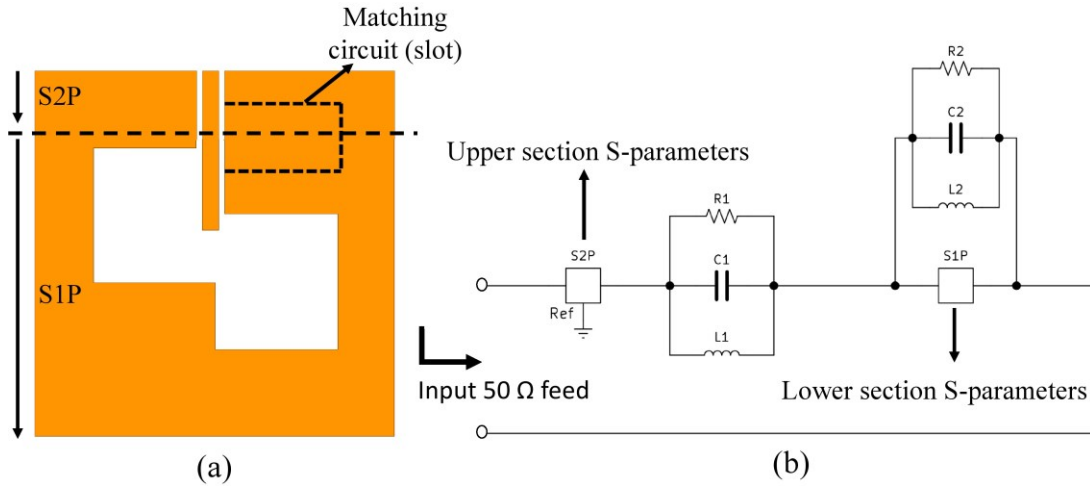


Figure 2.4: Analysis of antenna 3, (a) the way in which antenna 3 has been cut for obtaining corresponding reflection coefficients, (b) equivalent circuit of antenna 3 showing the RLC model of the slot.

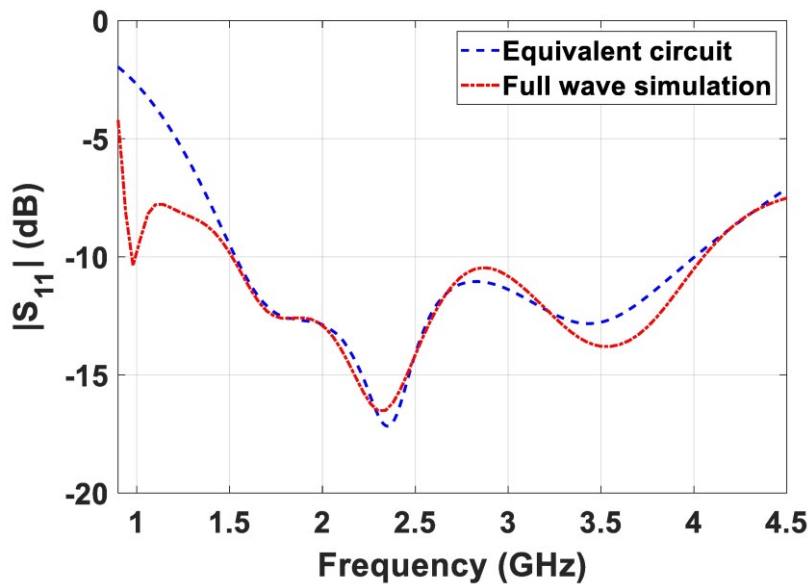


Figure 2.5: Reflection coefficient of antenna 3 using equivalent circuit model and full wave simulation.

As can be seen in Fig. 2.6 (a), the magnitude ratio of E_x and E_y for antenna 1 is large, which will not cause a circular polarization. For antenna 2, the two diagonal slots cause a symmetry, which gives much lower magnitude ratio of E_x and E_y . However,

as shown in Fig. 2.6 (b), the phase difference (PD) between the two field components is not enough for making the antenna circularly polarized. After adding the rectangular slot (antenna 3), by maintaining the magnitude ratio of E_x and E_y , the phase difference gets closer to 90° . Finally, by optimizing the antenna 3, the proposed antenna is introduced in which both the magnitude ratio and the phase difference have been improved to provide CP.

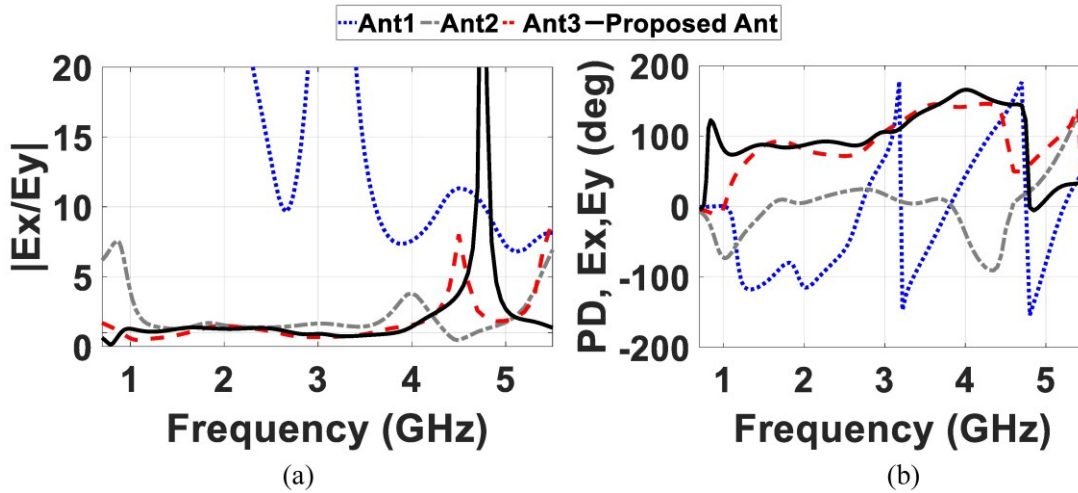


Figure 2.6: Magnitude ratio and phase difference of orthogonal field components E_x and E_y , (a) magnitude ratio, (b) phase difference (the unit is in degree).

2.2.2 CP Mechanism

The surface current distribution of the proposed antenna is illustrated at four different time instants at 0.9 and 1.6 GHz in Fig. 2.7 and Fig. 2.8, respectively. The current distribution at different regions has been shown by black arrows, while the sum of the current vectors is shown with the red arrows. As can be seen from Fig. 2.7, the dominated surface current is pointing upward at 0° . At 90° , the surface current orientation is changing for 90° counter-clockwise [see Fig. 2.7(b)]. The concentrated

dominant field is oriented along the x-direction at 180° . Finally, at 270° , the surface current distribution is pointing toward the y-direction. Also, in Fig. 2.8, the current distribution has been shown by black arrows in different regions. At 0° , most of the currents are pointing toward downward and (-y)-direction, while most of the currents rotate toward (+y)-direction at 90° with some currents still pointing to down. Besides, at the time instant of 180° , the current distribution vector sum points to up and right side, while the current vector sum rotate for 90 degrees in the counter-clockwise direction, pointing to the up and left side at the time instant of 270° .

It can be inferred from Fig. 2.7 and Fig. 2.8 that as the surface current orientation is rotating in the counter-clockwise direction, the antenna has a right-handed circular polarization (RHCP) radiation pattern.

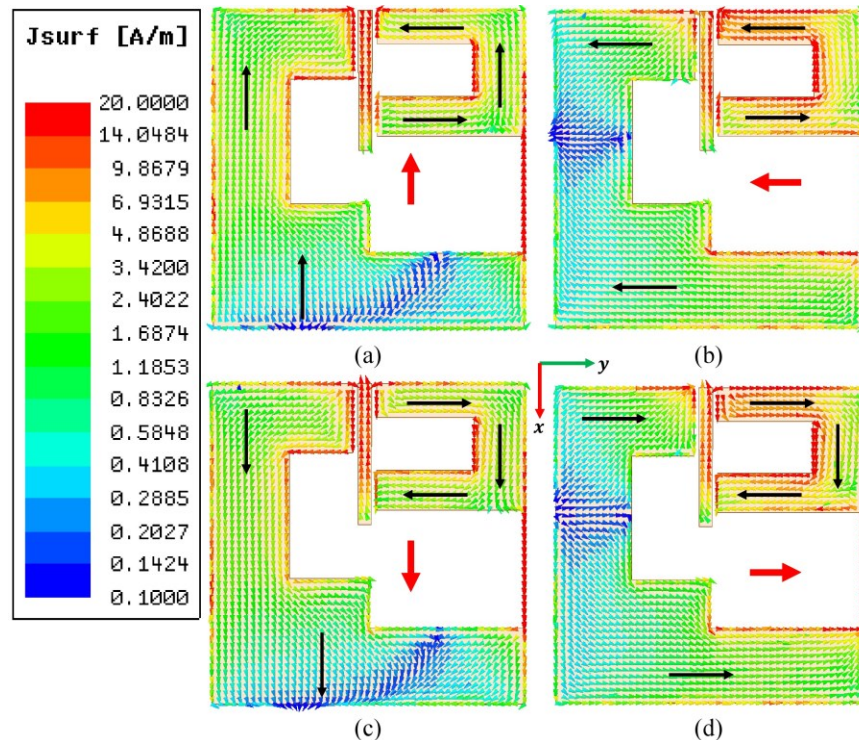


Figure 2.7: The surface current distribution of the proposed antenna at 900 MHz, (a) 0° , (b) 90° , (c) 180° , (d) 270° .

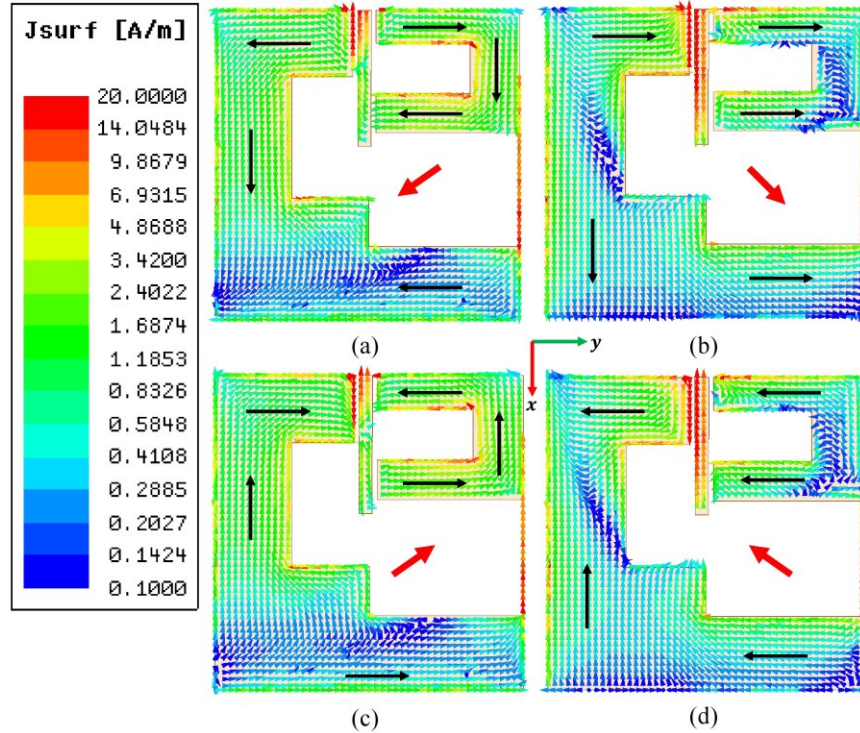


Figure 2.8: The surface current distribution of the proposed antenna at 1.6 GHz, (a) 0°, (b) 90°, (c) 180°, (d) 270°.

2.2.3 Redesigning the antenna

The antenna can be redesigned for other operating frequencies as the geometry of the antenna is simple. Generally, by scaling the size of the antenna up/down, the operating frequency of the antenna decreases/increases. Hence, the size of the antenna can be scaled in order to shift the frequency bandwidth to another desired one. Also, the AR bandwidth can be adjusted in the same way. To prove this concept, three antennas with the scaling values of 0.6, 1.2, and 2 have been simulated. Scaling factor of $S=2$ means that the antenna size including all parameters has been doubled, where the new scaled antenna dimensions would then become $179.8 \times 176 \text{ mm}^2$. Here, scaling factor

of $S=1$ shows the proposed antenna. Reflection coefficient and the AR bandwidth of the scaled antennas are demonstrated in Fig. 2.9.

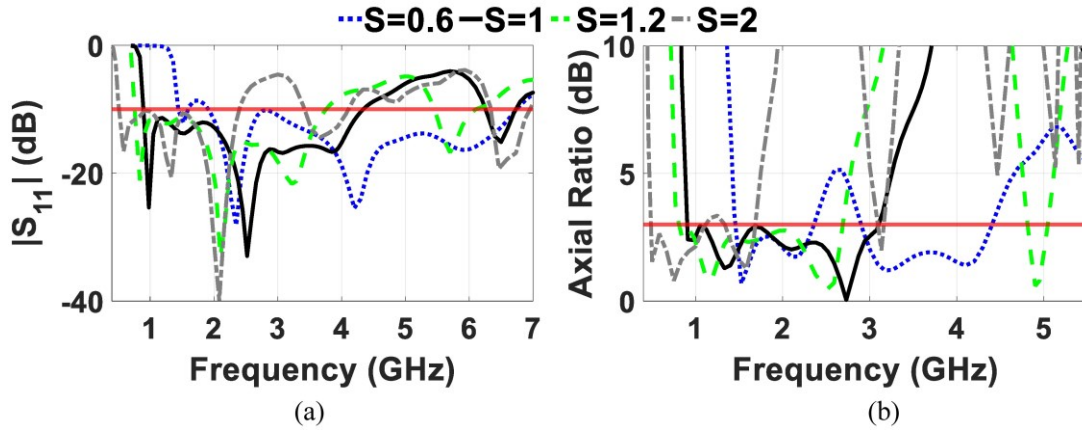


Figure 2.9: Simulated redesigned antennas for different scaled sizes, (a) S_{11} , (b) Axial Ratio.

2.2.4 Parametric Study

There are several parameters that have impact on reflection coefficient and AR of the antenna. The effects of three main parameters of the antenna on the reflection coefficient and axial ratio is presented in this section. As can be seen in Fig. 2.10, three main parameters W_{s1} , W_{s3} , and L_{cpw2} have been studied.

W_{s1} dominantly influence the AR bandwidth whereas it does not have significant effects on the impedance bandwidth. Also, it alters the higher end of the AR bandwidth. The reason for the change in the higher end of the AR bandwidth is that by increasing the size of the first slot (W_{s1}), the magnitude ratio of E_x and E_y will not change a lot, while the phase difference between the two components of E_x and E_y changes at $\theta = 0^\circ$ and $\phi = 0^\circ$. Thus, by introducing a longer slot, the phase difference between E_x and E_y changes in higher frequencies, leading to a circular

polarization in the frequencies with a 90 degrees phase difference. Also, by changing the size of first slot, the capacitance effect will change, and this will result in a change in the first resonance frequency. As the first slot also acts as a matching network, the resonance frequencies and impedance bandwidth will change by changing the size of the slot.

W_{s3} has a significant influence on the value of AR in the desired frequency bandwidth, especially the lower end. Increasing the value of W_{s3} leads to a better axial ratio. This is because of the fact that changes in the value of W_{s3} will mainly affect the phase difference of E_x and E_y at lower frequencies rather than higher frequencies. Also, by changing the size of third slot, the capacitance and inductance effect of the slot will change, and this will result in a change in the third resonance frequency. Increasing the size of W_{s3} will improve the AR bandwidth in lower frequencies, as the phase difference between E_x and E_y gets closer to 90 degrees. However, it does not change the impedance bandwidth and resonance frequencies much.

The length of the feedline, L_{cpw2} , has the most impact on the impedance bandwidth. Also, as can be seen in Fig. 2.10, it changes the resonance frequencies. By assuming that the feedline has capacitive and inductive effects, changing the size of the feedline will lead to a change in resonance frequencies and impedance bandwidth as the feedline has impacts on all three slots simultaneously, and this will cause change in all the bandwidth. By increasing the length of the feedline, the resonance frequencies shift toward the lower frequencies. The axial ratio bandwidth increases slightly by increasing the L_{cpw2} parameter (see Fig. 2.10).

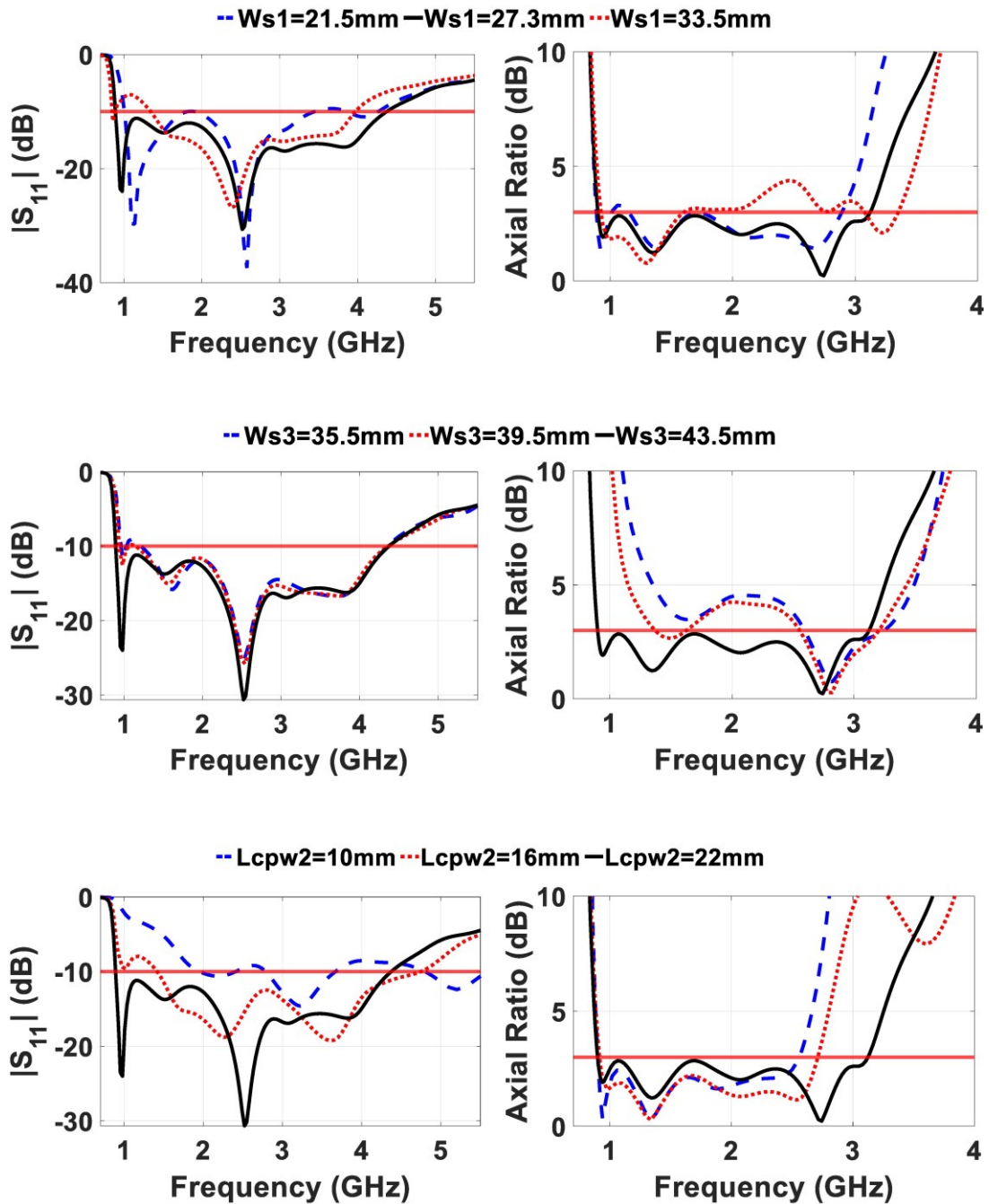


Figure 2.10: Parametric analysis of the proposed antenna in terms of reflection coefficient and axial ratio.

To summarize the proposed antenna design procedure, the antenna design flowchart has been shown in Fig. 2.11. As can be seen, the design procedure shows a step-by-step process in which the AR and impedance bandwidths of the antenna are set to the

desired ones by changing and tuning the parameters. As the design procedure shows, after setting the slots widths and lengths, the first step is to set the minimum CP frequency to the desired one. After achieving the desired minimum CP frequency, the AR desired bandwidth will be achieved by tuning the W_{s3} and L_{s3} parameters. Finally, to get the desired impedance bandwidth, the feedline length should be optimized.

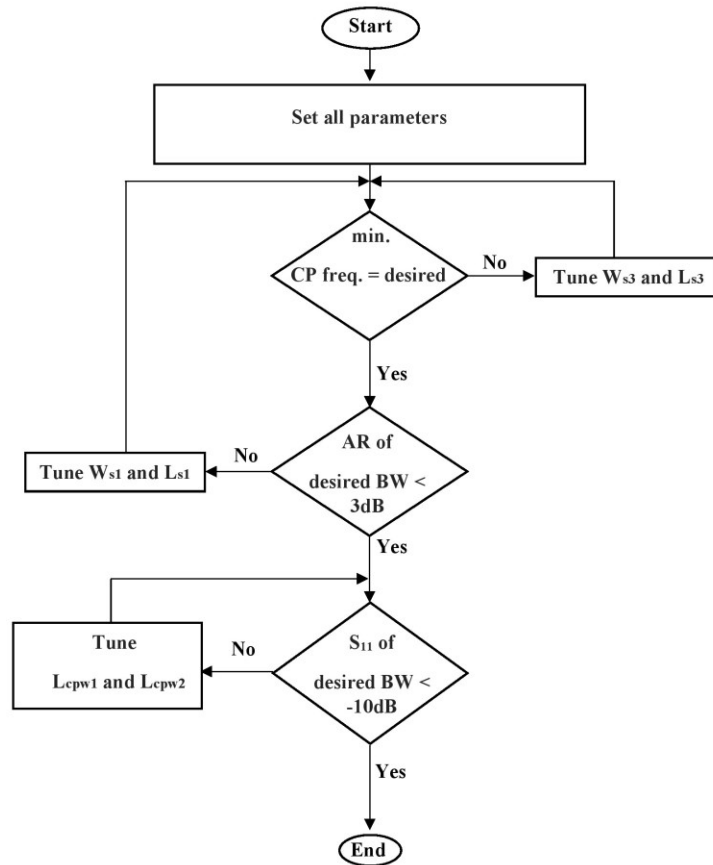


Figure 2.11: The flowchart design procedure of the proposed antenna.

2.3 Simulation and Measurement Results

The fabricated antenna and the anechoic chamber are illustrated in Fig. 2.12. The reflection coefficient and axial ratio simulated and measured results, which are in a close agreement, have been show in Fig. 2.13. The simulated impedance bandwidth is 130 % (0.9-4.3 GHz), and the simulated AR bandwidth is 110 % (0.9-3.1 GHz), while the measured S_{11} and AR bandwidth are 129.5 % (0.9-4.2 GHz) and 112 % (0.9-3.2 GHz), respectively. However, there is a little shift between measurement and

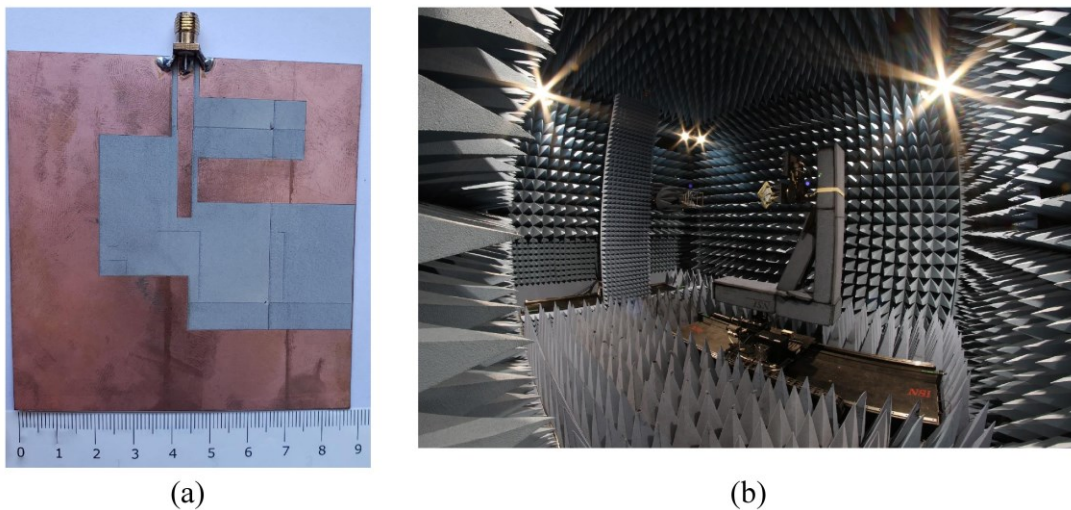


Figure 2.12: Fabrication and measurement of the proposed antenna, (a) photograph of the fabricated antenna prototype, (b) measurement of the antenna in an anechoic chamber.

simulation results which is due to fabrication processes and also substrate dielectric variation. The overlapping bandwidth of the 10-dB impedance bandwidth and the 3-dB axial ratio bandwidth is about 112 % (0.9-3.2 GHz), which has the most overlapping bandwidths among the designs reported in the literature. This overlapping bandwidth makes the path easy for the proposed antenna to be used in different applications like RFID, GNSS, WLAN, WiMAX, etc.

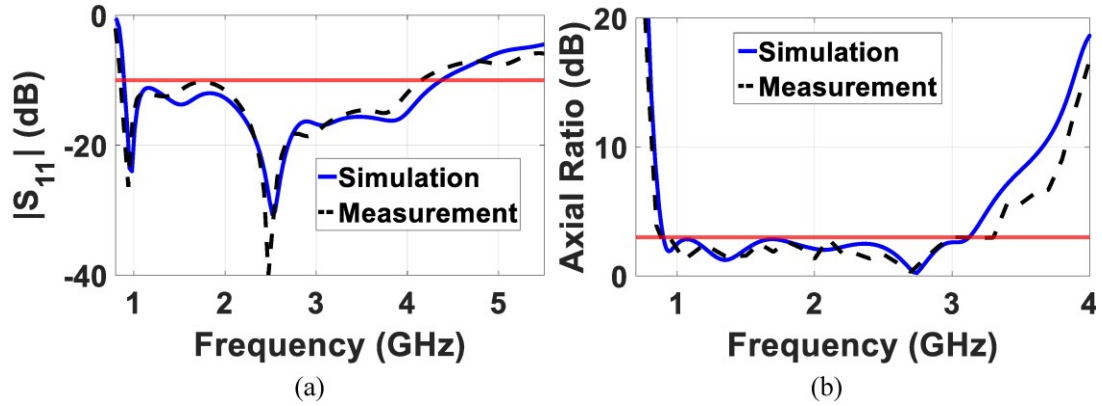


Figure 2.13: Simulated and measured parameters of the proposed antenna, (a) S_{11} , (b) Axial Ratio at $\theta = 0^\circ$ and $\phi = 0^\circ$.

The simulated and measured RHCP gain of the proposed antenna is demonstrated in Fig. 2.14. The obtained antenna 3-dB gain bandwidth is about 108 % (0.9-3.05 GHz). Wide 3-dB gain bandwidth would be suitable for applications with stable gain requirement. The peak gain (both simulation and measurement) of the proposed antenna is 5 dBic. It is worth mentioning that the peak gain and the front to back ratio of the antenna can be improved by using a reflector or a cavity. The simulation and measurement results for the total efficiency of the antenna is more than 90 % throughout the overlapping bandwidth.

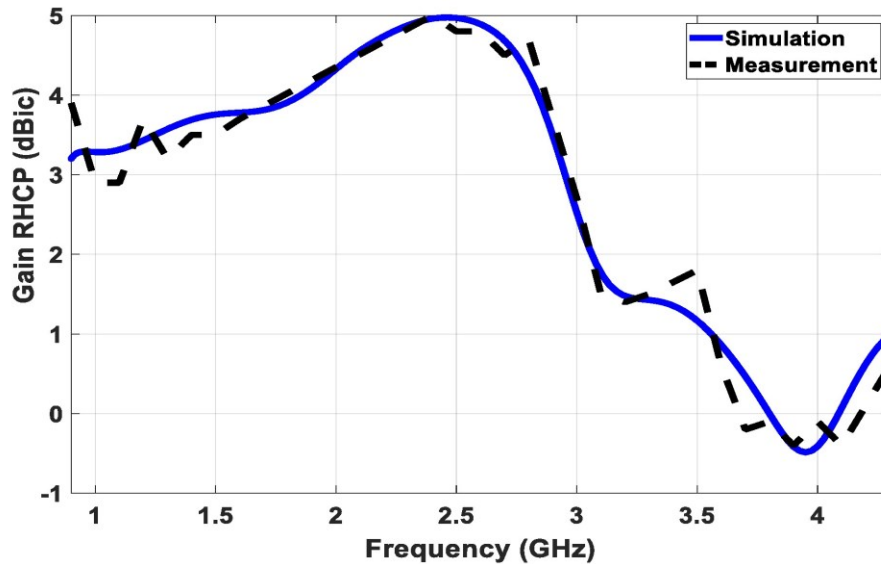


Figure 2.14: Simulated and measured RHCP gain of the proposed antenna.

Chapter 2: A Low-profile Wideband Circularly Polarized CPW Slot Antenna

Moreover, by increasing the dielectric constant of the substrate and keeping the thickness unchanged, the RHCP gain of the proposed antenna decreases especially in the upper frequencies.

The normalized simulated and measured radiation patterns for three different frequencies of 1.6, 2.4, and 3.1 GHz have been plotted in two different planes of $\phi = 0^\circ$ and $\phi = 90^\circ$ in Fig. 2.15. Also, the widest AR beamwidth of the proposed antenna is about 60° which occurs at 1.4 GHz.

Finally, the proposed antenna is compared with the recent state-of-art designs in terms of antenna size, impedance and AR bandwidth. Also, the permittivity of the substrates are included. Table 2-1 shows the comparison between the wideband CP antennas in literature and the proposed CPW slot antenna.

As can be seen, the antenna outperforms the state-of-art designs in terms of impedance and AR bandwidth. Also, the size of the antenna is small considering the impedance and AR bandwidths. The overlapping impedance and AR bandwidth is about 112 % (0.9-3.2 GHz), which outperforms the other reported designs. This high overlapping impedance and AR bandwidth is very useful in many applications.

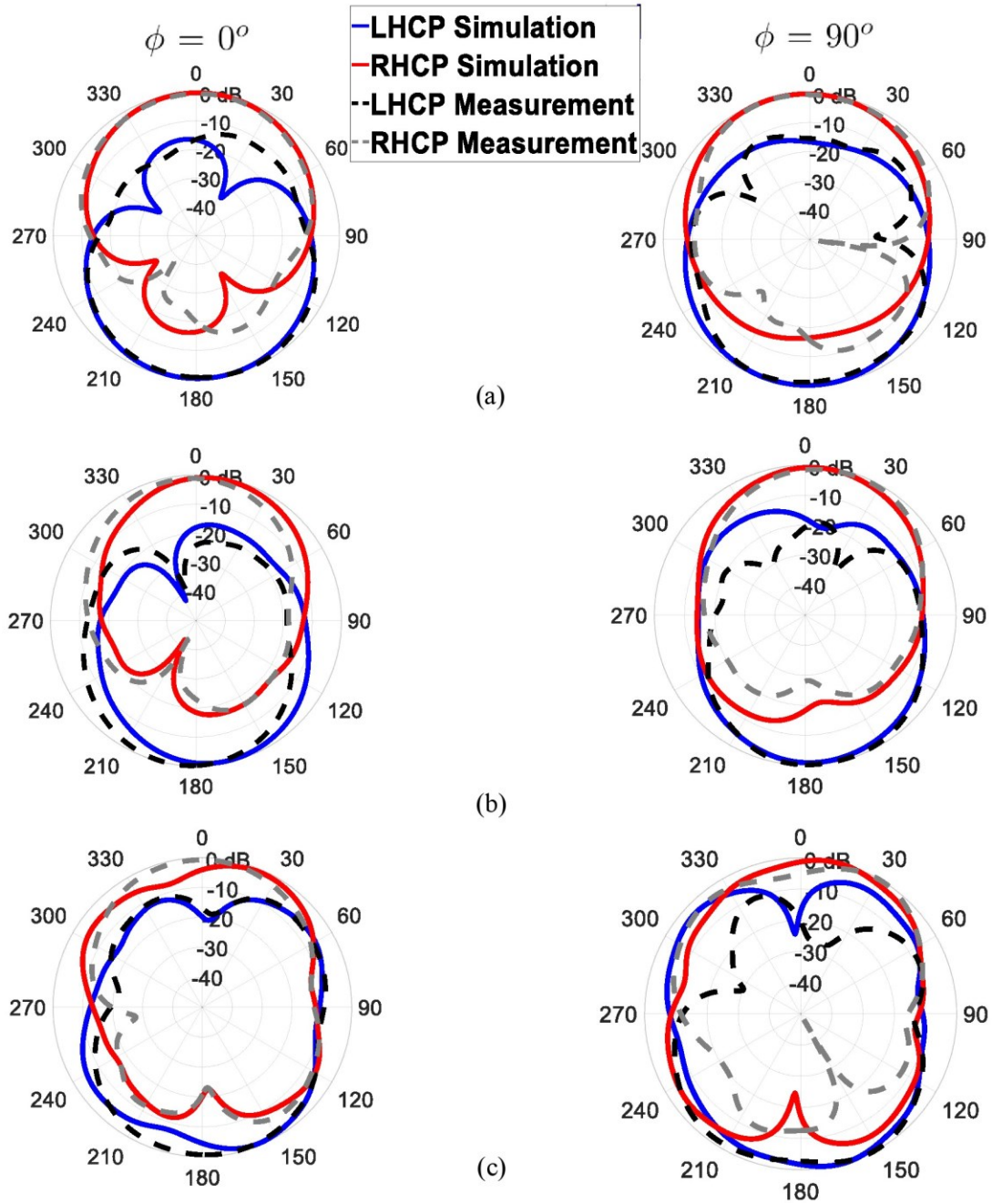


Figure 2.15: Simulated and measured normalized radiation patterns of the proposed antenna for two different planes of $\phi = 0^\circ$ and $\phi = 90^\circ$ at, (a) 1.6 GHz, (b) 2.4 GHz, (c) 3.1 GHz.

Table 2-1: Comparison between some wideband CP antennas in literature and the proposed CPW slot antenna

Ref	Size (λ_0^2)	F_{ope} (GHz)	Impedance BW (%)	AR BW (%)	ϵ_r
[42]	0.09	4.4-6.7	84	41.3	2.2
[43]	0.15	4.4-7.7	55	42.6	4.4
[44]	0.24	2-12	142	54	3.5
[45]	0.4	2.4-6.4	91	89	3.55
[46]	1	2.7-13	132	32.2	4.4
[47]	0.14	1.8-4.5	86	50	2.55
[48]	0.11	2-6	111	27	4.4
[49]	0.43	1.73-3.11	57	39	2.55
[50]	0.09	3.2-8.4	89	81	3.38
[51]	0.11	1.85-6	108	107	4.6
This work	0.07	0.9-4.2	129.5	112	6.15

λ_0 is the free space wavelength at the lowest operating frequency.

F_{ope} is the operating frequency of the antenna.

2.4 Conclusion

A simple low-profile wideband CP slot antenna has been proposed. The antenna consists of three slots and a feedline. The measured impedance and AR bandwidths of the antenna are 129.5 % (0.9-4.2 GHz) and 112 % (0.9-3.2 GHz), respectively. The size of the antenna is about $0.27\lambda_0 \times 0.27\lambda_0 \times 0.002\lambda_0$ at the lowest frequency of measured bandwidth, which outperforms other designs in the literature in terms of impedance and AR bandwidth. The antenna is very suitable for RFID, GNSS, WLAN and WiMAX frequency bands of interest. As the antenna structure is simple, it can be redesigned in order to be used in different frequency bands. The peak RHCP gain of the antenna is 5 dBic and the 3-dB gain bandwidth is from 0.9 GHz to 3.05 GHz (108 %).

Therefore, in this step, we have designed an antenna covering GNSS/GPS frequency bands both in terms of impedance and axial ratio bandwidths.

In the next step, an antenna having the above-mentioned characteristics, plus a high FBR is going to be designed to get closer to the end goal. Also, the effects of full and defected reflectors on the FBR are going to be investigated in more details.

3. Chapter 3: Compact Dual-Band Circularly Polarized Antenna with Octagonal-Shaped Slotted Reflector for GNSS Applications

3.1 Introduction

In this chapter, a compact dual-band CP antenna working in GNSS frequency bands and especially designed for GPS L2 and L1 bands is proposed. The antenna is low-profile, having a low height between the radiator and the reflector. The main novelty of the current work is the introduction of an octagonal slotted reflector which increases the FBR in both GPS L2 and L1 bands significantly, while maintaining the performance of the antenna proper and acceptable both in terms of reflection coefficient and AR. By changing some specific parameters, the antenna is capable to have high FBR in other frequencies as well. In addition, the reflector can enhance the RHCP gain of antenna in the entire bandwidth. The chapter falls into four main sections. Section 3.2 talks about the geometry and analysis of the proposed antenna. In Section 3.3, fabricated prototype and the experimental results are discussed. Finally, the chapter is concluded in Section 3.4.

3.2 Antenna Geometry and Analysis

3.2.1 Antenna Configuration

The geometry of the proposed antenna is shown in Fig. 3.1 which is designed on Rogers RO3006 substrate with the relative permittivity of $\epsilon_r=6.15$ and the thickness of 0.64 mm. The reflector is also printed on the same substrate with the same thickness. The antenna consists of a single-layer radiating patch fed by a coplanar waveguide (CPW) line at the top layer, followed by a reflector in the bottom layer. The input is matched to a 50Ω feedline. The combination of the radiating patch and the reflector forms the proposed antenna. The radiating patch consists a rectangular strip etched on the top side of the substrate in the L-shaped slot. The reflector has a symmetric octagonal-shaped slot in the middle, having different side values. The distance between the antenna and the reflector is chosen to be $H=30\text{mm}$, which is $0.117\lambda_0$ at the lowest frequency band. Simulations are performed using ANSYS High Frequency Structure Simulator (HFSS). Parameters of the proposed antenna are shown in Table 3-1 (all the values are in mm).

3.2.2 Antenna Analysis

In order to analyze the principal of operation of the proposed antenna, three different states are investigated. In state 1, the radiator does not have any reflector plane. State 2 shows the radiator while a full reflector plane has been placed under the antenna with the same distance of "H". Finally, state 3 shows the proposed antenna with the slotted reflector plane.

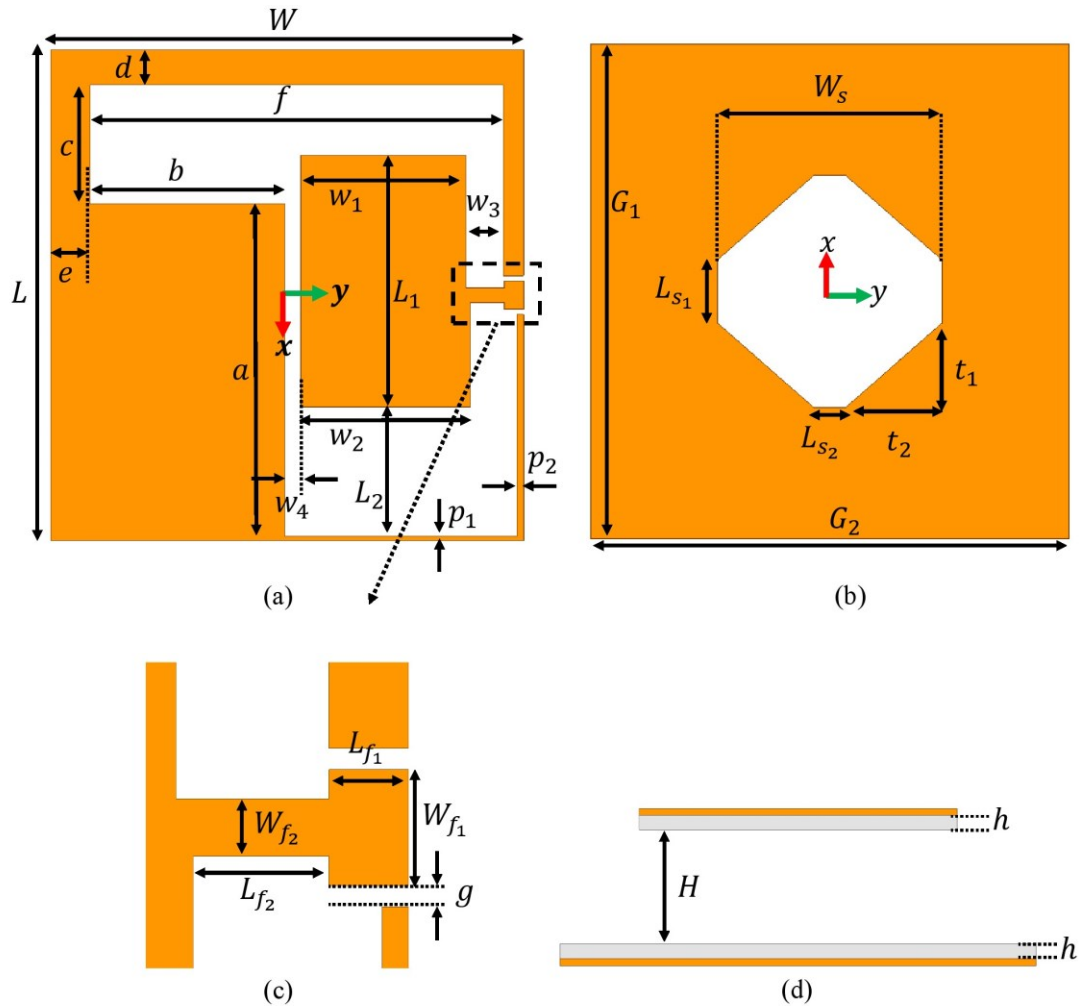


Figure 3.1: Geometry of the proposed antenna, (a) top view, (b) bottom view, (c) enlarged feeding section, (d) side view.

Fig. 3.2 depicts the simulation results of states 1-3 in terms of reflection coefficient, axial ratio, and FBR. In state 1, the antenna shows a wide impedance bandwidth with a resonance at the frequency of 1.35 GHz. By placing a full reflector plane at a distance of 30 mm below the antenna, the operating frequency bandwidth shifts toward lower frequencies (state 2), with two resonance frequencies at 1.21 GHz and 1.44 GHz. Finally, by introducing the slotted reflector (proposed antenna-state3), resonances shift toward 1.2 GHz and 1.38 GHz, respectively. Placing the full and slotted reflector planes under the radiator have significant impacts on the AR and FBR

Chapter 3: Compact Dual-Band Circularly Polarized Antenna with Octagonal-Shaped Slotted Reflector for GNSS Applications

(see Fig. 3.2 (b) and (c)). As shown, by adding the full reflector, the FBR improves about 11.3 dB and 15.6 dB at GPS L2 and L1 bands, respectively. However, the AR is still not appropriate. To overcome this problem, an octagonal-shaped slot is etched at the center of the reflector, designed in such a way that it improves the FBR in the desired frequency band. As a result, the simulated performance of antenna improves to an AR of 1.9 dB and 1.8 dB, and FBR of 20.5 dB and 21.2 dB at GPS L2 and L1 bands, respectively.

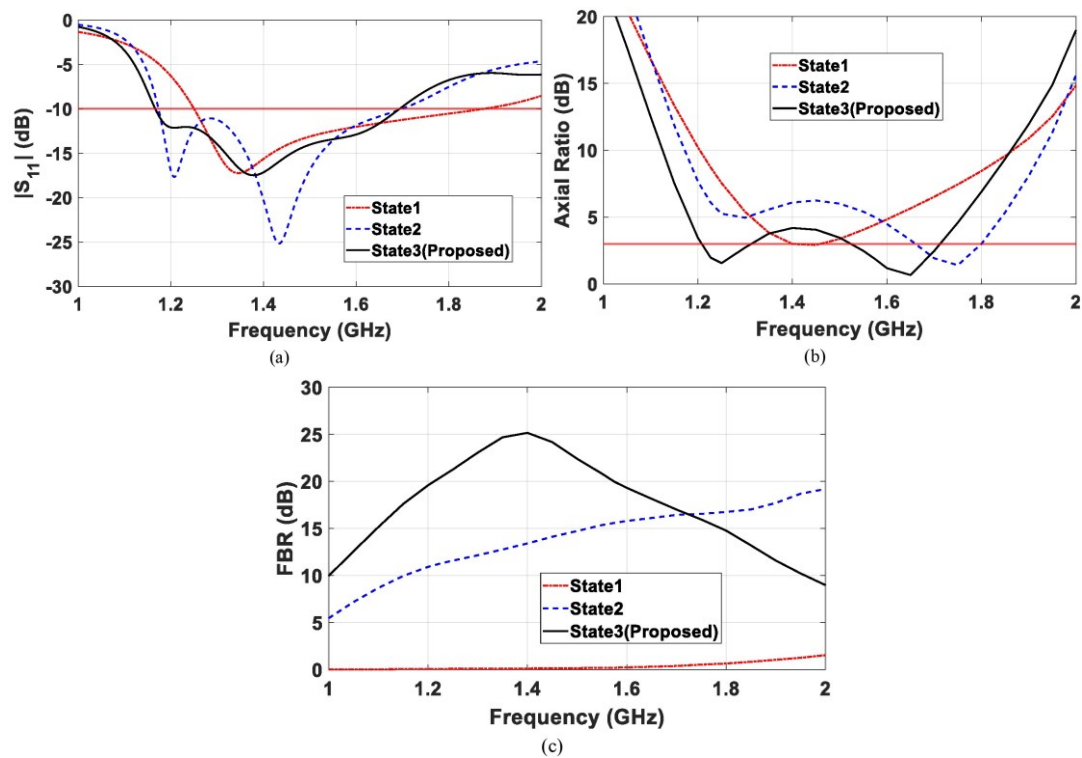


Figure 3.2: Reflection coefficient, axial ratio, and FBR of different states of the antennas, (a) reflection coefficient, (b) axial ratio, (c) FBR.

Since the distance between the reflector plane and the radiator is small (about $0.117\lambda_0$ at the lowest frequency bands of interest), by exciting the radiator, the electromagnetic fields are coupled to the reflector plane, causing surface currents to be induced on the reflector. Fig. 3.3 shows the absolute magnitude ratio of two electric field components of E_x and E_y and their phase difference for states 1-3. To have circular polarization,

Chapter 3: Compact Dual-Band Circularly Polarized Antenna with Octagonal-Shaped Slotted Reflector for GNSS Applications

two requirements should be fulfilled. First, the magnitude ratio of E_x and E_y should be equal. Second, the two electric field components should have 90 degrees phase difference at the desired frequency. As can be seen in Fig. 3.3, the absolute magnitude ratio of E_x and E_y for state 1 is very close to 1 for the entire bandwidth. However, the phase difference is not appropriate for making circular polarization. The only expected circular polarization can occur around 1.4 GHz since the phase difference is around 90° , which can be verified from the axial ratio plot (see Fig. 3.2(b)). That is almost the same for state 2 in which the magnitude ratio of E_x and E_y are close to each other, while the phase difference cannot cause circular polarization, but only around 1.75 GHz. Ultimately, the octagonal-shaped slotted reflector (state 3) causes a dual-band circular polarization in the desired GPS L2 and L1 bands by changing the phase difference to the appropriate ones.

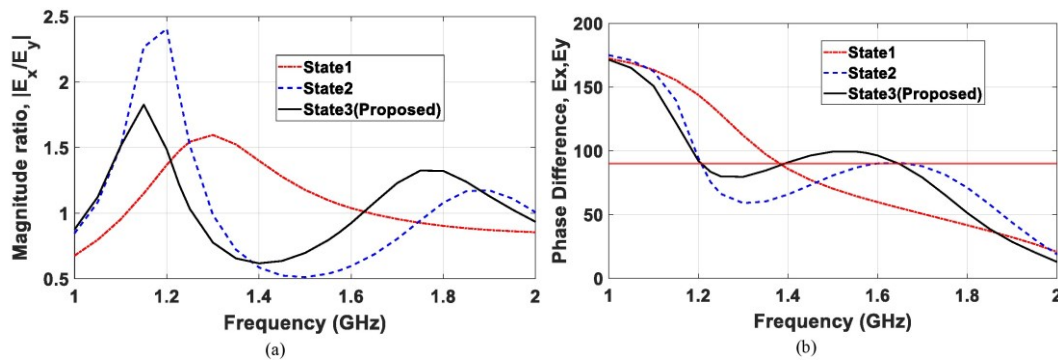


Figure 3.3: Magnitude ratio and phase difference of orthogonal field components E_x and E_y for different states, (a) magnitude ratio, (b) phase difference (the unit is in degree).

CP mechanism of the proposed antenna can be investigated by plotting the surface current distribution of the proposed antenna on the radiator. Fig. 3.4 demonstrates the surface currents and the vector sum of the currents at four different time instants at GPS L2 center frequency. Red arrows show the local surface current vector sum, and

Chapter 3: Compact Dual-Band Circularly Polarized Antenna with Octagonal-Shaped Slotted Reflector for GNSS Applications

the black arrows show the total vector sum of the surface currents. As can be seen, the black arrows rotate 90 degrees in each step. The counter-clockwise rotation of the black arrows as the time propagates indicates the RHCP wave radiation of the proposed antenna.

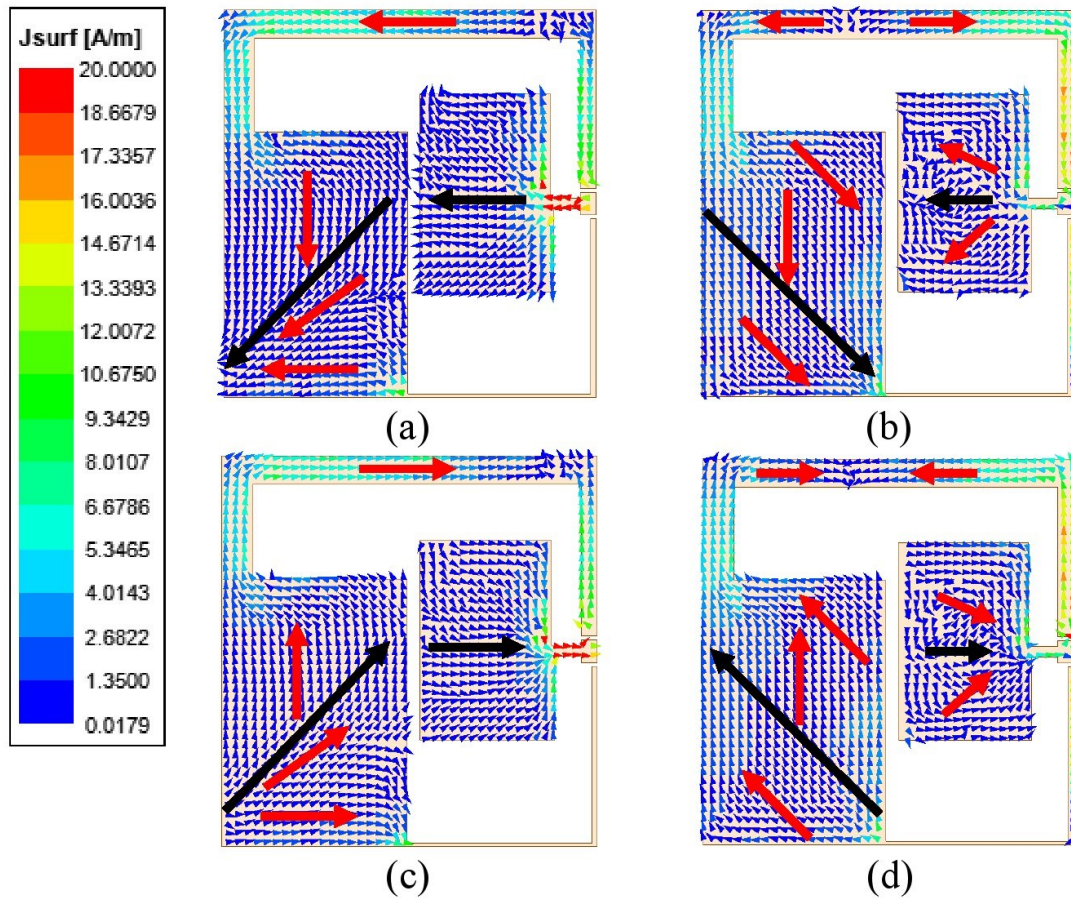


Figure 3.4: The surface current distribution of the proposed antenna at 1.227 GHz, (a) 0°, (b) 90°, (c) 180°, (d) 270°.

To show how the slotted reflector help to improve the RHCP and decrease the LHCP gains (and consequently improve the FBR), the electric field distribution of the octagonal-shaped slot is illustrated in Fig. 3.5. The counter-clockwise rotation of the electric fields is the same as the rotation of the surface currents of the radiator. This

infers that the currents are induced on the reflector (which also cause the electric field at the slot) in a way that they increase the RHCP and decrease the LHCP wave.

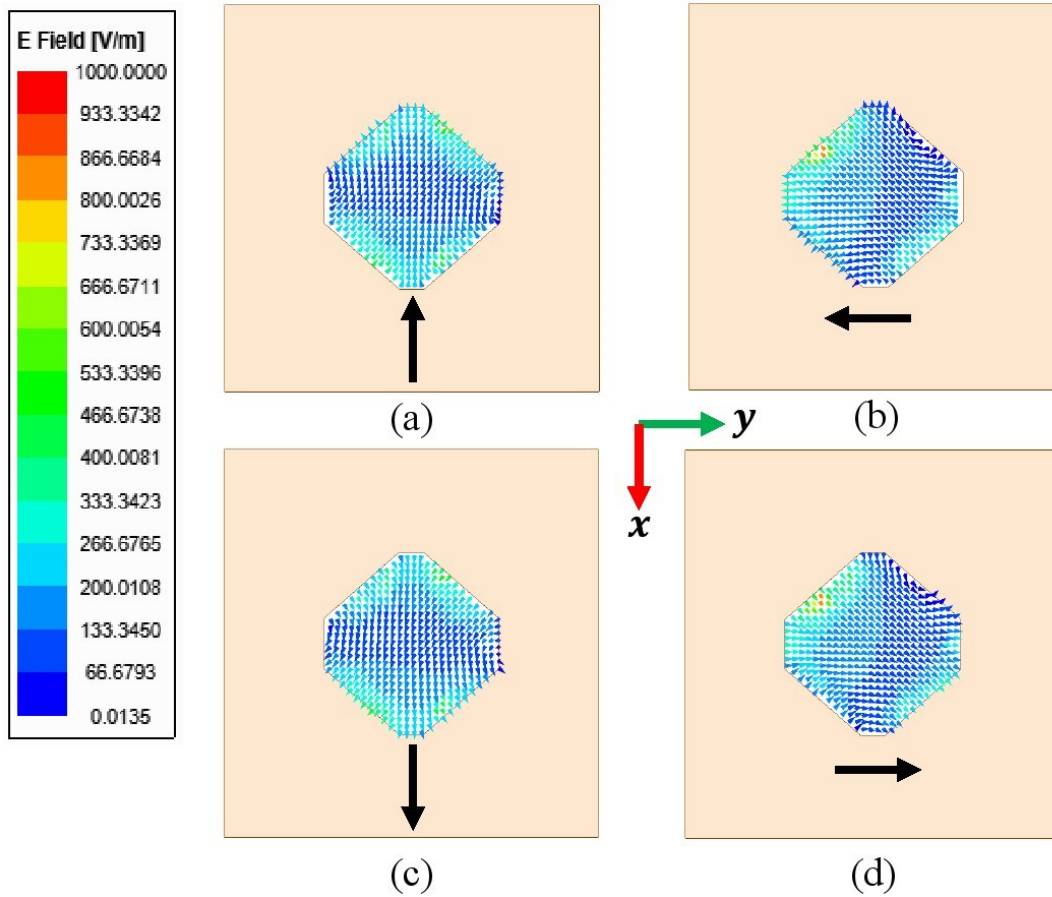


Figure 3.5: The electric field distribution at the octagonal-shaped slot from the top view at 1.227 GHz, (a) 0°, (b) 90°, (c) 180°, (d) 270°.

3.2.3 Parametric Study

In this section, the effects of different parameters on the performance of the antenna are investigated by simulations. Fig. 3.6 shows the results of different values of "e" on reflection coefficient and axial ratio. By increasing the value of "e", the frequency bandwidth shifts toward upper frequencies, while the bandwidth remains almost the same (with a very slight change). Increasing the value of "e" will cause an increase in

both the beginning and the end of impedance bandwidth. Additionally, by increasing "e", the magnitude ratio of E_x and E_y decreases and their phase difference increases, which cause a worse axial ratio in the entire bandwidth.

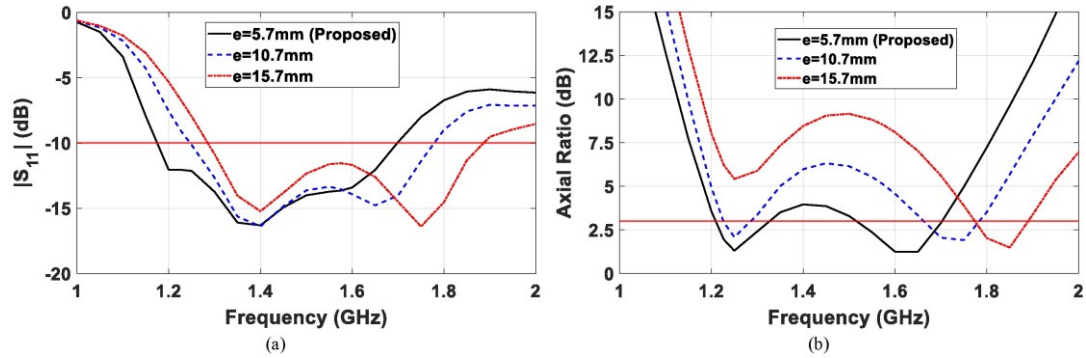


Figure 3.6: Simulation results of the proposed antenna for different values of "e", (a) reflection coefficient, (b) axial ratio.

Another investigated parameter is " W_s ", which is the width (and length) of the octagonal-shaped slot in the reflector. The parametric study of " W_s " represents that by changing the size of the slot, the minimum LHCP gain at $\theta = 180^\circ$ alters throughout the frequency band, as shown in Fig 3.7. In other words, by optimizing the size of the slot, it is possible to obtain the maximum FBR at any desired frequency in the entire frequency bandwidth. The proposed antenna is compared with previously reported GPS dual-band antennas in Table 3-2. The antennas are compared in terms of size, impedance and axial ratio bandwidths, FBR, gain, and FR. Considering all the factors together, the proposed antenna outperforms the other works in literature, specially by its FBR.

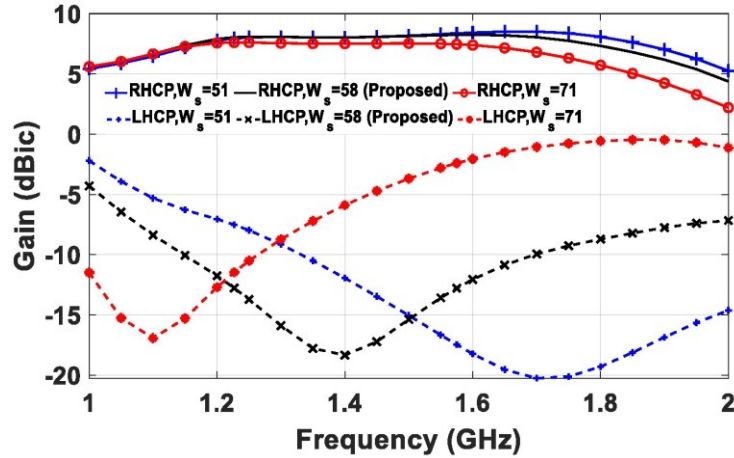


Figure 3.7: Simulation results of RHCP and LHCP gain of the proposed antenna for different values of " W_s " at $\theta = 0^\circ$, $\phi = 0^\circ$ and $\theta = 180^\circ$, $\phi = 0^\circ$ respectively.

Table 3-1: Parameters of Antenna Configuration (values in mm).

Parameter	Value	Parameter	Value	Parameter	Value
W	69.9	L	72.8	d	5.3
a	49.3	b	28.8	c	17.6
e	5.7	f	61.2	w_1	24.5
w_2	25.1	w_3	5.5	w_4	2.3
L_1	37.3	L_2	19.1	p_1	0.6
p_2	1	G_1	127.7	G_2	123.5
W_s	58	L_{s1}	16.2	L_{s2}	8
t_1	22	t_2	25	g	0.8
W_{f1}	4.2	W_{f2}	2.1	L_{f1}	2.9
L_{f2}	5	h	0.64	H	30

Table 3-2: Comparison between dual-band CP antennas in literature and the proposed antenna

Design	Size (λ_0^3) ¹	IBW	ARBW	FBR	Gain	FR
		(L,U) ^{2,3} (%)	(L,U) ^{2,3} (%)	(L,U)	(L,U)(dBic)	
[7]	0.56×0.56×0.05	28.5	2 , 2	NA	6 , 7	1.28
[8]	0.41×0.41×0.09	3.7 , 1.2	0.9 , 0.6	11.7 , 10	6.5 , 6	1.28
[52]	0.34 λ_0^2 ×0.016	1.2 , 1.5	NA	NA*	7.2 , 6.5	1.48
[53]	0.31×0.31×0.007	3 , 2.4	1.1 , 1.04	NA	4 , 1.2	1.77
[54]	0.58×0.58×0.036	3 , 14.9	1.98 , 3.1	17 , 17	6.2 , 6.5	1.66
[55]	0.46×0.46×0.09	16 , 12.5	6.9 , 0.6	NA	1.45 , 1.1	1.28
[56]	0.57×0.57×0.17	34.4	19.2 , 18	NA	4 , 4	1.28
[57]	0.41×0.41×0.03	16.1 , 11.2	2.1 , 2	NA	6.5 , 6.8	1.18
[58]	0.106 λ_0^2 ×0.105	0.6 , 0.8	0.6 , 0.8	NA	2.6 , 3.4	1.28
[59]	0.53×0.53×0.13	40.5	6.56 , 7.74	11 , 16**	7.7 , 8.1	1.28
[60]	1.51 λ_0^2 ×0.02	16.6	1.35 , 1.45	14.93 , 18.3	5.8 , 4	1.08
[61]	0.36×0.31×0.01	15.1 , 23	7.2 , 15.6	0 , 0	2.4 , 3	2.24
[62]	0.2×0.2×0.04	40.2	24 , 14.5	6.2 , 5.8	1.57 , 3	1.28
[63]	0.45×0.38×0.01	71.6	27.4 , 7.1	0 , 0	2 , 2.5	1.38
This Work	0.49×0.48×0.117	36	8 , 11.7	20.5 , 21.2	8 , 8.2	1.28

¹ λ_0 is the free space wavelength at the lowest operating frequency.

² IBW: Impedance bandwidth, ARBW: Axial ratio bandwidth.

³ “L” is the lower and “U” is the upper band.

* NA in this column refers to either the FBR is not available, or the cross polarization gain has not been reported.

** Obtained from the figures in the paper.

3.3 Fabricated Prototype and Experimental Results

The fabricated prototype is shown in Fig. 3.8. The measurements have been done in an anechoic chamber (see Fig. 3.8 (c)). The simulation and measurement results of the reflection coefficient and axial ratio of the proposed antenna are illustrated in Fig. 3.9. The results show that the 10-dB impedance bandwidth of the antenna is about 36 % (1.17-1.69 GHz). Also, the 3-dB axial ratio bandwidth is about 8 % (1.21-1.31 GHz) in the lower band and 11.7 % (1.53-1.72 GHz) in the upper band. Furthermore, the simulated and measured results of RHCP gain at $\theta = 0^\circ, \phi = 0^\circ$ and LHCP gain at $\theta = 180^\circ, \phi = 0^\circ$ are depicted in Fig. 3.10. The RHCP gain at $\theta = 0^\circ$ at GPS L2 and L1 bands are 8 dBic and 8.2 dBic, respectively, while the LHCP gain at $\theta = 180^\circ$ at GPS L2 and L1 bands are -12.5 dBic and -13 dBic, respectively. It is worth mentioning that the 3-dB gain bandwidth of the antenna is about 64.8 % (1- 1.96 GHz), which is almost stable in the entire bandwidth.

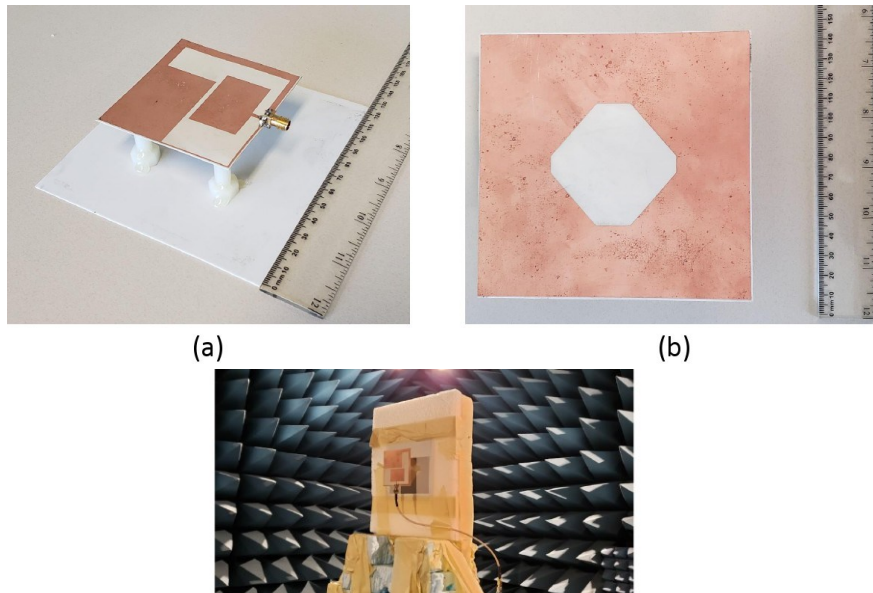


Figure 3.8: Fabricated prototype and measurement of the proposed antenna, (a) isometric view, (b) bottom view, (c) measurement of the proposed antenna in anechoic chamber.

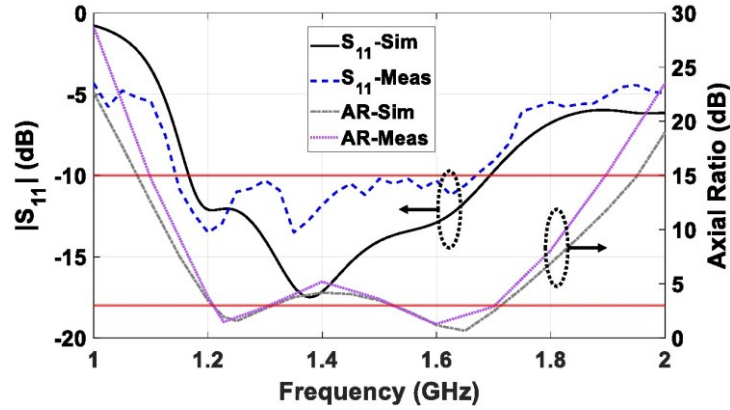


Figure 3.9: Simulation and measurement results of reflection coefficient and axial ratio the proposed antenna.

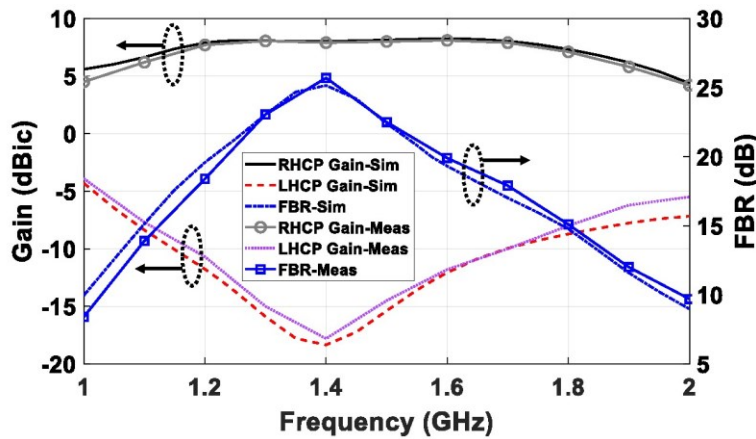


Figure 3.10: Simulation and measurement results of RHCP and LHCP gain of the proposed antenna at $\theta = 0^\circ, \phi = 0^\circ$ and $\theta = 180^\circ, \phi = 0^\circ$, respectively along with the FBR.

The radiation patterns of the proposed antenna at GPS L2 and L1 frequency bands at two different planes of $\phi = 0^\circ$ and $\phi = 90^\circ$ are presented in Fig. 3.11. As shown, a FBR of about 20.5 dB and 21.2 dB at L2 and L1 bands are acquired. Moreover, the HPBW is about 75° at both $\phi = 0^\circ$ and $\phi = 90^\circ$ at L2 band while a HPBW of 75° and 80° is obtained at L1 band at $\phi = 0^\circ$ and $\phi = 90^\circ$ planes respectively, which is acceptable for the desired applications. Therefore, the results show that the proposed antenna is a good candidate for GNSS (and specifically for GPS) applications.

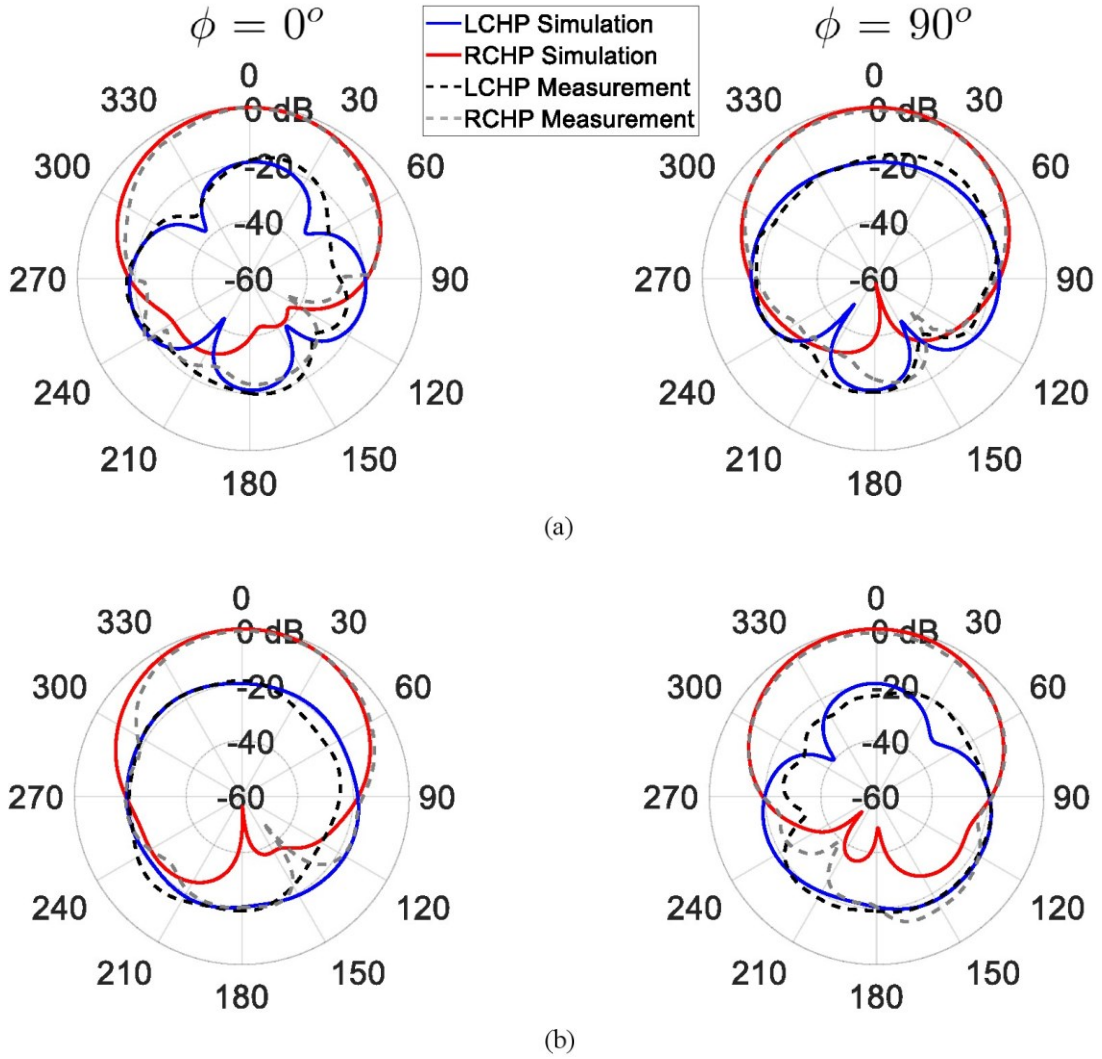


Figure 3.11: Normalized radiation patterns of the proposed antenna in two different frequencies of GPS L2 and L1 bands at two different planes of $\phi = 0^\circ$ and $\phi = 90^\circ$.

3.4 Conclusion

In this chapter, a dual-band CP antenna with slotted reflector for GPS applications is proposed. The antenna consists of a radiator and a reflector with a distance of 30 mm from the radiator, which is about $0.117\lambda_0$ at the lowest frequency bands of interest. Also, the dimension of the antenna is $0.28\lambda_0 \times 0.27\lambda_0$ and the reflector size is $0.49\lambda_0 \times 0.48\lambda_0$. The reflector consists of an octagonal-shaped slot which is responsible for decreasing the maximum value of LHCP gain, resulting in the enhancement of FBR to about 20.5 dB and 21.2 dB at GPS L2 and L1 bands, respectively. By tuning and optimizing the size of the slot, the antenna is capable to produce a high FBR in other frequencies as well. The 10-dB impedance bandwidth of the antenna is about 36 % (1.17-1.69 GHz). Also, the 3-dB axial ratio bandwidths of 8 % (1.21-1.31 GHz) in the lower band and 11.7 % (1.53-1.72 GHz) in the upper band have been obtained. The 3-dB gain bandwidth of the antenna which is about 64.8 % (1 - 1.96 GHz), shows a sustainability of the gain values in the entire bandwidth. The maximum RHCP gain of the antenna is about 8 dBic and 8.2 dBic at GPS L2 and L1 bands, respectively. The HPBW is obtained for about 75° at the frequency bands of interest.

Thus, in this step, a dual-band CP antenna covering the GNSS/GPS frequency bands with a high FBR has been proposed. The only remaining desired features to achieve the research aims are to have tilted beam and transparency.

In the next two chapters, two different antennas having all the desired features and characteristics have been proposed.

4. Chapter 4: Wideband Transparent Circularly Polarized Rectangular Slot GNSS Antenna for Vehicular Applications

4.1 Introduction

In this chapter, a novel single-layer coplanar waveguide (CPW)-fed wideband circularly polarized transparent antenna with tilted beam is proposed. The antenna is designed and can be used for any inclined surfaces which need LoS applications. Here, the proposed antenna is designed especially for GPS location tracking for vehicular platforms. Since most windshields are inclined for around 30 degrees in elevation, the beam of the antenna is also designed for a tilt of about 30 degrees. In this case, the maximum RHCP gain, which is vital for GPS applications, occurs at zenith when it is mounted on the windshield. Furthermore, to increase the FBR, a transparent reflector is designed and fabricated in order to be placed inside the car, on the dashboard or glove compartment of the vehicle. The antenna exhibits a wide 10-dB impedance bandwidth and also a wide 3-dB axial ratio bandwidth covering all GNSS frequencies. Moreover, the 3-dB gain bandwidth of the antenna shows a stable bandwidth throughout the desired frequency band. Obtaining all the characteristics together in a single-layer antenna is the main novelty of this work. To analyze the antenna's mechanism of operation, characteristic mode analysis (CMA) is performed, which has been an interesting and attractive analysis among the researchers in recent years (see the appendix).

Chapter 4: Wideband Transparent Circularly Polarized Rectangular Slot GNSS Antenna for Vehicular Applications

The rest of the chapter is organized as follows. Section 4.2 introduces the antenna configuration and the development stages. Section 4.3 talks about the antenna analysis and introduction of transparent reflector. The fabrication process and discussion of results are represented in Section 4.4. Finally, the chapter is summarized in Section 4.5. The characteristic mode analysis of the proposed antenna is presented in the appendix.

4.2 Configuration and Development of the Proposed Antenna

4.2.1 Antenna Geometry

The configuration of the proposed antenna is shown in Fig. 4.1. The single-layer single-sided antenna is designed on a transparent glass substrate with a relative permittivity of $\epsilon_r=5.5$ and a thickness of 1mm, with dimensions of $149 \times 99 \text{ mm}^2$. The CPW line is fed by a coaxial feedline with an input impedance of 50Ω . The exact dimensions of different sections are shown in Fig. 4.2. Another key point to remember is the fact that since the antenna is intended to be transparent, a mesh grid is used throughout the antenna instead of full conductive layer. Most of the mesh grid elements consist of square elements with a length of 5.4 mm and a width of 0.1 mm (see Fig. 4.2 (d)). In some minor areas, however, the size of mesh elements are modified corresponding to the constraints in terms of space. For calculating the transparency, the general equation for a periodic mesh grid surface with equal sized elements is defined as follows:

$$OT = \left(\frac{m}{m+n}\right)^2 \quad (1)$$

where “ m ” is the length and “ n ” is the width of mesh element (for the proposed antenna are 5.4 and 0.1 mm, respectively). Having said that, for a surface having mesh elements with different sizes, the transparency is obtained by the ratio of the whole and open areas. In this case, the transparency of the antenna is calculated for about 95 %. Furthermore, a new coordinate system is defined in which most of the simulation and measurement results are performed. The new coordinate system in which the antenna is mounted on the windshield of a car is illustrated in Fig. 4.3.

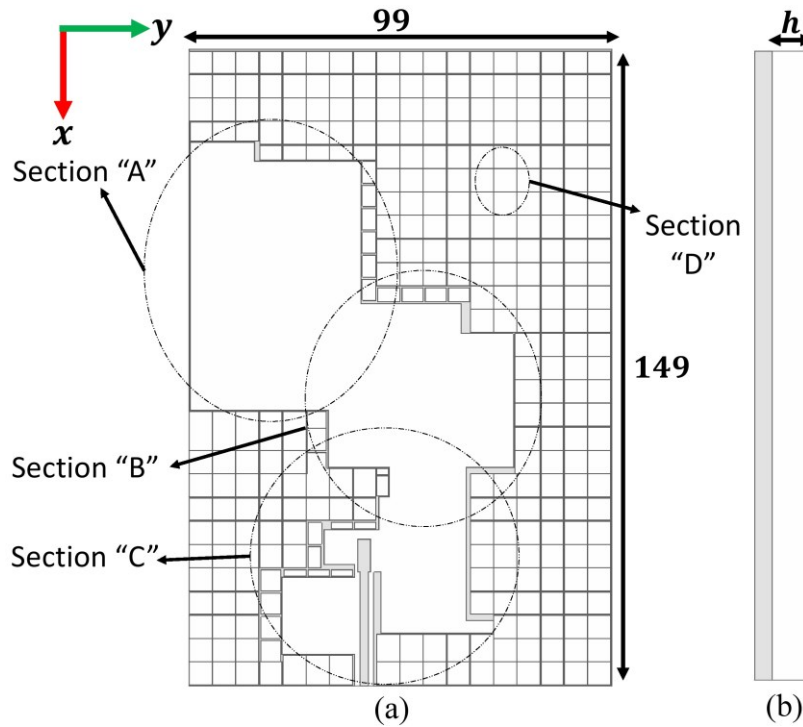


Figure 4.1: Geometry of the proposed antenna, (a) top view (b) side view. $h=1$ (dimensions in mm).

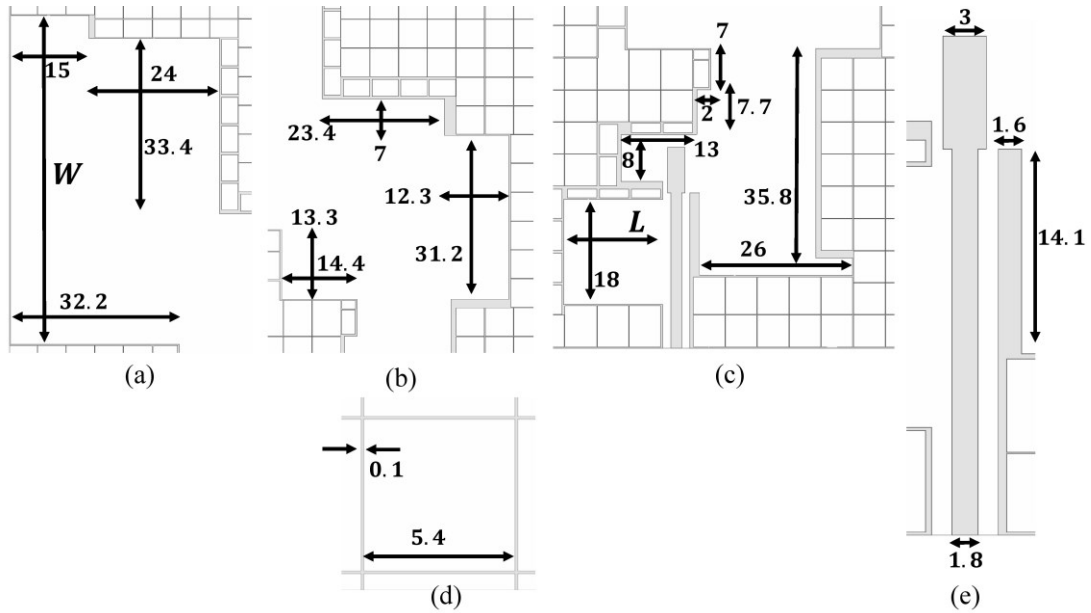


Figure 4.2: Enlarged sections of the proposed antenna, (a) section A (b) section B (c) section C (d) section D (e) enlarged section of feedline. $W=63$, $L=17$ (all dimensions are in mm).

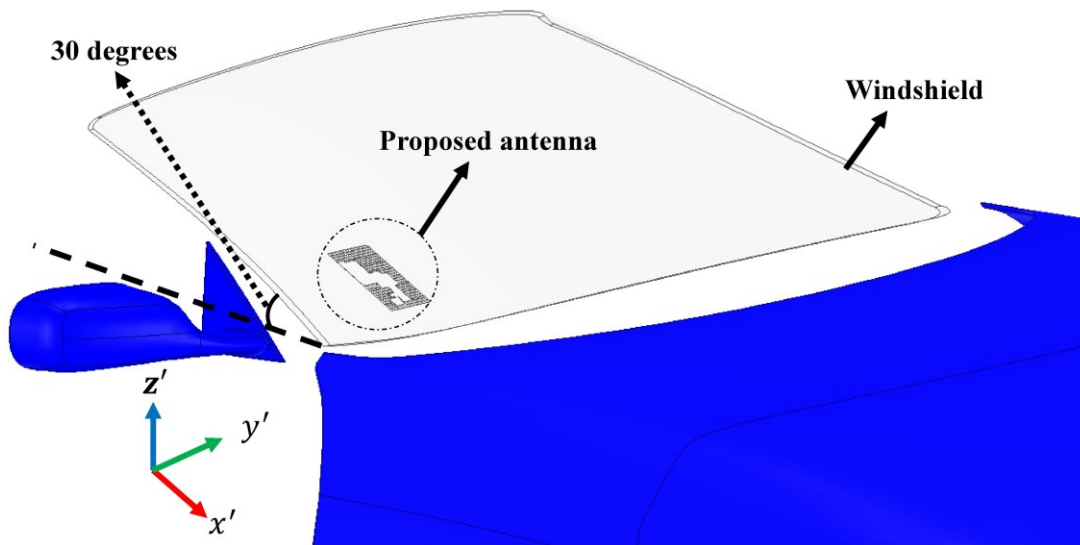


Figure 4.3: Definition of the new coordinate system while the antenna is placed on the windshield.

4.2.2 Antenna Development Stages

Five different antenna evolution stages are depicted in Fig. 4.4. Since the desired antenna should have a tilted beam, an asymmetric rectangular slot is etched on the conductive layer being fed by a CPW feedline not in the middle (see Fig. 4.4 (a)). This will result in a tilted beam in the desired frequency band since the surface current distribution is asymmetric, and causing two resonance frequencies near 1.35 GHz and 1.75 GHz. The reflection coefficient and axial ratio of all antennas are shown in Fig. 4.5. Also, the magnitude ratio of two orthogonal field components of E_x and E_y are demonstrated in Fig. 4.6. To reach CP, from the theory, the magnitude ratio of E_x and E_y should reach 1 with a 90° phase difference. However, since the magnitude ratio of two orthogonal field components of E_x and E_y is high, Ant1 does not radiate a circularly polarized wave. In order to overcome this problem, three rectangular strips are added at three different corners of the rectangular slot. This will cause the magnitude ratio of E_x and E_y to drop for a significant value, but still an inappropriate phase difference (PD) between E_x and E_y remains which does not form circular polarization. Therefore, in this step, another strip is added at the middle and the size of the slot is reduced in the right section and increased in the bottom section, forming Ant3 (see Fig. 4.4 (c)). Hence, the magnitude ratio and phase difference of E_x and E_y is changed to the desired, having axial ratio below 3-dB for the desired bandwidth. However, the reflection coefficient is still not acceptable. To solve the problem, some small-size slots are added to different parts of the antenna, as can be seen in Fig. 4.4 (d), creating Ant4. Finally, mesh grid is applied to the antenna to make the antenna

Chapter 4: Wideband Transparent Circularly Polarized Rectangular Slot GNSS Antenna for Vehicular Applications

transparent. It is worth mentioning that the axial ratio of different antennas are depicted in the new coordinate system. The development stages are discussed in more details in the next section.

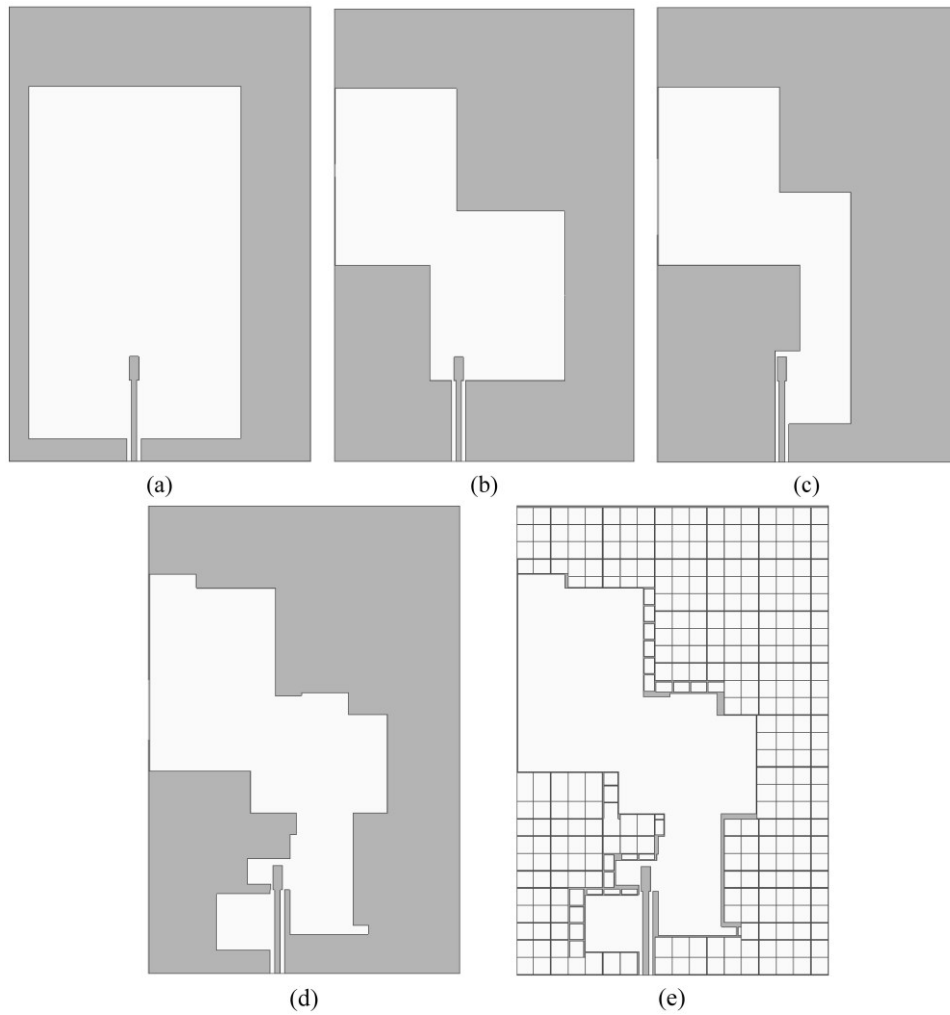


Figure 4.4: Antenna evolution stages, (a) Ant1 (b) Ant2 (c) Ant3 (d) Ant4 (e) proposed antenna

Chapter 4: Wideband Transparent Circularly Polarized Rectangular Slot GNSS Antenna for Vehicular Applications

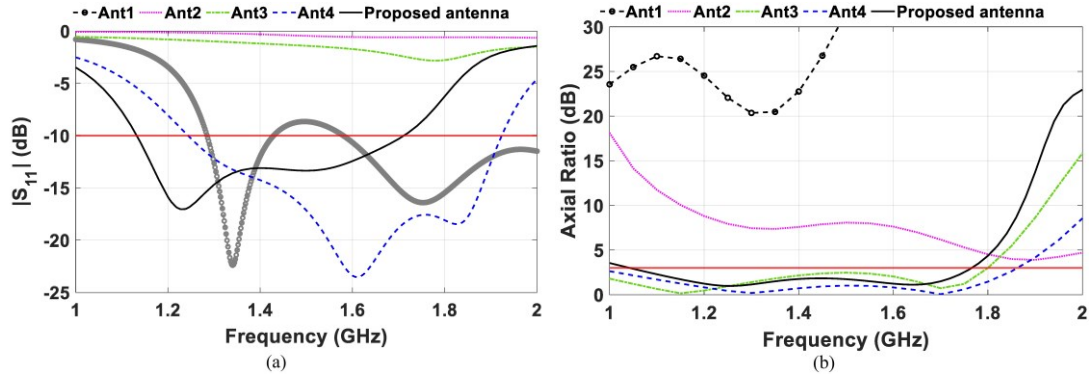


Figure 4.5: Reflection coefficient and axial ratio of Ant1-Ant4 and the proposed antenna, (a) reflection coefficient (b) axial ratio at $\theta' = 0$, $\phi = 0$.

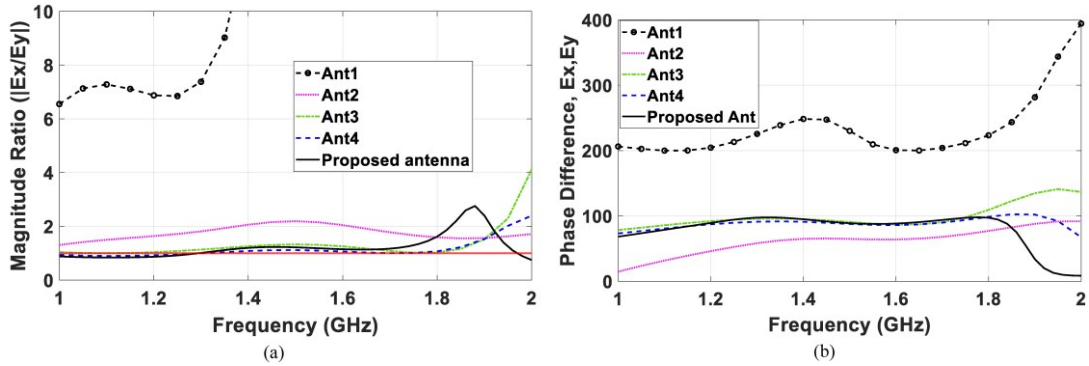


Figure 4.6: Magnitude ratio and phase difference (PD) of orthogonal field components E_x and E_y , (a) magnitude ratio, (b) phase difference (PD unit is in degree).

4.3 Antenna Analysis and Transparent Reflector

4.3.1 CP Mechanism

In this section, the CP mechanism of the proposed antenna is investigated by plotting the electric fields distribution of the antenna at four different time instants at GPS L2 center frequency band (1.227 GHz) as an example. As can be seen in Fig. 4.7, the field distribution at the middle section of the antenna is rotating as the time passes.

Chapter 4: Wideband Transparent Circularly Polarized Rectangular Slot GNSS Antenna for Vehicular Applications

The counter-clockwise rotation of the fields result in an RHCP wave radiation of the antenna. Also, the fields at the lower section of the antenna have notable contribution for producing circular polarization. As can be seen, the rotation of the lower section fields is the same as middle section in terms of the summation of field vectors pointing and being counter-clockwise in time propagation. The way that the electric fields distribution is observed has been shown in Fig. 4.7 (e).

The characteristic mode analysis (CMA) for the proposed antenna is carried out in the appendix.

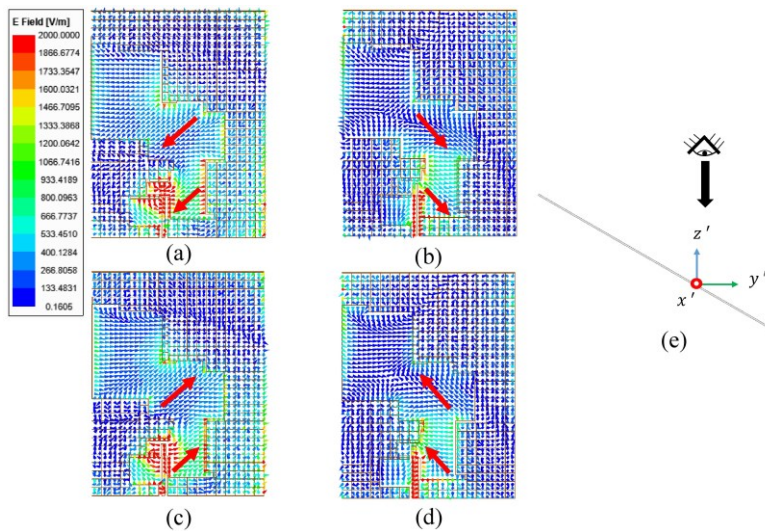


Figure 4.7: Electric fields distribution of the proposed antenna at four different time instants at GPS L2 center frequency (1.227 GHz), (a) 0° (b) 90° (c) 180° (d) 270° (e) the way proposed antenna is observed for the electric fields distribution.

4.3.2 Antenna Beam

To have a better observation of beam tilting, an antenna having two diagonal slots is investigated for observing the beam directions, shown in Fig. 4.8. This antenna is similar to Ant2, with some differences in the dimension of the slots and the overall length. The initial length of this antenna is 90 mm and increases to 150 mm (same

Chapter 4: Wideband Transparent Circularly Polarized Rectangular Slot GNSS Antenna for Vehicular Applications

length of Ant2). As shown in Fig. 4.8, by increasing the length of the antenna from upper side, the maximum beam direction of the antenna alters from $\theta = 0^\circ$ to $\theta = 25^\circ$ at 1.227 GHz, and from $\theta = 5^\circ$ to about $\theta = 30^\circ$ at 1.575 GHz at $\phi = 0^\circ$ in the primary coordinate system. Therefore, an increase in the length of the antenna causes an increase in the tilted angle of the antenna in the desired plane and frequencies. As another investigation, the RHCP beam directions of the proposed antenna for different frequencies in the primary coordinate system are demonstrated in Fig. 4.9. Increasing the operation frequency from 0.6 GHz to 1.8 GHz results in maximum beam directions from $\theta = 0^\circ$ to around $\theta = 30^\circ$ at the desired plane of $\phi = 0^\circ$, while no sensible change can be observed at $\phi = 90^\circ$. The direction of the beam is almost constant in each GNSS channel bandwidth. Hence, by choosing the desired length and performing optimization, the antenna can be used on a surface with an inclination angle rather than 30° .

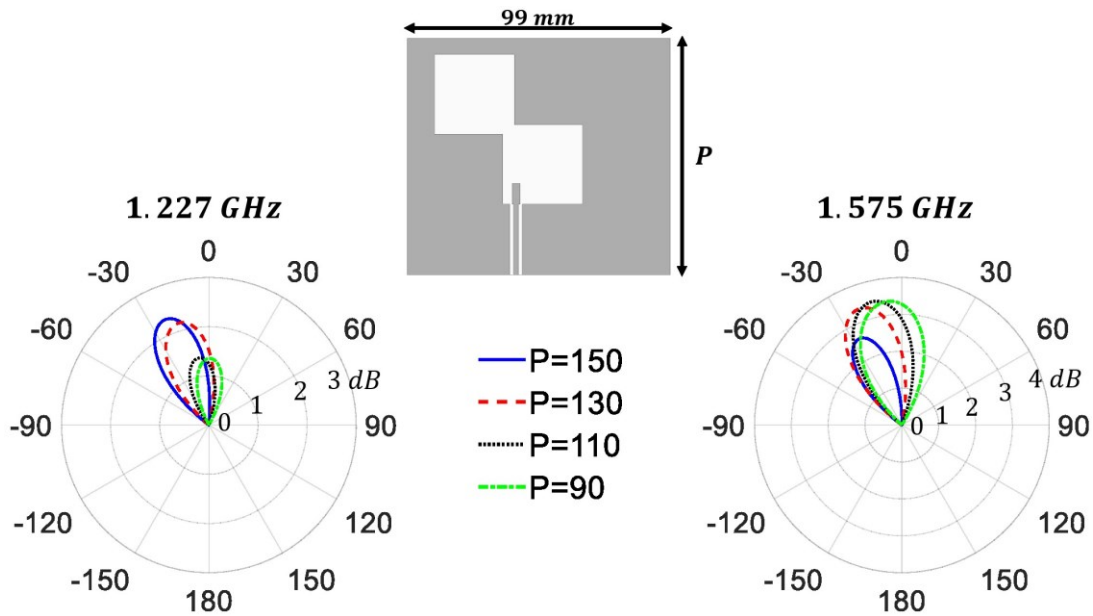


Figure 4.8: RHCP beam direction of the diagonal-slot antenna for different values of "P" in the primary coordinate system at $\phi = 0^\circ$ for two different GPS frequency bands.

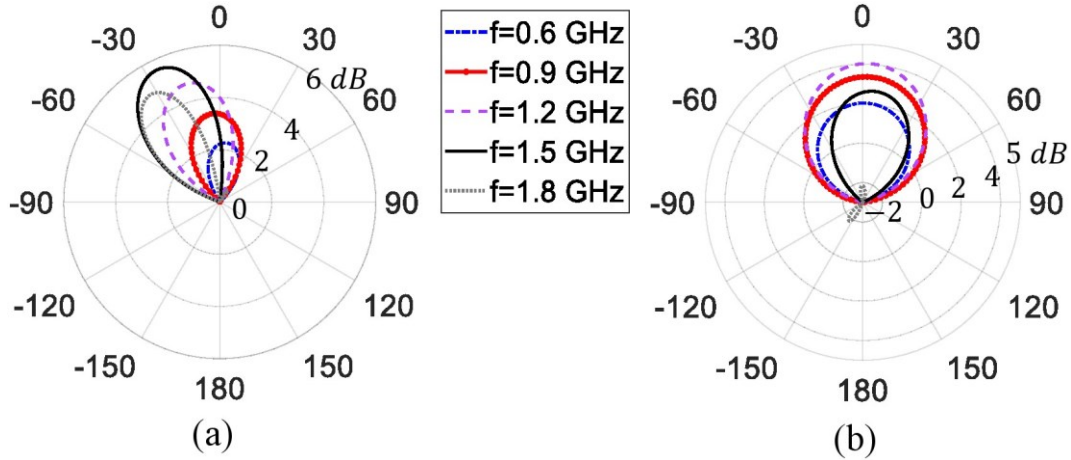


Figure 4.9: RHCP beam direction of the diagonal-slot antenna for different frequencies in the primary coordinate system at two different planes, (a) $\phi = 0^\circ$ (b) $\phi = 90^\circ$.

4.3.3 Parametric Study

Fig. 4.10 and Fig. 4.11 show the variation of two parameters of “ L ” and “ W ” and the simulation results of reflection coefficient and axial ratio against frequency. The results are obtained for Ant4 since it is very close to the proposed antenna in terms of simulation results, except the transparency. Moreover, it is easier to do the parametric study for Ant4 instead of the proposed antenna since changing the parameters of proposed antenna needs some modification in terms of mesh elements. Hence, it is preferred to carry out the study on Ant4. Fig. 4.10 shows the variation of “ L ” and the corresponding results in terms of S_{11} and axial ratio.

As discussed in section 4.2, Ant3 has a wide 3-dB axial ratio bandwidth, whereas the reflection coefficient shows that the antenna is not matched to a 50Ω input feedline. Therefore, some slots are added to Ant3 to alter the effective electrical length of main radiator slots in the antenna structure and improve the reflection coefficient while

Chapter 4: Wideband Transparent Circularly Polarized Rectangular Slot GNSS Antenna for Vehicular Applications

keeping the 3-dB axial ratio bandwidth unchanged. In order to match a circuit to a certain transmission line with a certain characteristic impedance, from the theory, introducing a matching circuit at the beginning of the circuit would be one possible solution. In this case, the capacitive and inductive effects created by the matching circuit can improve the impedance bandwidth.

One of the slots which plays the key role for 10-dB impedance bandwidth improvement is the slot with the length of “ L ”. By adding the slot, it produces some capacitive and inductive effects which can alter the input impedance seen from the input of the antenna. By changing the length of the slot, the capacitive and inductive effects change and result in a change in the input impedance of the antenna, finally causing a change in the impedance bandwidth. As can be seen in Fig. 4.10 (a), by increasing the length of the slot, the impedance bandwidth becomes wider by shifting the lower end to lower frequencies, keeping the higher end almost unchanged. The axial ratio of the antenna however does not alter in the desired frequency band (see Fig. 4.10 (b)).

Another important parameter is the width of the larger slot (“ W ”). As shown in previous section (CP mechanism), the electric fields distribution at the slots forms a circular polarization. This means that by changing the size of main slots, the axial ratio value can be different. In Fig. 4.11, the reflection coefficient and axial ratio of Ant4 for different values of “ W ” are shown. This parameter has a significant impact on the upper end of the axial ratio bandwidth, while the lower end does not change much.

Chapter 4: Wideband Transparent Circularly Polarized Rectangular Slot GNSS Antenna for Vehicular Applications

By decreasing the value of “ W ”, the axial ratio bandwidth becomes wider since the higher end of the bandwidth shift toward upper frequencies.

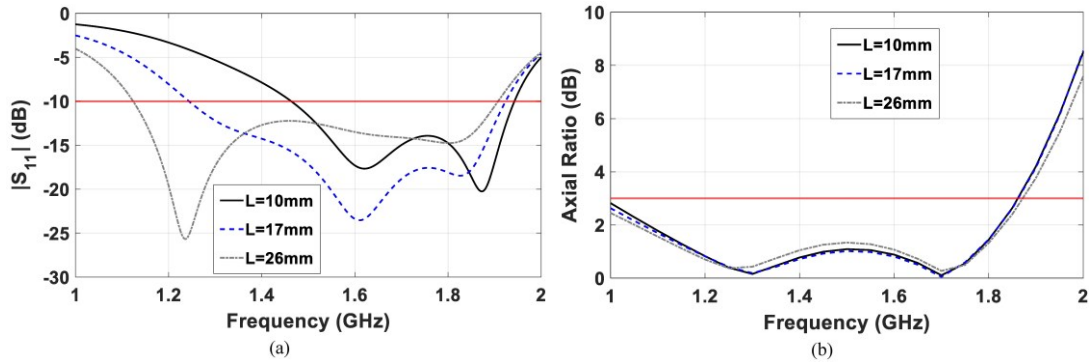


Figure 4.10: Simulation of Ant4 for different values of “ L ”, (a) reflection coefficient (b) axial ratio.

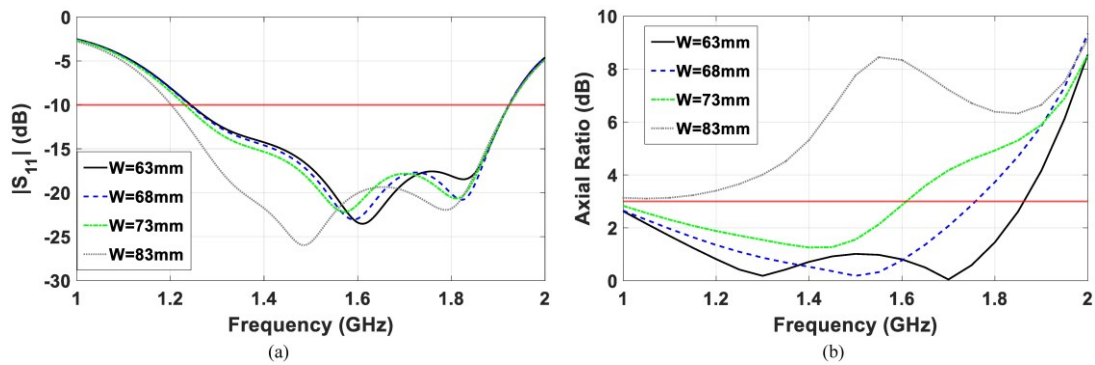


Figure 4.11: Simulation of Ant4 for different values of “ W ”, (a) reflection coefficient (b) axial ratio.

Additionally, the effects of different scales of the proposed antenna on the tilted angle in elevation plane are investigated. As shown in Fig. 4.12, by scaling the size of the antenna from the scale factors of $S=0.8$ to $S=1.1$, the tilted angle alters from $\theta = 17^\circ$ to $\theta = 33^\circ$ in the primary coordinate system. For example, scale factor of 1.1 means all dimensions of the antenna are multiplied by 1.1. The scale factor of $S=1$ is the proposed antenna. This behaviour is beneficial when the inclination angle of the

Chapter 4: Wideband Transparent Circularly Polarized Rectangular Slot GNSS Antenna for Vehicular Applications

surface (windshield here) is not exactly 30° . Therefore, by changing the scale factor parameter and performing optimization, the antenna can be used on a surface with an inclination angle rather than 30° . The RHCP radiation patterns of the proposed antenna for different scale factors in the primary coordinate system at 1.575 GHz for $\phi = 0^\circ$ plane are depicted in Fig. 4.12.

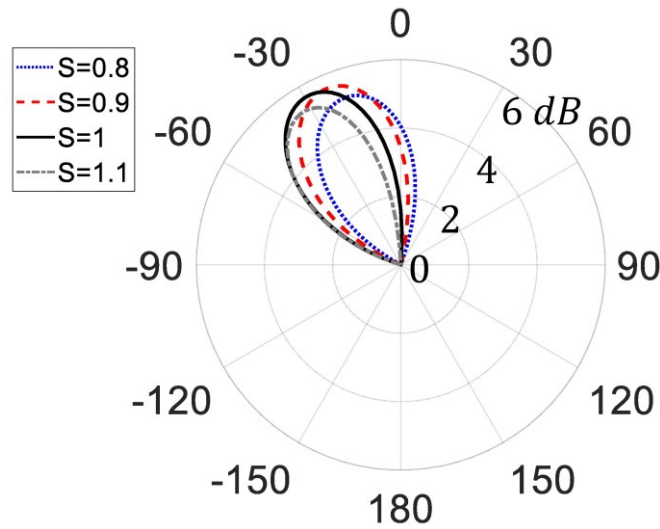


Figure 4.12: RHCP radiation patterns of the proposed antenna for different scale factors in the primary coordinate system at 1.575 GHz at $\phi = 0^\circ$.

4.3.4 Transparent Reflector

In GNSS (and especially GPS) applications, one of the key factors for having a better performance of the system is a high FBR, defined as the ratio of maximum RHCP and LHCP gain, while occurring at $\theta = 0^\circ$ and $\theta = 180^\circ$, respectively. However, in this work, since the beam of the antenna is tilted for around 30 degrees, the maximum RHCP gain occurs at around $\theta = 30^\circ$, whereas maximum LHCP gain is at $\theta = 180^\circ - 30^\circ = 150^\circ$, at the initial coordinate system. In the new coordinate system,

Chapter 4: Wideband Transparent Circularly Polarized Rectangular Slot GNSS Antenna for Vehicular Applications

however, this changes to $\theta' = 0^\circ$ and $\theta' = 180^\circ - 2 \times 30^\circ = 120^\circ$ for RHCP and LHCP maximum gains, respectively. Consequently, the terms "FBR" and "maximum RHCP and LHCP ratio" may be used interchangeably throughout the chapter.

One of the common techniques for improving the FBR is to place a reflector below the antenna in a certain distance depended on the frequency of operation. Another important parameter is the size of the reflector which can determine the amount of FBR. The trade-off between the size of the reflector and FBR has always been a challenge. In this work, the target is to establish a balance between the size of the reflector and the FBR. Furthermore, since the proposed antenna is going to be mounted on the windshield, the reflector can be placed on the dashboard or glove compartment of the vehicle, fulfilling the required distance between the antenna and reflector. This will necessitate the need of the transparent reflector, instead of an opaque one.

Taking all above-mentioned information into consideration, a transparent small-size reflector with the dimensions of 100×100 mm is designed with the usage of mesh grid in order to increase the transparency. The designed reflector is shown in Fig. 4.13 (a), and one mesh element is depicted in Fig. 4.13 (b). As discussed before, the transparency of reflector depends on the width of each trace (" n ") and length of the mesh element (" m "). Here, by setting $m=5.4$ and $n=0.1$ mm, the calculated transparency using equation (1) is about 95%. Afterwards, the reflector is put under the antenna with a distance of 85 mm from the center (or 48 mm from the lower edge) of the antenna. The isometric and side view of the final placements are illustrated in

Fig. 4.13 (c) and (d), respectively. All simulation and measurement results are discussed in more details in the next section.

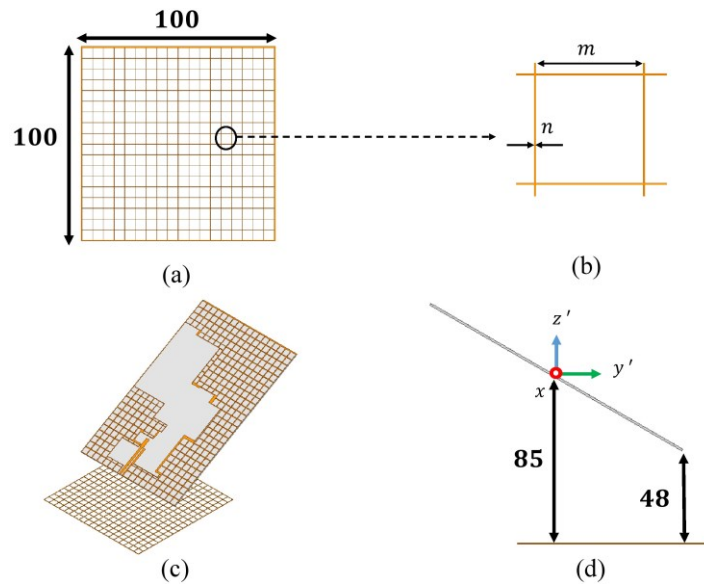


Figure 4.13: Transparent reflector and the way it is placed under the proposed antenna, (a) transparent reflector using mesh grid (b) one mesh element (c) isometric view of the reflector under the antenna (d) side view of the reflector and antenna (units in mm).

4.4 Fabrication of Prototypes and Discussion of Simulation and Measurement Results

4.4.1 Fabrication Process

The process of fabrication is done in two major steps. In the first step, the antenna is fabricated by printing conductive silver ink on two equal-size Corning® Boro-Aluminosilicate glasses with $\epsilon_r=5.5$ and thickness of 1 mm, with a precision of 0.1 mm for mesh traces. Afterwards, the two halves are connected and integrated with

Chapter 4: Wideband Transparent Circularly Polarized Rectangular Slot GNSS Antenna for Vehicular Applications

each other, forming the final prototype. For resemblance of windshield and its inclination angle, an inclined stage with an angle of 30° is fabricated using 3D printing. The material of stage is chosen to be very close to air, not to have a significant impact on the measurement results. Also, the stage is designed in such a way to be capable of holding the reflector with the desired distance under the antenna. The measurements are carried out in anechoic chamber for two states are with and without the reflector. Finally, the reflection coefficient of the antenna while placed on the windshield of a vehicle is obtained. Fig. 4.14 illustrates all the above-mentioned steps.

4.4.2 Results and Discussion

The simulation and measurement results of the proposed antenna in terms of reflection coefficient and axial ratio are depicted in Fig. 4.15 (a) and (b), respectively. As it is shown, the reflection coefficient is measured in two different states of normal (when it is measured in the lab) and on the windshield of a vehicle. The results show a very close agreement between the three plots, having a wide 10-dB impedance bandwidth of 40.8 % (1.13 - 1.71 GHz). The axial ratio simulation and measurement results are also plotted in Fig. 4.15 (b), showing a 3-dB axial ratio bandwidth of 52% (1.04 - 1.77 GHz) in the simulation and 47.4% (1.06 - 1.72 GHz) in the measurements. Both the impedance and axial ratio bandwidths cover the whole GNSS bands, starting from 1.16 GHz to 1.61 GHz. Noteworthy, the axial ratio measurement is done in the new coordinate system.

Chapter 4: Wideband Transparent Circularly Polarized Rectangular Slot GNSS Antenna for Vehicular Applications

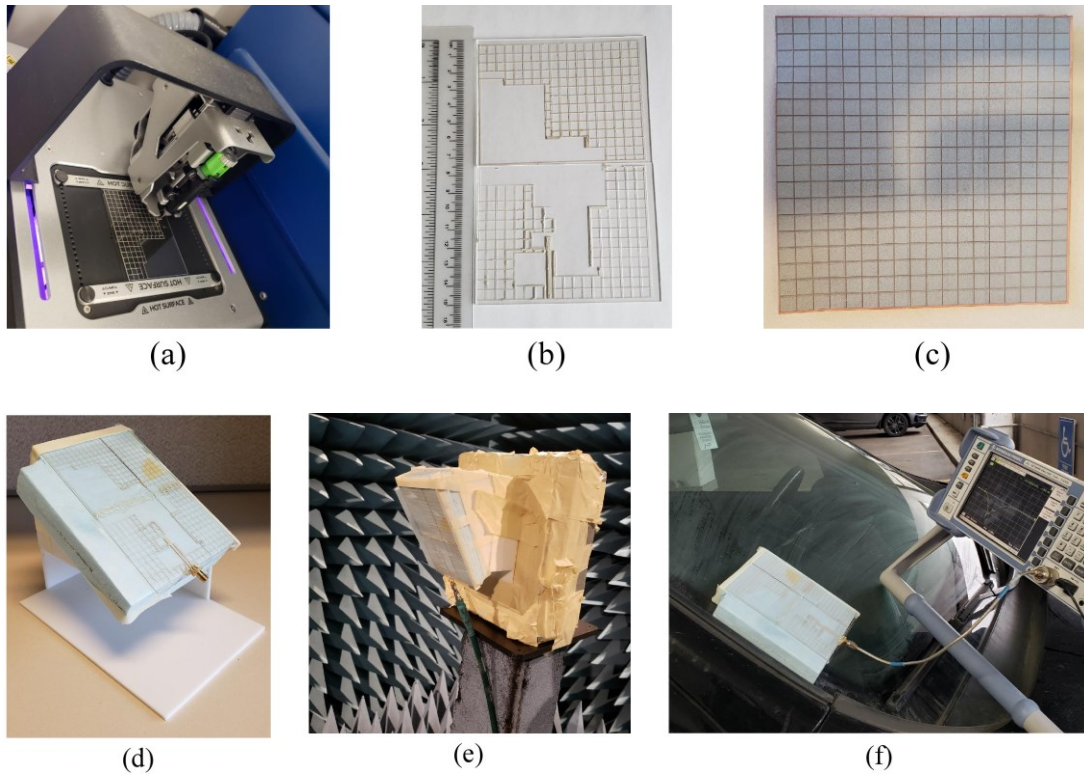


Figure 4.14: Fabrication and measurement of the proposed antenna, (a) fabrication process (b) proposed antenna before integration (c) fabricated transparent reflector (d) fabricated antenna on the inclined stage (e) measurement of the fabricated antenna in anechoic chamber (f) measurement of reflection coefficient of the proposed antenna on the windshield of vehicle.

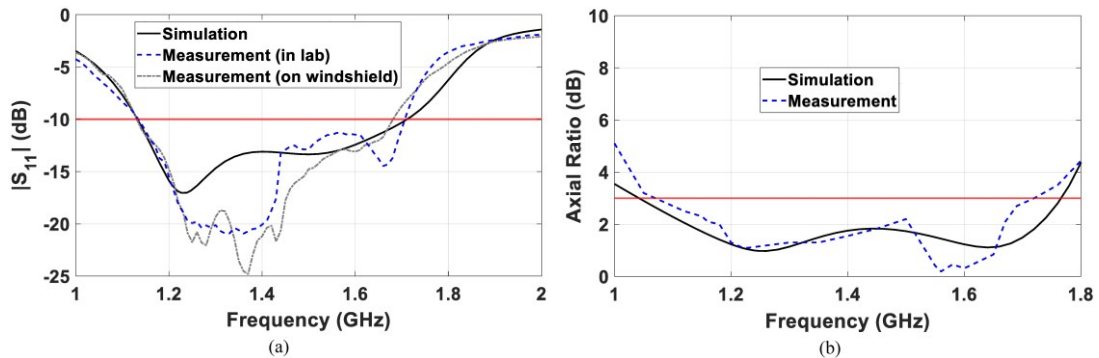


Figure 4.15: Simulation and measurement results of the proposed antenna, (a) reflection coefficient (b) axial ratio at $\theta' = 0^\circ$ and $\phi = 0^\circ$ (while mounted on the inclined stage).

Chapter 4: Wideband Transparent Circularly Polarized Rectangular Slot GNSS Antenna for Vehicular Applications

The normalized radiation patterns of the antenna while it is mounted on the inclined stage are demonstrated in Fig. 4.16 and 4.17, with and without the presence of the reflector, respectively. The patterns in Fig. 4.20 are plotted at GPS L2 and L1 center frequencies at $\phi = 0^\circ$ and $\phi = 90^\circ$ planes, in the new coordinate system. The maximum RHCP gain occurs at $\theta' = 0^\circ$, with an RHCP gain of 4.87 dBic and 5 dBic at GPS L2 and L1 bands, respectively. Also, the RHCP maximum gain while the reflector is put below the antenna is about 6.75 dBic at GPS L2, and 7.1 dBic at GPS L1 center frequencies, respectively. The measured HPBW is more than 60° . Moreover, Fig. 4.17 shows the radiation patterns of antenna with the reflector placed on the stage. Both the simulation and measurement results show an improvement of FBR for at least 5 dB, which is desirable since the reflector size is small compared to the size of the antenna. Furthermore, RHCP gain results at $\theta' = 0^\circ$ and $\phi = 0^\circ$ against frequency with and without the reflector are depicted in Fig. 4.22. The measured maximum RHCP gain is about 7.1 dBic occurring at 1.35 GHz and 5.3 dBic at 1.5 GHz for the scenarios of with and without reflector, having a 3-dB gain bandwidth of 56.3 % (1.02 - 1.82 GHz) and 54.2 % (1.02 - 1.78 GHz), respectively. The results show that the reflector not only increases the FBR, but also improves the RHCP gain.

Chapter 4: Wideband Transparent Circularly Polarized Rectangular Slot GNSS Antenna for Vehicular Applications

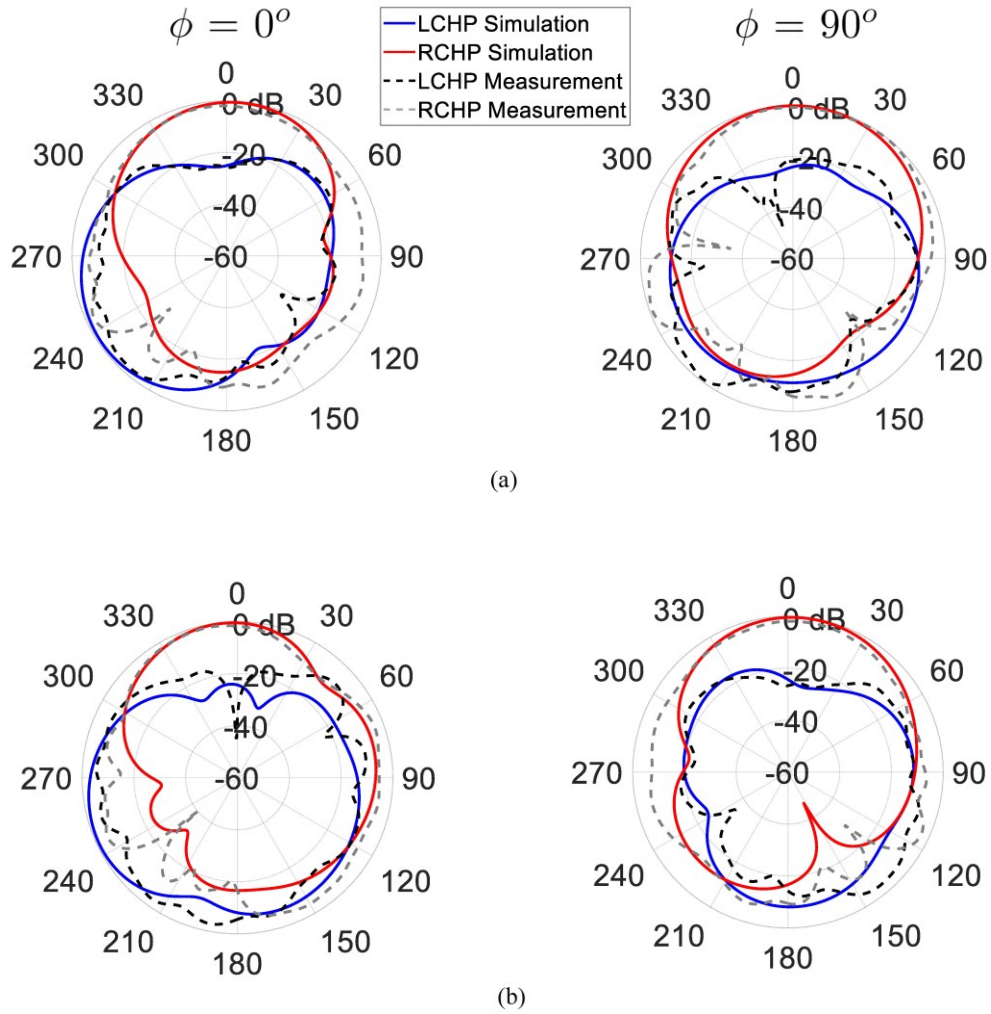


Figure 4.16: Normalized radiation pattern of the proposed antenna while placed on the inclined stage in the new coordinate system at two different frequencies, (a) 1.227 GHz (b) 1.575 GHz.

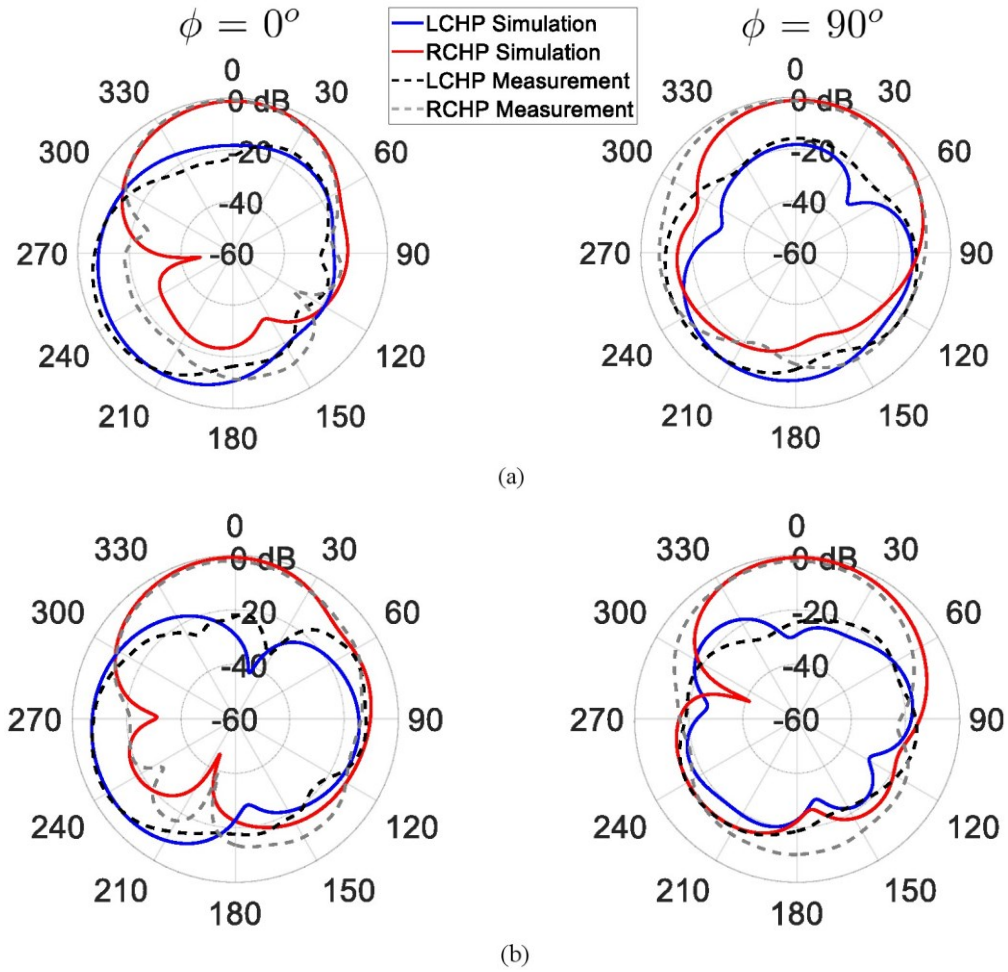


Figure 4.17: Normalized radiation pattern of the proposed antenna while placed on the inclined stage with the reflector below the antenna, in the new coordinate system at two different frequencies, (a) 1.227 GHz (b) 1.575 GHz.

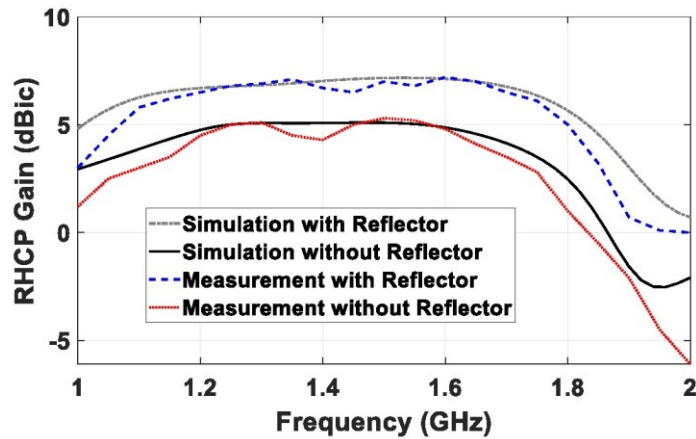


Figure 4.18: Simulation and measurement results of RHCP gain of the proposed antenna with and without the reflector at $\theta' = 0^\circ$ and $\phi = 0^\circ$.

4.4.3 Comparison with Previous Works in Literature

Table 4-1 shows the comparison of the proposed antenna with other similar previous works in literature. As can be seen, there are no other previous works having all the characteristics of being wideband, CP, tilted beam, and transparent at the same time. As discussed earlier, designing an antenna on a single-layer having all the characteristics together and adding a transparent reflector under the antenna on the dashboard or glove compartment of the car, is the main novelty of this work.

4.4.4 Results on a Car Model

To see the effects of different parts of the vehicle (such as the roof, hood, doors and so forth) on the radiation patterns, the proposed antenna with the reflector are put on the glove compartment of a car model, shown in Fig. 4.19. The results are represented in Fig. 4.20 for GPS L2 and L1 center frequencies at two different planes. Like the previous results, the new coordinate system is chosen and, consequently, the maximum RHCP gain is expected to happen at $\theta' = 0^\circ$, with an acceptable FBR. The results in Fig. 4.20 verify the acceptable performance of the antenna while it is mounted on the windshield.

Table 4-1: Comparison between some single, dual, and wideband antennas in literature and the proposed antenna

Design	Size (λ_0^2)¹	Type²	IBW (L,U)³(%)	ARBW (L,U)³ (%)	Tilted angle (deg)	Transparency (%)
[8]	0.41×0.41	DB	3.7 , 1.2	0.9 , 0.6	NT*	NT*
[30]	0.4×0.4	SB	10	Not CP	NT	80
[56]	0.57×0.57	DB	16.9 , 11.4	19.2 , 18	NT	NT
[57]	0.41×0.41	WB	42	2.1 , 2	NT	NT
[59]	0.53×0.53	WB	40.57	6.56 , 7.74	NT	NT
[64]	0.28×0.28	SB	3.2	1.7	NT	NT
[65]	4.52	WB	35	Not CP	NT	100
[66]	0.71×0.25	WB	28.5	Not CP	15	94
[67]	0.74×0.74	SB	4	10.7	49	NA
[68]	0.26×0.19	WB	20	25	NT	NT
[69]	0.988×0.52	WB	40	6.19	30	NT
[70]	0.48×0.175	WB	26**	Not CP	NT	>70
This Work	0.56×0.37	WB	40.8	47.4	30	95

¹ λ_0 is the free space wavelength at the lowest operating frequency

² “SB”: Single-Band, “DB”: Dual-Band, “WB”: Wideband

³ Lower band, Upper band

* “NT”: Not Tilted, Not Transparent

** The 10-dB IBW is obtained from the figures in the paper.

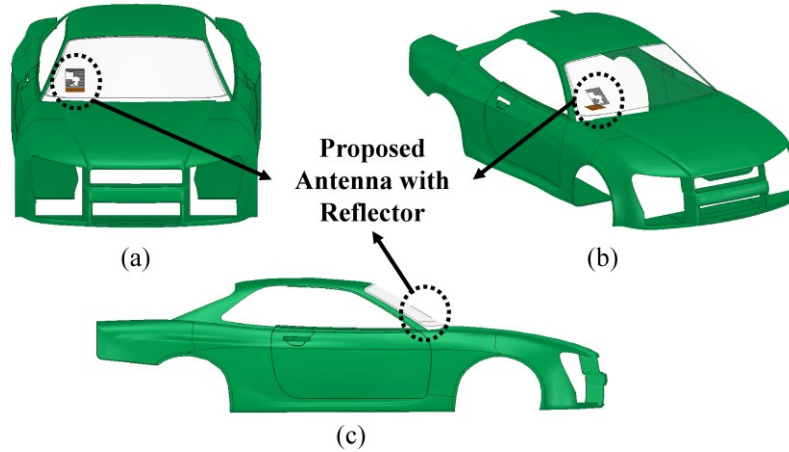


Figure 4.19: Proposed antenna with the reflector on a car model for re-simulation, (a) front view (b) isometric view (c) side view.

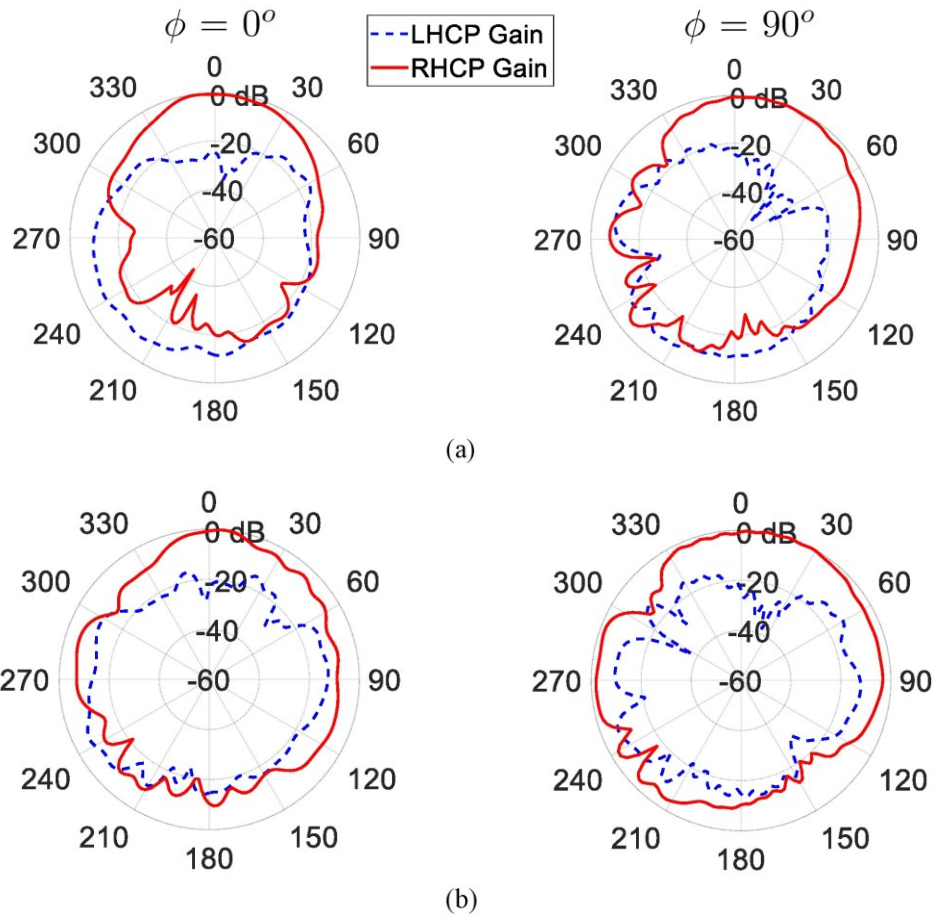


Figure 4.20: Simulated normalized radiation pattern of the proposed antenna on the car model at two different frequencies with the reflector under the antenna, (a) 1.227 GHz (b) 1.575 GHz.

4.4.5 Effects of Mesh Defects on the Performance of the Antenna

In some cases and situations (especially during the fabrication), some defects might occur in the mesh grid layer of the proposed antenna. In this section, the effects of having defects in the mesh grid is investigated. Fig. 4.21 illustrates two different states of the proposed antenna with defects in mesh grid layer. Fig. 4.21 (a) shows the state 1 in which a defect exists in the mesh layer, while Fig. 4.21 (b) shows the state 2 where defects exist in two different areas. Defects are demonstrated using red dash lines.

The simulation results of the proposed antenna and two different states (state 1 and 2) are depicted in Fig. 4.22. As can be seen, the performance of the antenna in terms of reflection coefficient, axial ratio, and RHCP gain remains constant and the antenna still works properly at the existence of minor defects in the mesh layer.

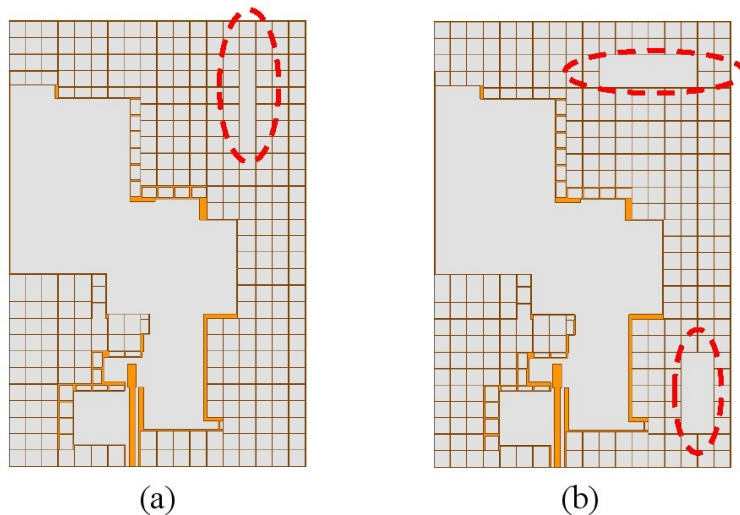


Figure 4.21: Two different states showing different types of defects on the mesh grid shown in red dash lines, (a) state 1 (b) state 2.

Chapter 4: Wideband Transparent Circularly Polarized Rectangular Slot GNSS Antenna for Vehicular Applications

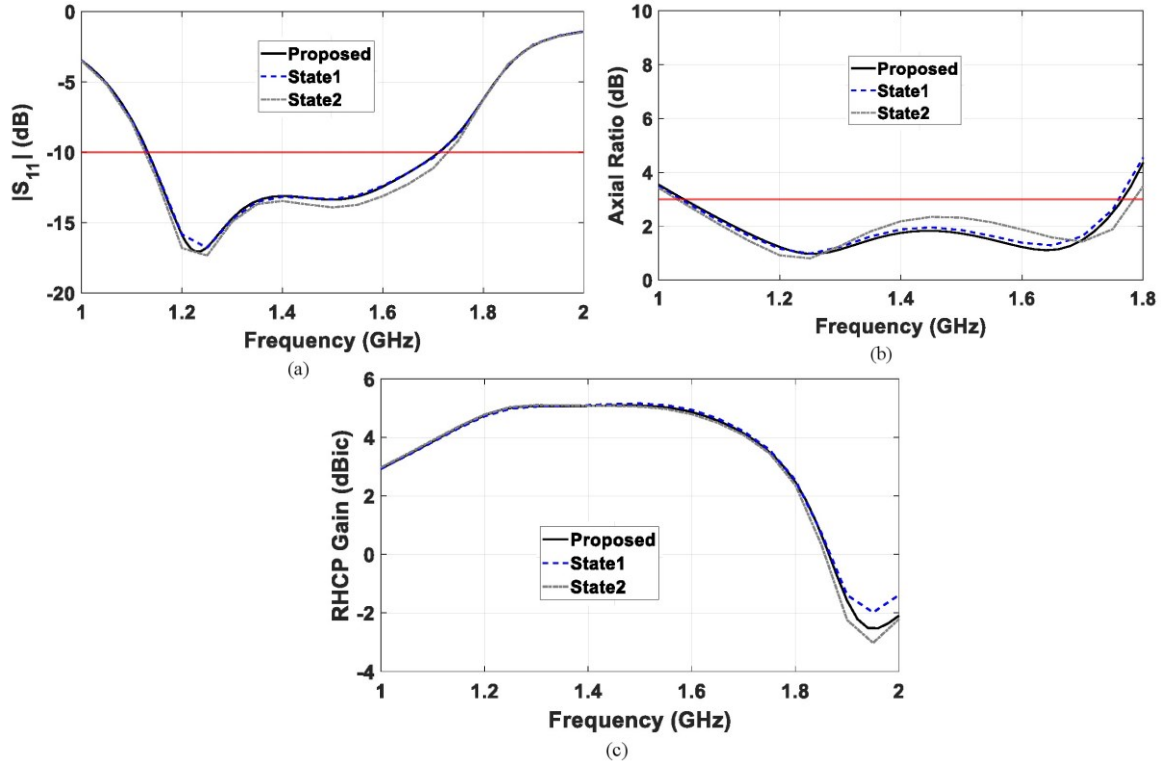


Figure 4.22: Simulation results of the proposed antenna and two states in which defects exist in the mesh layer, (a) reflection coefficient (b) axial ratio (c) RHCP gain at $\theta' = 0^\circ$.

The reason lies behind the fact that since there are many mesh elements in the conductive layer, the surface current of the proposed antenna is formed and distributed throughout the surface using all mesh elements, and a change (defect here) in the formation of several mesh elements does not significantly change the performance of the antenna. However, it should be noted that large changes in the mesh grid layers may impact the performance of the antenna.

4.5 Conclusion

In this chapter, a novel single-layer wideband CPW-fed transparent CP antenna with tilted beam is proposed. The antenna has a wideband 10-dB impedance bandwidth of 40.8 % (1.13 - 1.71 GHz) and a wideband 3-dB axial ratio bandwidth of 47.4 % (1.06 - 1.72 GHz) and a 3-dB gain bandwidth of 54 % (1.02 - 1.78 GHz) are obtained in the measurements, covering the whole GNSS frequency bands. The RHCP gain of the antenna at $\theta' = 0^\circ$ and $\phi = 0^\circ$ is about 6.75 and 7.1 dBic at GPS L2 and L1 bands respectively, in the presence of the reflector. The antenna is fabricated on Corning® Boro-Aluminosilicate glass with $\epsilon_r=5.5$ and thickness of 1 mm. Mesh grid is used for the conductive layer of the antenna, instead of a full layer. The transparency of the antenna is about 95 %. The operation of antenna is investigated with CMA with a step-by-step procedure shown in the appendix. Furthermore, to increase the FBR and RHCP gain of the antenna, a small-size transparent reflector is designed and placed under the antenna with a certain distance. The radiation patterns show a tilted beam antenna with an acceptable performance in terms of reflection coefficient, axial ratio, RHCP gain, FBR, and so on. In the final step, the antenna is re-simulated on a car model to see the effects of different parts of a car on the radiation patterns. The proposed antenna is suitable for inclined surfaces and also for GNSS/GPS applications, such as location tracking of the vehicles. Comparing to the previous works in literature, no other such antennas being wideband, CP, transparent, and tilted beam were proposed. In the next chapter, another wideband CP transparent antenna with tilted beams is proposed which is suitable for vehicular applications.

5. Chapter 5: Wideband Transparent Circularly Polarized Spiral Slot Antenna with Tilted Beam for Automotive Applications

5.1 Introduction

In this chapter, another novel single layer microstrip circularly polarized CPW-fed transparent antenna with tilted beam has been proposed. As most of the cars' windshields are inclined around 30° , the antenna is designed to have a tilted beam for around 30° . In this case, the maximum RHCP antenna gain will occur at $\theta=0^\circ$. The axial ratio is calculated while the antenna is mounted on an inclined stage. To make the antenna transparent, a Corning® Boro-Aluminosilicate glass with $\epsilon_r=5.5$ and a thickness of 1mm is used as the substrate. Moreover, silver mesh grid is used instead of full conductive layer to increase the transparency of the antenna. Additionally, in order to increase the RHCP gain and decrease the LHCP gain of the antenna, a transparent reflector (same as the transparent reflector proposed in the previous chapter) is used with a certain distance below the antenna. The reflector can be placed on the dashboard or the glove compartment of the vehicle, having a certain distance from the antenna. To have a better understanding of how the antenna works, characteristic mode analysis is performed for the conductive layer, which provides the physical understanding of the operation mechanism, presented in the appendix.

The rest of the chapter is organized as follows. Section 5.2 introduces the antenna configuration and development stages. Section 5.3 discusses the antenna development

analysis and CP mechanism. In Section 5.4, fabrication and measurements will be shown, and finally, the conclusion is presented in Section 5.5.

5.2 Antenna Configuration and Development

5.2.1 Antenna Geometry

The geometry of the proposed antenna is shown in Fig. 5.1. As stated earlier, spiral antennas are known for their capability of producing circular polarization. Also, they are capable to make the beam of the antenna tilted at some desired frequencies. The proposed CPW-fed spiral-based slot antenna details are depicted in Fig. 5.1 as well. The substrate of the antenna is a Corning® Boro-Aluminosilicate glass with the permittivity of $\epsilon_r=5.5$ and a thickness of 1 mm. The input of the antenna is fed by a 50 Ω coaxial feedline. In order to make the antenna transparent, mesh grid is used instead of full conductive layer.

The mesh grid which makes the antenna transparent consists of different slot dimensions. The majority of the slots are squares with a length of 6.9 mm and a width of 0.1 mm (see Fig. 5.1 (c)). The size of the mesh grid is not the same in the whole design as some parts need smaller slots and some others need larger ones. By making the width of grid thinner, the transparency of the antenna increases. However, it makes the fabrication of the antenna harder. The development of the proposed antenna and the CP mechanism are discussed in the following sections.

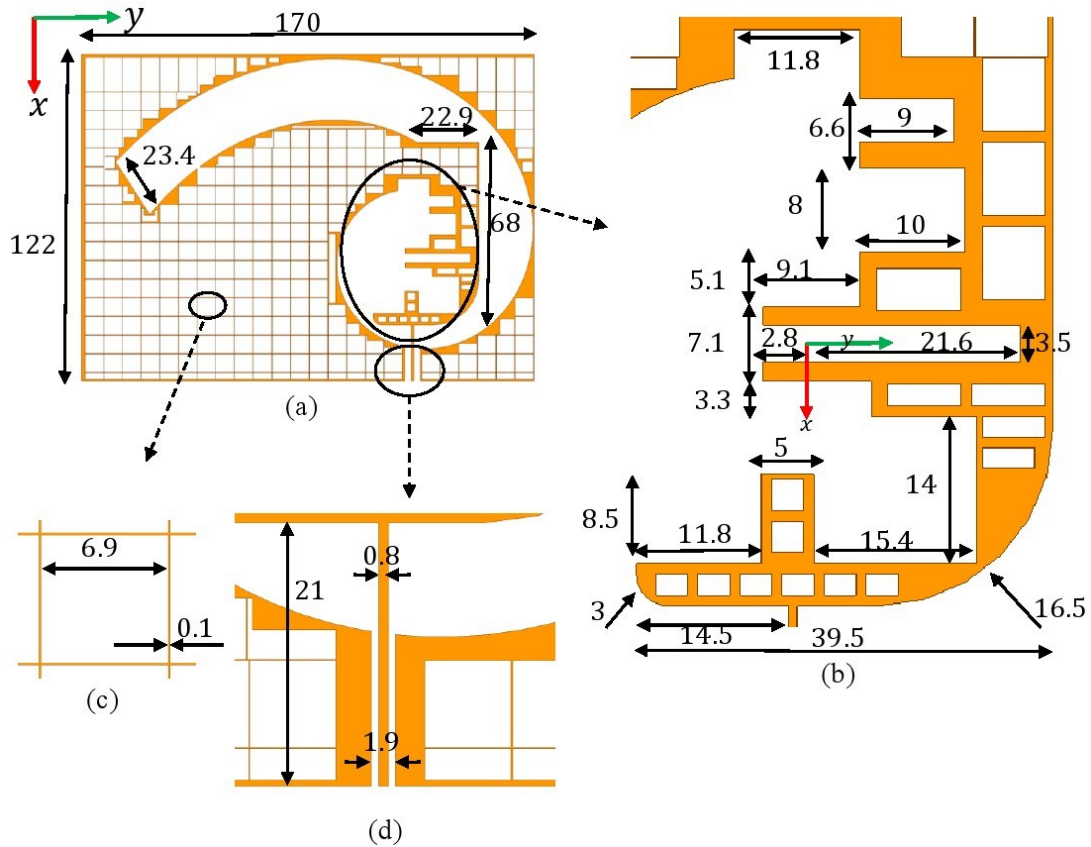


Figure 5.1: The configuration of the proposed antenna and its different parts, (a) final design, (b) enlarged view of the middle section (c) one mesh element (d) enlarged view of the feedline (all dimensions in mm).

5.2.2 Antenna Development Stages

The initial configuration of the antenna is a spiral slot with the following equation:

$$r = r_0 \exp(at) \quad (2)$$

where “ r ” is the radial distance of the spiral arms from the origin, “ a ” is the spiral growth rate, “ t ” is the angular position, and r_0 is the radial distance when $t=0$. To have a better visualization, the first two steps for realizing the proposed antenna are shown in Fig. 5.2. The initial spiral arms are depicted in two different colors. The red arm (curve1) which has the same equation as (2), starts from “ $Start1$ ” and ends at “ $End1$ ”

points. The blue arm (curve2) also starts from “Start2” and ends at “End2” points and has the following equation:

$$r = r_0 \exp(at) + d \quad (3)$$

where the parameters are the same as (2), with a distance of “d” between the arms. After implementing the spiral arms with a growth rate of “a=0.57”, the spiral slot is rotated for 163° counter-clockwise. In Fig. 5.2 (b), the rotated spiral slot is shown while it has been subtracted from the conductive layer.

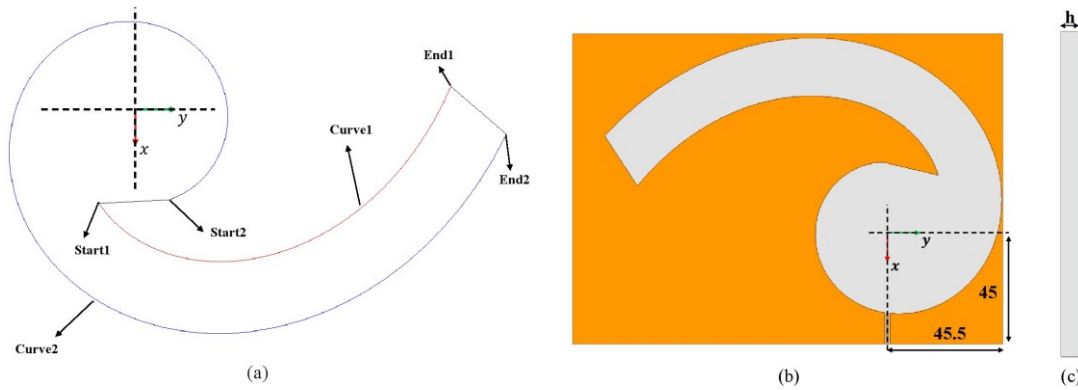


Figure 5.2: Two initial steps for realizing the proposed antenna, (a) spiral arms of the slot spiral (b) the spiral slot on the conductive layer after the rotation (c) side view of the antenna. $h = 1$, $r_0 = 15.6$, $d = 25.3$ (units are in mm), and Start1= 1.1, Start2= -4.3, End1=3.2, End2= 3.1 (units are in rad).

The antenna development stages are depicted in Fig. 5.3. Shown in Fig. 5.3 (a), Ant 1 has the same structure as introduced in Fig. 5.2 (b), added with a radiator to be matched to a 50 Ω feedline. The antenna, however, is not matched to the input, but is circularly polarized in L2 band. To match the antenna perfectly, in the next step, an L-shaped radiator is introduced and integrated into the spiral slot, resulting in Ant 2. Here, the antenna radiates from 0.94 to 1.46 GHz with a tilted beam of 30 degrees in the entire band. Then, several rectangular slots have been added to the L-shaped part,

Chapter 5: Wideband Transparent Circularly Polarized Spiral Slot Antenna with Tilted Beam for Automotive Applications

creating Ant3. These slots make the antenna circularly polarized at the tilted angle (at $\theta = 30^\circ$) and also produce a 55.3 % 10-dB impedance bandwidth (1.02 - 1.80 GHz). Finally, mesh grid is applied to the design to make it transparent, shown in Fig. 5.3 (d) (proposed antenna). The dimensions of the middle section of the proposed antenna ("B") were shown in Fig. 5.1(b). As the goal of the final antenna is to be circularly polarized at the tilted beam ($\theta = 30^\circ$), a new coordinate system is introduced which has been rotated for 30 degrees. In other words, the maximum gain of the antenna is desired to occur at $\theta' = 0^\circ$ in the new coordinate system.

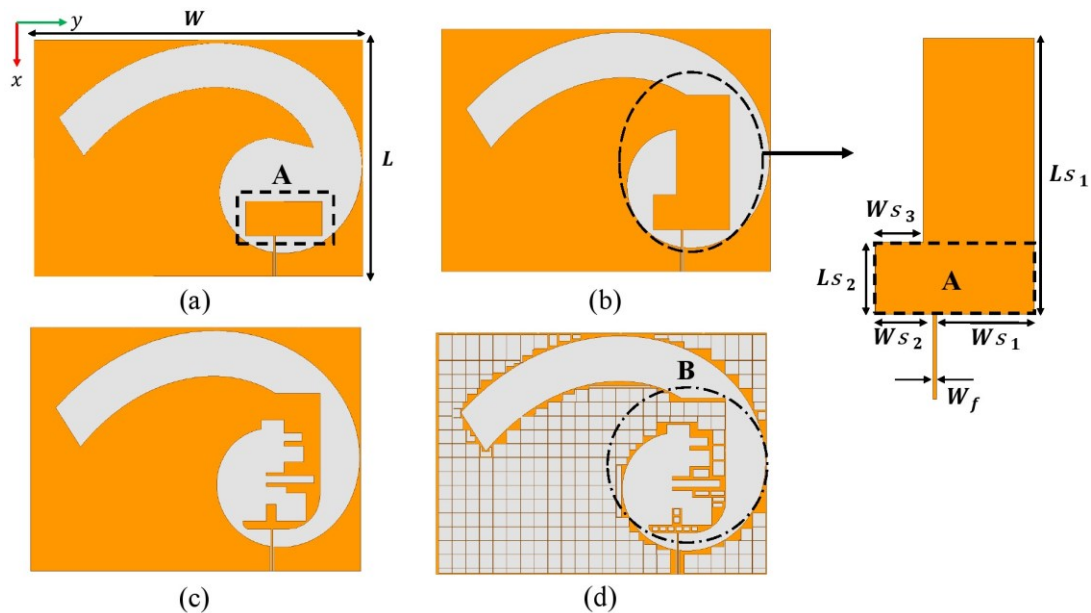


Figure 5.3: Evolution steps of the proposed antenna and the enlarged L-shaped radiator, (a) Ant1 (b) Ant2 (c) Ant3 (d) proposed antenna. $W = 170$, $L = 122$, $L_{S1} = 68$, $L_{S2} = 17.6$, $W_{S1} = 24.2$, $W_{S2} = 14.5$, $W_{S3} = 12$, $W_f = 0.8$ (units are in mm).

In Fig. 5.4, the proposed antenna is shown while placed on the windshield in a new coordinate system. It is worth mentioning that the results (the axial ratio and radiation patterns) have been obtained in the new coordinate system (more details are presented in Section 5.4). The reflection coefficient and the axial ratio of Ants 1-3 and the

Chapter 5: Wideband Transparent Circularly Polarized Spiral Slot Antenna with Tilted Beam for Automotive Applications

proposed antenna are shown in Fig. 5.5. The results show that by making the antenna transparent using mesh grid, the reflection coefficient and the axial ratio just have a slight change in their values and also an ignorable shift in the resonance frequencies. More details about the antenna development stages are presented in Section 5.3. It is worth mentioning that the characteristic mode analysis (CMA) for the proposed antenna is performed and presented in the appendix.

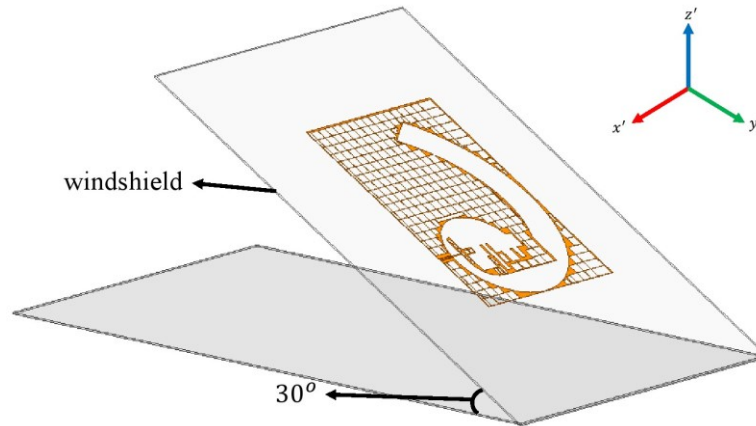


Figure 5.4: The proposed antenna while placed on the windshield introducing a new coordinate system.

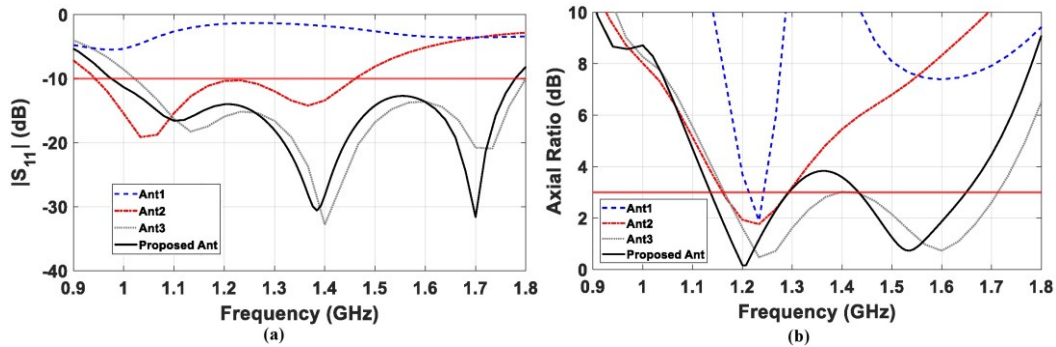


Figure 5.5: Reflection coefficient and axial ratio of Ant1-3 and the proposed antenna, (a) reflection coefficient, (b) axial ratio.

5.3 Antenna Development Analysis and CP mechanism

The antenna development analysis is performed in this section. For making circular polarization, two orthogonal components of E_x and E_y must be equal in magnitude and have a 90 degrees phase difference in the frequency bands of interest. Fig. 5.6 illustrates the magnitude ratio and phase difference of orthogonal field components of E_x and E_y in the new coordinate system. As can be seen, for Ant 1 the field components have an equal magnitude and a phase difference of about 90° at L2 band. For Ant 2, after adding the L-shaped radiator, the phase difference between the field components become more stable in the frequency band. However, the magnitude ratio decreases and become less than 1, as the frequency increases. To solve this problem, the effective electrical length should be altered in order to increase the phase difference of the orthogonal components in the frequency band. Hence, several rectangular slots are added to the L-shaped radiator, causing the magnitude ratio remain near 1 for a wider bandwidth, while making changes in the phase difference in the frequency band of interest as well (Ant 3). Finally, the magnitude ratio and the phase difference of the proposed antenna field components are depicted, showing that the changes are very slight and ignorable compared to Ant 3.

To figure out how the antenna is circularly polarized at the tilted angle ($\theta' = 0$), the surface currents of Ant3 in four different time instants at two different center frequencies of GPS L2 and L1 bands are shown in Fig. 5.7 and 5.8, respectively.

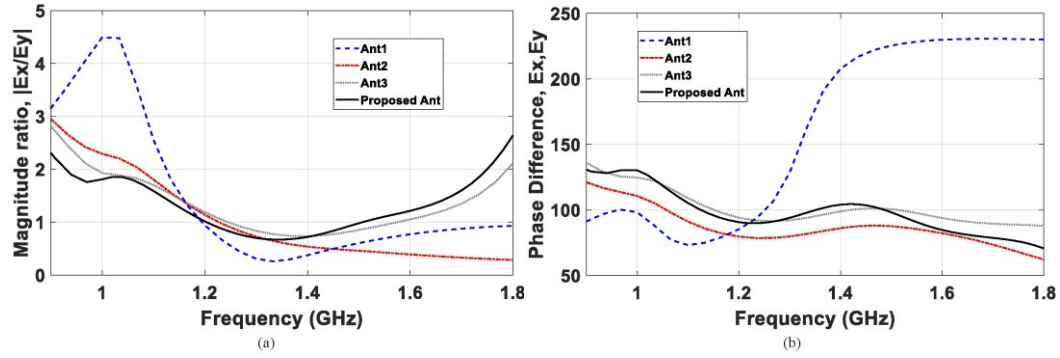


Figure 5.6: Magnitude ratio and phase difference of orthogonal field components E_x and E_y , (a) magnitude ratio (b) phase difference (the unit is in degree).

Since the proposed antenna consists of mesh grid pattern, illustration of the surface current distribution and observation of currents rotation at different time instants in Ant3 are more obvious. Also, as most characteristics and results of Ant3 are very close to the proposed antenna, the surface current distribution on Ant3 is shown in this part, instead of the proposed antenna. As can be seen, the surface currents direction is rotating counter-clockwise causing RHCP wave radiation. Also, the way that the antenna is being observed are shown in Fig. 5.7 (e) and 5.8 (e). The direction of the currents are shown with an arrow in each time instant. Taking L2 center frequency as an example, the dominated electric fields are pointing toward $(-y)'$ -direction at $t=0^\circ$ (see Fig. 5.7 (a)). At $t=90^\circ$, the dominated electric fields direction change for 90° , pointing along the x' -direction. Then, after passing a quarter of a period, the dominated electric fields orientation changes for 90° counter-clockwise. Finally, the electric fields at $t=270^\circ$ show a 90° anticlockwise rotation from the previous time instant, oriented at $(-x')$ -direction (see Fig. 5.7 (d)).

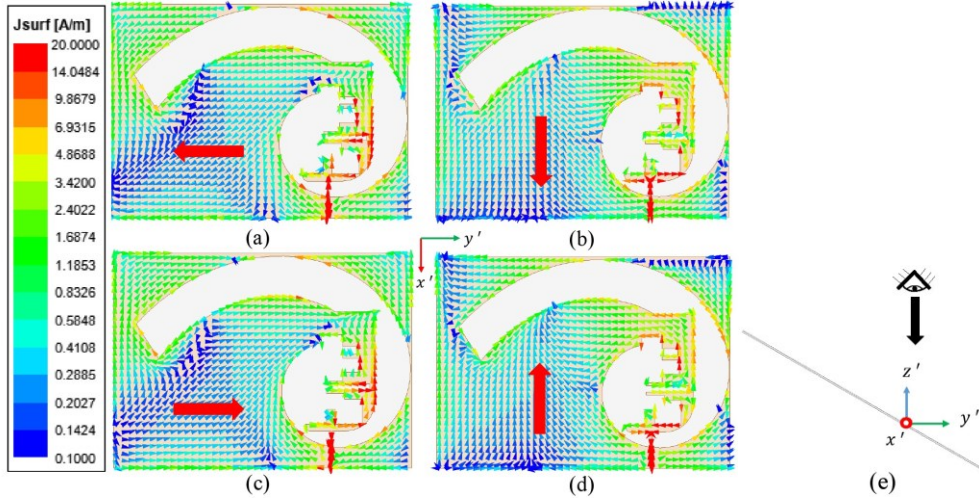


Figure 5.7: Surface currents distribution of Ant3 at four different time instants at 1.227 GHz, (a) 0° (b) 90° (c) 180° (d) 270° (e) observation of the proposed antenna for the electric fields distribution.

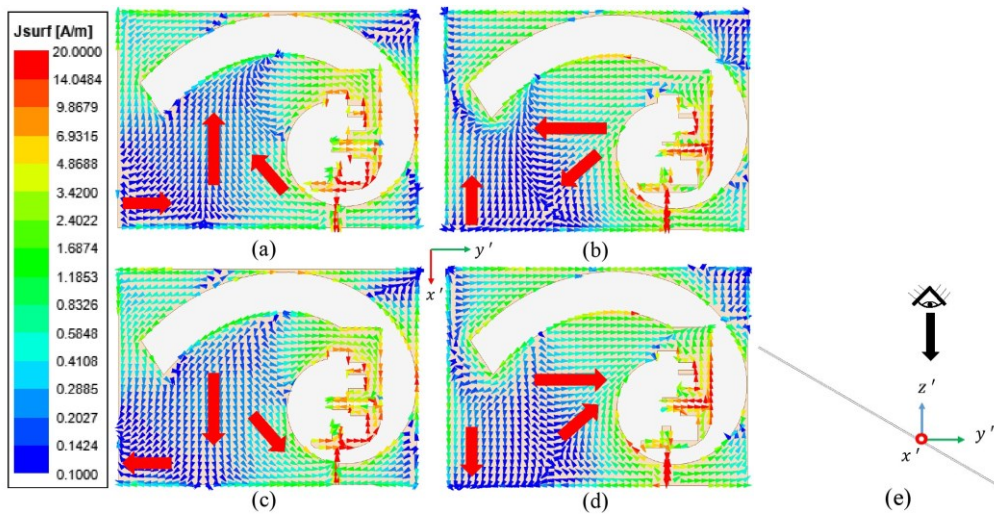


Figure 5.8: Surface currents distribution of Ant3 at four different time instants at 1.575 GHz, (a) 0° (b) 90° (c) 180° (d) 270° (e) observation of the proposed antenna for the electric fields distribution.

5.3.1 Transparent Reflector

The radiations of slot antennas are mostly bi-directional. To make it suitable for satellite applications, usually a metallic reflector or a cavity is used in order to make

Chapter 5: Wideband Transparent Circularly Polarized Spiral Slot Antenna with Tilted Beam for Automotive Applications

the antenna unidirectional, causing the FBR to improve. Hence, a small-size reflector with the size of $100 \text{ mm} \times 100 \text{ mm}$ ($0.32\lambda \times 0.32\lambda$) is used under the antenna. By increasing the size of the reflector, it is expected to have a higher FBR. Since the reflector should be placed in the vehicle (on the dashboard or the glove compartment), it is better to be transparent like the proposed antenna. Therefore, the same mesh grid is applied for the reflector, each element having a width of 0.1 mm and a length of 5.4 mm which cause a transparency of about 95 %. The reflector with full conductive layer, transparent reflector, and one mesh element are demonstrated in Fig. 5.9. Since the beam of the antenna is tilted, instead of using FBR, the ratio of maximum RHCP and LHCP gains are measured. For this specific application, a ratio of 5 dB would be suitable. By using the antenna theory, in order to have a high FBR (unidirectional radiation), the distance between the reflector and the antenna should be quarter-wavelength. The free space quarter-wavelength value for L2 and L1 bands are 61 mm and 47 mm, respectively. The arrangement of the reflector and the proposed antenna from different views is depicted in Fig. 5.10. Here, the reflector has been placed 45 mm below the antenna, around a quarter-wavelength at L1 band (see Fig. 5.10 (b)).

5.3.2 Parametric Study

The effects of different parameters of the antenna on the reflection coefficient and the axial ratio have been investigated through the simulations. Two main parameters which have the most significant impacts on the behaviour of the antenna, “ a ”, and “ $End1\&2$ ”, are chosen for investigation. Fig. 5.11 shows the different variations of the end of the spiral arm through the changes in “ $End1\&2$ ”.

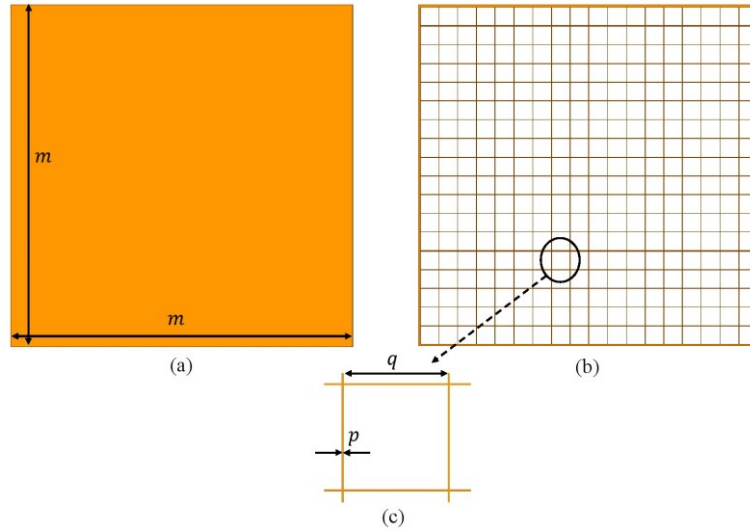


Figure 5.9: The proposed reflector, (a) full reflector (b) transparent reflector (c) width and length of mesh elements used in transparent reflector. $m=100$, $p=0.1$, $q=5.4$ (all dimensions in mm)

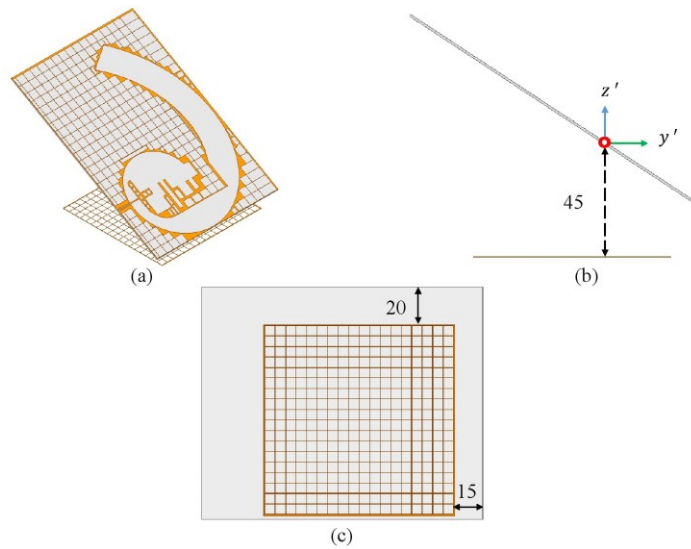


Figure 5.10: Arrangement of the reflector and the proposed antenna, (a) isometric view (b) front view (c) bottom view (all dimensions in mm).

By increasing the length of the spiral arm, the reflection coefficient shifts to lower frequencies, while maintaining the upper frequency stable. This shows that the length of the spiral arm determines the working frequency. In this case, the lower frequencies are much affected by the length of the spiral arm. It is worth mentioning that the

numbers written for the “ $End1\&2$ ” values are in radian. Moreover, Fig. 5.11 (b) shows the variations in the axial ratio of which the antenna becomes CP by lengthening the spiral arms. In Fig. 5.12, the spiral growth rate “ a ” has been investigated. The lower growth rates contribute to a smaller slot, both in length and curvature. Like the previous parameters, the lower frequencies shift to the left as the growth rate increases, while the upper working frequencies do not change a lot. Also, by increasing the spiral growth rate, the axial ratio at L2 and L1 bands decreases.

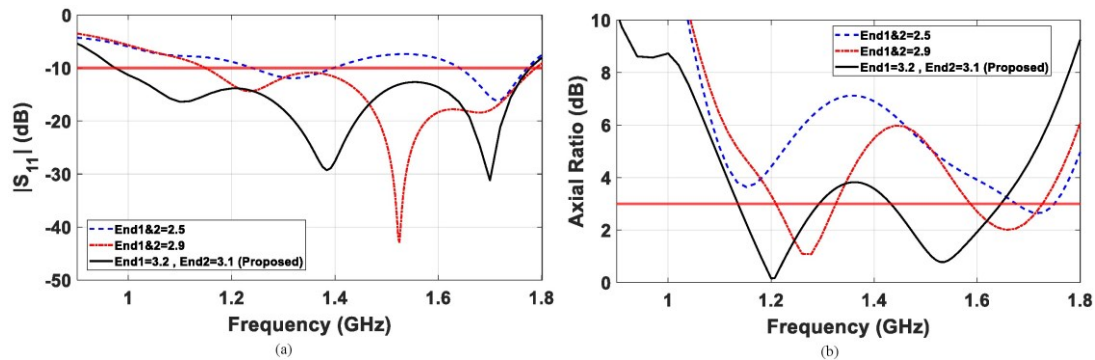


Figure 5.11: Simulated results of the proposed antenna with different values of $End1\&2$, (a) reflection coefficient (b) axial ratio.

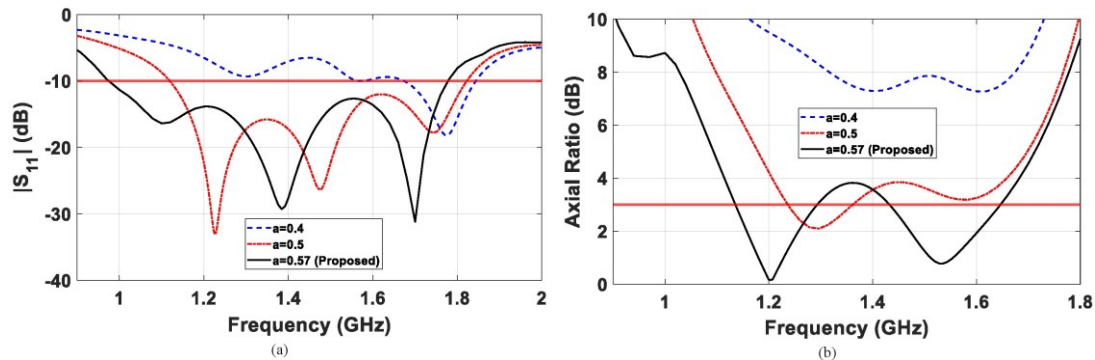


Figure 5.12: Simulated results of the proposed antenna with different values of “ a ”, (a) reflection coefficient (b) axial ratio.

5.3.3 Mesh Grid and Optical Transparency

By using mesh grid instead of full metal conductor, the transparency will increase. The optical transparency definition is the ratio of the whole and open area. Having a periodic pattern of mesh elements, similar to Fig. 5.9 (b) and (c), the optical transparency is defined as follows:

$$OT = \left(\frac{q}{q+p}\right)^2 \quad (4)$$

where “ q ” is the length and “ p ” is the width of mesh element. However, for a surface in which the pattern of mesh elements is not periodic, the optical transparency percentage can be obtained by calculating the whole and open areas and obtaining the ratio.

5.4 Fabrication and Measurements

In this section, the details of prototype manufacturing process and experimental measurements under two different situations and placements of the proposed antenna (with and without the reflector) are discussed.

5.4.1 Prototype and Manufacturing Process

The proposed antenna manufacturing process is based on printing. Corning® Boro-Aluminosilicate glass with $\epsilon_r=5.5$ and thickness of 1 mm is used as the substrate of the antenna. The conductive layer is printed on the substrate using silver conductive

ink and heated up to a high temperature to cure and stabilize the ink on the glass. The fabrication process and the proposed antenna are demonstrated in Fig. 5.13 (a) and (b), respectively. It is worth mentioning that the antenna is fabricated in two halves and connected together after the fabrication. To hold the antenna on an inclined surface, an inclined stage is fabricated using 3D printing manufacturing. The dielectric constant of the material used for the inclined stage is chosen to be very close to the air not to have significant impact on the parameters of the antenna. The stage is also capable to hold the transparent reflector. Fig. 5.13 (c) shows the stage and reflector. The inclination angle is 30 degrees with respect to the horizon. The measurements have been done in the anechoic chamber shown in Fig. 5.13 (d), measuring the parameters of the antenna while it is placed on the inclined stage. In this case, the maximum RHCP gain of the antenna is expected to occur nearly at $\theta' = 0$. Finally, the measurement setup and the proposed antenna when placed on the windshield is shown in Fig. 5.13 (e).

5.4.2 Study of Measurement Results

The simulation and measurement results of the proposed antenna in terms of reflection coefficient and axial ratio are depicted in Fig. 5.14. As can be seen, the simulation and measurement results of the proposed antenna are in a close agreement both in terms of reflection coefficient and axial ratio. Also, the reflection coefficient of the proposed antenna while it is on an inclined windshield is shown in Fig. 5.14 (a).

Chapter 5: Wideband Transparent Circularly Polarized Spiral Slot Antenna with Tilted Beam for Automotive Applications

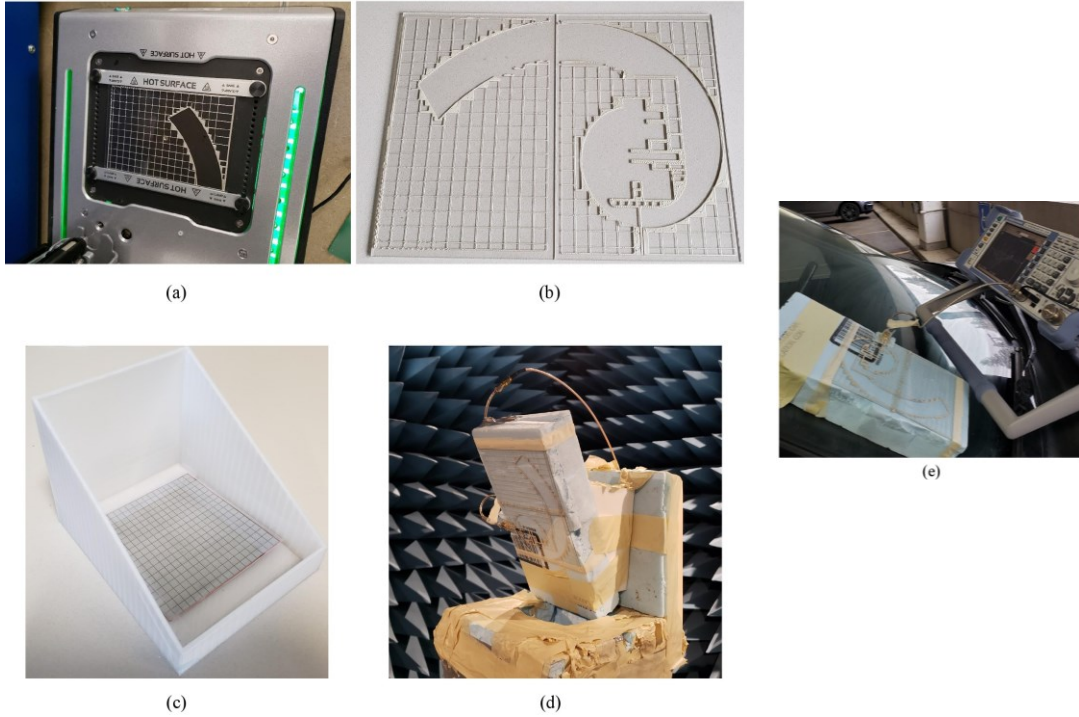


Figure 5.13: Fabricated prototype and measurements, (a) fabrication process (b) fabricated prototype before integration (c) inclined stage with fabricated reflector (d) proposed antenna measurement in anechoic chamber (e) reflection coefficient measurement of the proposed antenna while placed on the windshield.

The simulation results show the impedance bandwidth of 59 % (0.97 - 1.78 GHz), while the measurement results show impedance bandwidth of 57 % (0.98 - 1.76 GHz). The frequency shift of measured reflection coefficient of the antenna on the windshield is due to the effects of the materials in the environment, like the windshield, hood, and so forth.

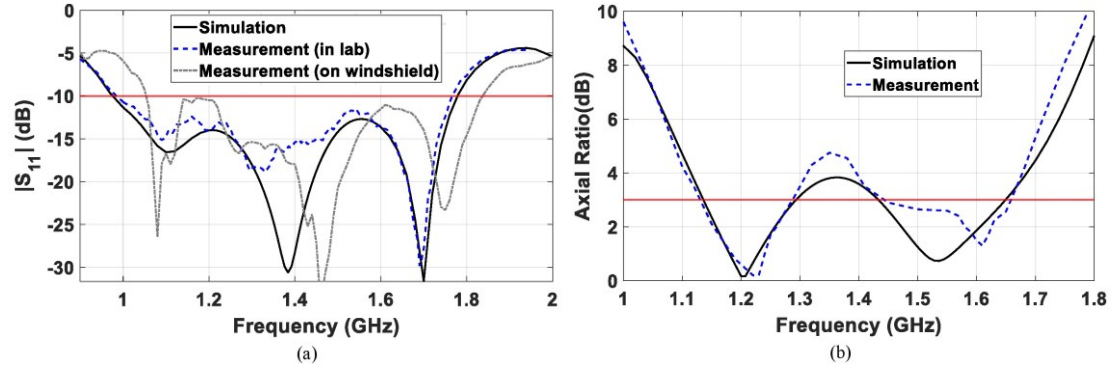


Figure 5.14: Simulation and measurement results of the proposed antenna in terms of reflection coefficient and axial ratio, (a) simulation and measurement results of the reflection coefficient in lab and on the inclined windshield (b) axial ratio, while it is mounted on the inclined stage without the reflector at $\theta' = 0$, $\phi = 0$.

Also, the 3-dB axial ratio bandwidth of 13 % (1.13 - 1.29 GHz) in lower bandwidth and 14 % (1.44 - 1.66 GHz) in upper bandwidth is obtained in measurements. It is noteworthy that the axial ratio measurement is obtained while the antenna is placed on the stage (done in the new coordinate system). Fig. 5.15 demonstrates the radiation pattern of the antenna in the new coordinate system (mounted on the stage) for GPS L2 and L1 center frequencies in two different planes of $\phi = 0^\circ$, and $\phi = 90^\circ$. The maximum RHCP gain of the antenna occurs nearly at $\theta' = 0^\circ$, while the maximum left hand circular polarization (LHCP) gain do not occur at $\theta' = 180^\circ$, as expected to be inclined for about 30 degrees in the first coordinate system and $2 \times 30 = 60$ degrees in the new one. Furthermore, the HPBW of the antenna is about 70 degrees in both $\phi = 0^\circ$, and $\phi = 90^\circ$ planes. In Fig. 5.16, the RHCP and LHCP radiation patterns of the proposed antenna mounted on the stage with the reflector below the antenna are shown at GPS L2 and L1 center frequencies in two different planes of $\phi = 0^\circ$, and $\phi = 90^\circ$. The HPBW in this new scenario still remains around 70 degrees. Comparing the results of Fig. 5.15 and Fig. 5.16, it is obvious that as the beam of the

Chapter 5: Wideband Transparent Circularly Polarized Spiral Slot Antenna with Tilted Beam for Automotive Applications

antenna is tilted, the FBR would be high (about 12 dB at L2 band and 8.5 dB at L1 band). However, the maximum RHCP and LHCP gain are almost the same (5.1 dBic at L2 band and 5.3 dBic at L1 band). By adding the reflector below the antenna, the FBR ratio turns to 7.5 dB and 20 dB in L2 and L1 bands respectively in the simulation results, while having a FBR of 18 dB and 20 dB in L2 and L1 bands respectively in the measurements. Also, the maximum RHCP gain of the antenna increases to 6.75 dBic and 7 dBic at L2 and L1 frequency band, while the maximum LHCP gain decreases to 1.8 dBic and 0 dBic at L2 and L1 frequency bands, respectively. The simulation and measurement results of RHCP gain of the antenna in the new coordinate system is represented in Fig. 5.17 for both scenarios of with and without the reflector. Additionally, the measured 3-dB axial ratio beamwidth of the antenna at 1.227 GHz is about 82° and 48° at $\phi = 0^\circ$, and $\phi = 90^\circ$ planes, respectively. Also, at 1.575 GHz, the measured 3-dB axial ratio beamwidth is about 50° and 33° at $\phi = 0^\circ$, and $\phi = 90^\circ$ planes, respectively. Noteworthy, the simulated and measured efficiencies of the proposed antenna are more than 85 % in the desired GNSS bandwidth (1.16 GHz – 1.61 GHz) which is acceptable for our desired application.

5.4.3 Results on a Car Model

The effects of different parts of a vehicle (like the windshield, hood, roof, doors, etc.) on the radiation pattern must be considered. Fig. 5.18 shows a car model on which the proposed antenna is re-simulated again to see the effects of different parts on the radiation pattern. The simulated results of the radiation patterns at two different frequencies and planes are plotted in Fig. 5.19. As can be seen, the patterns show an

Chapter 5: Wideband Transparent Circularly Polarized Spiral Slot Antenna with Tilted Beam for Automotive Applications

acceptable performance of the antenna on the windshield of the car model, having a maximum RHCP gain at nearly $\theta' = 0^\circ$, with almost 7 dB and 8 dB difference between the maximum RHCP and LHCP gains, making the antenna a good candidate for being used in automotive applications.

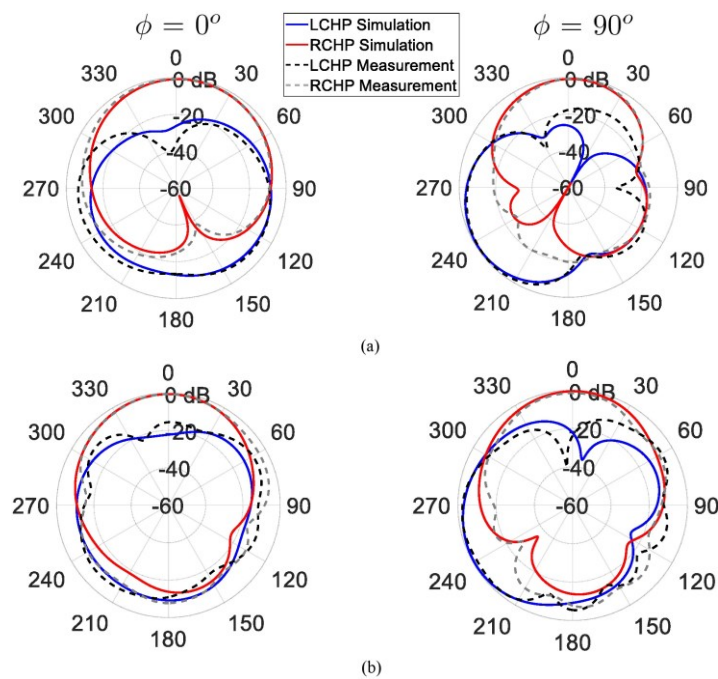


Figure 5.15: Normalized radiation pattern of the proposed antenna while mounted on the inclined stage without the reflector at (a) 1.227 GHz, (b) 1.575 GHz.

Chapter 5: Wideband Transparent Circularly Polarized Spiral Slot Antenna with Tilted Beam for Automotive Applications

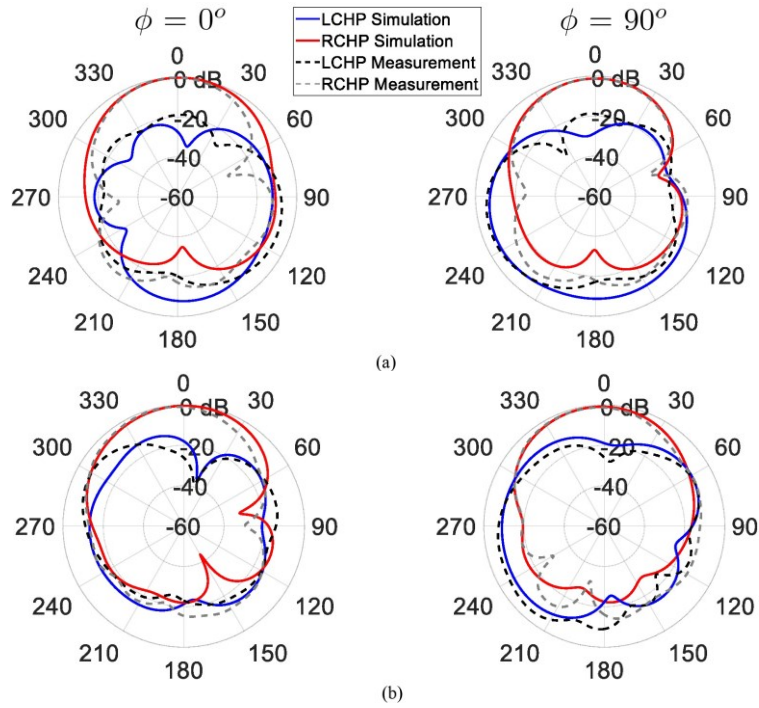


Figure 5.16: Normalized radiation pattern of the proposed antenna while mounted on the inclined stage with the reflector at (a) 1.227 GHz , (b) 1.575 GHz

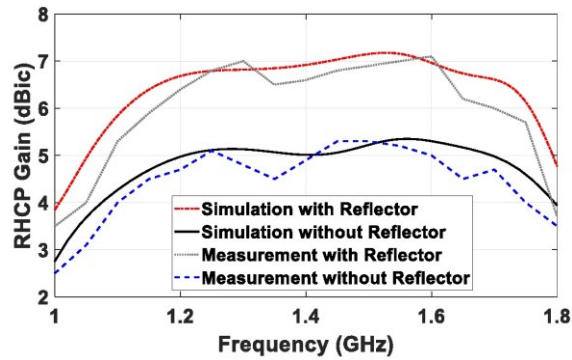


Figure 5.17: RHCP gain of the proposed antenna at $\theta' = 0^\circ$, $\phi = 0^\circ$ while it has been mounted on the stage, with and without the reflector.

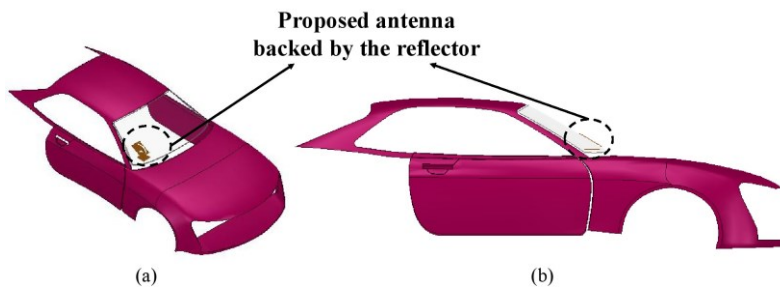


Figure 5.18: Proposed antenna mounted on a car model for re-simulation, (a) isometric view, (b) side view.

5.4.4 Comparison with Previous Works

The proposed antenna is compared with the state-of-art designs in terms of size, type of the antenna, the impedance and axial ratio bandwidth, the tilted angle, and the transparency in Table 5-1. As can be seen, there is no previous work having all the characteristics of wideband or dual-band circular polarization, tilted beam, and transparency at the same time, which is the novelty of the current work.

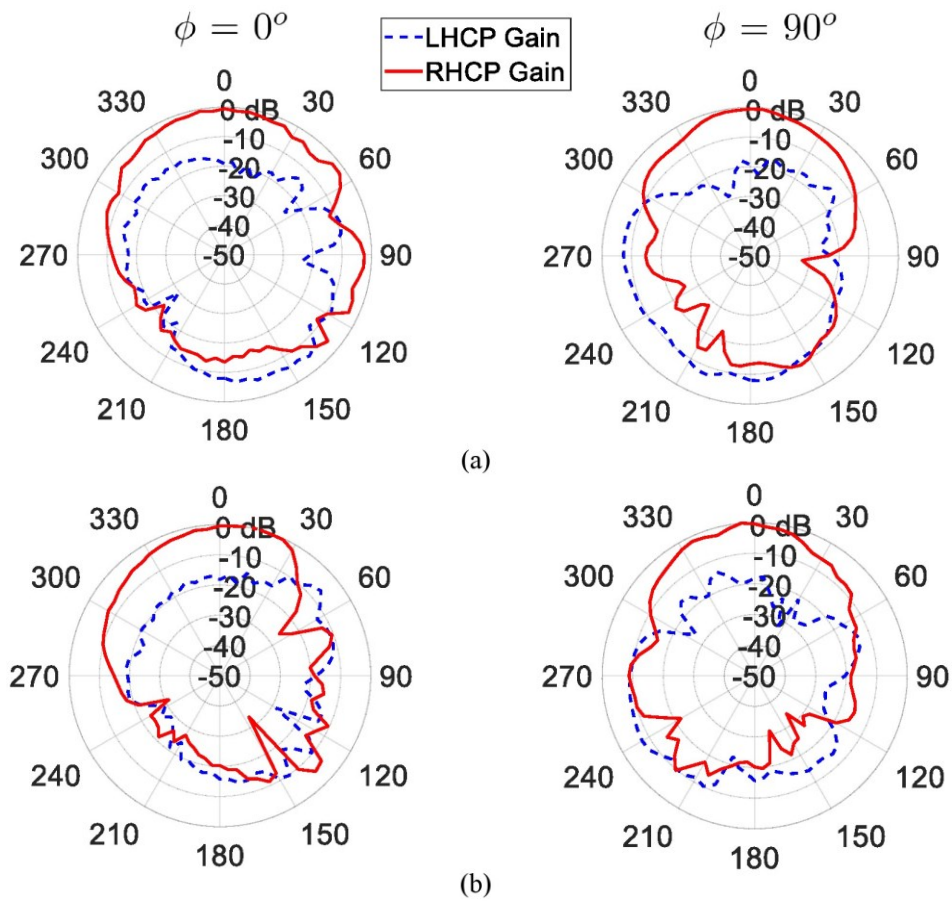


Figure 5.19: Normalized radiation pattern of the proposed antenna while mounted on the windshield of the car model backed by the reflector at (a) 1.227 GHz, (b) 1.575 GHz.

Table 5-1: Comparison between some single, dual, and wideband antennas in literature and the proposed antenna

Design	Size (λ_0^2) ¹	Type ²	IBW	ARBW	Tilted angle	OT ⁴	Peak Gain
			(L,U) ³ (%)	(L,U) ³ (%)	(deg)	(%)	(dB/dBic)
[8]	0.41×0.41	DB	3.7 , 1.2	0.9 , 0.6	NT ⁵	NT ⁶	1.5
[30]	0.4×0.4	SB	10	Not CP	NT	80	5.28
[56]	0.57×0.57	DB	16.9 , 11.4	19.2 , 18	NT	NT	7.9
[57]	0.41×0.41	WB	42	2.1 , 2	NT	NT	8.3
[58]	0.106	DB	0.6 , 0.8	0.6 , 0.8	NT	NT	3.93
[59]	0.53×0.53	WB	40.57	6.56 , 7.74	NT	NT	8.11
[64]	0.28×0.28	SB	3.2	1.7	NT	NT	3.13
[65]	4.52	WB	35	Not CP	NT	100	4
[66]	0.71×0.25	WB	28.5	Not CP	15	94	7
[67]	0.74×0.74	SB	4	10.7	49	NA	8.1
[68]	0.26×0.19	WB	20	25	NT	NT	-1.17
[69]	0.988×0.52	WB	40	6.19	30	NT	8
[70]	0.48×0.175	WB	26 ^{**}	Not CP	NT	>70	6.2
[71]	0.208×0.208	DB	1.25 , 6.9	29.2 , 46.6 [*]	NT	NT	1.73
[72]	1.4×1.36	WB	5.6	Not CP	45	NT	8.75
This Work	0.55×0.39	WB	57	13 , 14	30	88	7

¹ λ_0 is the free space wavelength at the lowest operating frequency

² “SB”: Single-Band, “DB”: Dual-Band, “WB”: Wideband

³ Lower band, Upper band

⁴ Optical Transparency

⁵ Not Tilted

⁶ Not Transparent

* The overlap of IBW and ARBW is just equal to the IBW.

** The 10-dB IBW is obtained from the figures in the paper.

5.5 Conclusion

In this chapter, a novel single-layer CPW-fed transparent circularly polarized antenna with tilted beam designed for GNSS (and specifically for GPS) applications is proposed. It is designed on a Corning® Boro-Aluminosilicate glass with $\epsilon_r=5.5$ and a thickness of 1mm, as the substrate in order to make it transparent. Also, a mesh grid is used in the conductive layer for increasing the transparency of the antenna. Since it is designed for the windshield of vehicles, the beam of the antenna should be tilted to see the sky (LoS) when it is mounted on the windshield. To increase the ratio of maximum RHCP and LHCP gain, a transparent small-size reflector is designed and placed under the antenna. For a better understanding of how the antenna operates, CMA is performed in the desired bandwidth. The antenna 10-dB impedance bandwidth is about 57 % (0.98-1.76 GHz) and 3-dB axial ratio bandwidth of 13 % (1.13 - 1.29 GHz) and 14 % (1.44-1.66 GHz) over the lower and upper frequency bands of interest are obtained, respectively. Additionally, the transparency of the antenna and reflector is 88 % and 95%, respectively. To have more realistic results, an inclined stage is designed using 3D printing to resemble the inclined windshields of vehicles. The measurements are done while the antenna is placed on the stage, with and without the reflector under it. The maximum RHCP gain of the antenna is about 5.1 dBic and 5.3 dBic in L2 and L1 center frequency bands respectively without the reflector, while the RHCP gains increase to 6.75 dBic and 7 dBic at L2 and L1 center frequency bands respectively when the reflector is present. Finally, the simulation of the antenna on a car model is performed for the verification of the results.

6. Future works

As discussed in the previous chapters, different antennas were proposed for GNSS/GPS applications (and possible other applications as well).

As the first potential work, the FBR of the proposed antennas in chapter 4 and 5 could be improved by converting the transparent reflector into a transparent reflector containing a slot, similar to the slotted reflector introduced in chapter 3.

As another potential future works, the optimum tilted angle for high performance of the antenna in different vehicles and different places can be investigated. Since there are many crowded places with high towers and skyscrapers, receiving GNSS/GPS signals may encounter some problems as signals coming from the satellites are hard to be received (or, may not be received) in a line of sight direction, yet to be received with multipath effects. To receive the signals properly, new methods can be developed. One of the methods that could be used for reaching that goal is to design an array of antennas on different regions of a vehicle (could be the front and rear windshields, or side windows of the vehicle). This also will need some new antennas to be designed.

As another suggestion, a novel antenna can be introduced which is going to be mounted on the side mirror of a car. Since the side mirrors are normally curved in most cars, the antenna will be flexible. Moreover, the antenna is transparent and circularly polarized with a high HPBW and 3-dB axial ratio beamwidth. To increase the FBR, a transparent reflector will be designed and placed at the bottom side of the mirror.

Future works

Since most of the devices are becoming more compact nowadays, designing a very compact antenna for vehicular applications is also very demanding and challenging (an example if such antennas are shark fin antennas which are mounted on the vehicles' roofs). Therefore, for the same GNSS/GPS applications as an example, designing very compact antennas with a low height can be introduced, either by putting on the roof or any other places of the cars. This antenna should have a wide impedance and axial ratio bandwidths covering all GNSS/GPS bands, while having an acceptable amount of FBR, which is very challenging for very compact antennas.

The antennas may not be limited to GNSS/GPS applications. By designing wideband antennas with suitable characteristics, other applications can be considered as well. For example, wearable antennas working in 2.4 GHz range can be designed for WLAN/WBAN applications. A key feature of such antennas is their conformability since they need to be mounted on the human body. Another key feature of such antennas is their circular polarization which gives several advantages over LP antennas. Other applications also can be considered.

In summary, considering the characteristics and applications of antennas, many interesting and demanding works can be done.

Bibliography

- [1] N. Koch, "Antennas for automobiles," *New Advances in Vehicular Technology and Automotive Engineering*, p. 410, 2012.
- [2] Kaplan, Elliott and Hegarty, Christopher, *Understanding GPS_GNSS: principles and applications*, Artech house, 2018.
- [3] Liu, Sijia and Li, Du and Li, Boyu and Wang, Feixue, "A compact high-precision GNSS antenna with a miniaturized choke ring," *IEEE Antennas and Wireless Propagation Letters*, vol. 16, pp. 2465--2468, 2017.
- [4] NAVIPEDIA, "esa NAVIPEDIA," 2018.
- [5] Zhou, Yijun and Chen, Chi-Chih and Volakis, John L, "Dual band proximity-fed stacked patch antenna for tri-band GPS applications," *IEEE Transactions on Antennas and Propagation*, vol. 55, no. 1, pp. 220--223, 2007.
- [6] Basilio, Lorena I and Chen, Richard L and Williams, Jeffery T and Jackson, David R, "A new planar dual-band GPS antenna designed for reduced susceptibility to low-angle multipath," *IEEE Transactions on Antennas and Propagation*, vol. 55, no. 8, pp. 2358--2366, 2007.
- [7] Sun, Xiaoye and Zhang, Zhijun and Feng, Zhenghe, "Dual-band circularly polarized stacked annular-ring patch antenna for GPS application," *IEEE Antennas and Wireless Propagation Letters*, vol. 10, pp. 49--52, 2011.
- [8] Hsieh, Wang-Ta and Chang, Tze-Hsuan and Kiang, Jean-Fu, "Dual-band circularly polarized cavity-backed annular slot antenna for GPS receiver," *IEEE Transactions on Antennas and Propagation*, vol. 60, no. 4, pp. 2076--2080, 2012.
- [9] Cai, Yuan-Ming and Li, Ke and Yin, Ying-Zeng and Ren, Xueshi, "Dual-band circularly polarized antenna combining slot and microstrip modes for GPS with HIS ground plane," *IEEE Antennas and Wireless Propagation Letters*, vol. 14, pp. 1129--1132, 2015.

Bibliography

- [10] Yuan, Jiade and Zheng, Jiamin and Chen, Zhizhang David, "A compact meandered ring antenna loaded with parasitic patches and a slotted ground for global navigation satellite systems," *IEEE Transactions on Antennas and Propagation*, vol. 66, no. 12, pp. 6835--6843, 2018.
- [11] Yinusa, Kazeem A, "A dual-band conformal antenna for GNSS applications in small cylindrical structures," *IEEE Antennas and Wireless Propagation Letters*, vol. 17, no. 6, pp. 056--1059, 2018.
- [12] C. A. Balanis, *Antenna theory: analysis and design*, John Wiley & sons, 2016.
- [13] Gao, Steven Shichang and Luo, Qi and Zhu, Fuguo, *Circularly polarized antennas*, John Wiley & Sons, 2013.
- [14] Brookner, Eli and Hall, William M and Westlake, Ruth Hampton, "Faraday loss for L-band radar and communications systems," *IEEE transactions on aerospace and electronic systems*, vol. 4, pp. 459--469, 1985.
- [15] Bickel, SH and Bates, RHT, "Effects of magneto-ionic propagation on the polarization scattering matrix," *Proceedings of the IEEE*, vol. 53, no. 8, pp. 1089--1091, 1965.
- [16] X. L. Bao and M. J. Ammann, "Dual-Frequency Circularly-Polarized Patch Antenna With Compact Size and Small Frequency Ratio," *IEEE Transactions on Antennas and Propagation*, vol. 55, no. 7, pp. 2104-2107}, 2007.
- [17] R. Xu and J. Li, and W. Kun, "A Broadband Circularly Polarized Crossed-Dipole Antenna," *IEEE Transactions on Antennas and Propagation*, vol. 64, no. 10, pp. 4509-4513, 2016.
- [18] H. Nakano and H. Takeda and T. Honma and H. Mimaki and J. Yamauchi, "Extremely low-profile helix radiating a circularly polarized wave," *IEEE Transactions on Antennas and Propagation*, vol. 39, no. 6, pp. 754-757, 1991.
- [19] Mashaal, O Ahmad and Rahim, SKA and Abdulrahman, AY and Sabran, MI and Rani, MSA and Hall, PS, "A coplanar waveguide fed two arm Archimedean spiral slot antenna with improved bandwidth," *IEEE transactions on antennas and propagation*, vol. 61, no. 2, pp. 939--943, 2012.

Bibliography

- [20] Xu, Rui and Li, Jian-Ying and Yang, Jiang-Jun and Wei, Kun and Qi, Yang-Xiao, "A design of U-shaped slot antenna with broadband dual circularly polarized radiation," *IEEE Transactions on Antennas and Propagation*, vol. 65, no. 6, pp. 3217--3220, 2017.
- [21] Ma, Xiaoliang and Huang, Cheng and Pan, Wenbo and Zhao, Bo and Cui, Jianhua and Luo, Xiangang, "A dual circularly polarized horn antenna in Ku-band based on chiral metamaterial," *IEEE transactions on antennas and propagation*, vol. 62, no. 4, pp. 2307--2311, 2014.
- [22] Nakano, H and Aso, N and Mizobe, N and Yamauchi, J, "Low-profile composite helical-spiral antenna for a circularly-polarized tilted beam," *IEEE transactions on antennas and propagation*, vol. 59, no. 7, pp. 2710--2713, 2011.
- [23] Nakano, Hisamatsu and Eto, Jun and Okabe, Yosuke and Yamauchi, Junji, "Tilted-and axial-beam formation by a single-arm rectangular spiral antenna with compact dielectric substrate and conducting plane," *IEEE Transactions on Antennas and Propagation*, vol. 50, no. 1, pp. 17-24, 2002.
- [24] Nakano, H and Toida, M and Okabe, S and Yamauchi, J, "Tilted beam formation using parasitic loop-based plates," *IEEE Antennas and Wireless Propagation Letters*, vol. 15, pp. 1475--1478, 2015.
- [25] Ake, William Dale and Pour, Maria and Mehrabani, Adam, "Asymmetric half-bowtie antennas with tilted beam patterns," *IEEE Transactions on Antennas and Propagation*, vol. 67, no. 2, pp. 738--744, 2018.
- [26] Green, Ryan B and Guzman, Michelle and Izyumskaya, Natalia and Ullah, Barkat and Hia, Supapon and Pitchford, Joshua and Timsina, Ranjita and Avrutin, Vitaliy and Ozgur, Umit and Morkoc, Hadis and others, "Optically transparent antennas and filters: A smart city concept to alleviate infrastructure and network capacity challenges," *IEEE Antennas and propagation magazine*, vol. 61, no. 3, pp. 37--47, 2019.
- [27] H. a. S. M. a. N. K. a. S. T. a. T. T. Inaba, "Vehicle window glass antenna using transparent conductive film". United States Patent 4,849,766, 18 Jul 1989.

Bibliography

- [28] Ito, K and Wu, M, "See-through microstrip antennas constructed on a transparent substrate," *1991 Seventh International Conference on Antennas and Propagation, ICAP 91 (IEE)*, pp. 133--136, 1991.
- [29] Silva, Zachary James and Valenta, Christopher R and Durgin, Gregory, "Optically transparent antennas: A survey of transparent microwave conductor performance and applications," *IEEE Antennas and Propagation Magazine*, 2020.
- [30] Kang, Seok Hyon and Jung, Chang Won, "Transparent patch antenna using metal mesh," *IEEE Transactions on Antennas and Propagation*, vol. 66, no. 4, pp. 2095--2100, 2018.
- [31] Hautcoeur, Julien and Colombel, Franck and Castel, Xavier and Himdi, Mohamed and Cruz, E Motta, "Optically transparent monopole antenna with high radiation efficiency manufactured with silver grid layer (AgGL)," *Electronics Letters*, vol. 45, no. 20, pp. 1014--1016, 2009.
- [32] Gordon, Roy G, "Criteria for choosing transparent conductors," *MRS bulletin*, vol. 25, no. 8, pp. 52--57, 2000.
- [33] Ginley, David S and Perkins, John D, *Handbook of transparent conductors*, Springer, 2011.
- [34] Ghosh, Shuvaraj and Mallick, Arindam and Kole, Arindam and Chaudhury, Partha and Garner, Sean and Basak, Durga, "Study on AZO coated flexible glass as TCO substrate," *2016 IEEE 43rd Photovoltaic Specialists Conference (PVSC)*, pp. 0634--0638, 2016.
- [35] Guan, Ning and Furuya, Hirotaka and Himeno, Kuniharu and Goto, Kenji and Ito, Koichi, "A monopole antenna made of a transparent conductive film," *2007 International Workshop on Antenna Technology: Small and Smart Antennas Metamaterials and Applications*, pp. 263--266, 2007.
- [36] Song, Hyok Jae and Hsu, Tsung Yuan and Sievenpiper, Daniel F and Hsu, Hui Pin and Schaffner, James and Yasan, Eray, "A method for improving the

Bibliography

- efficiency of transparent film antennas," *IEEE Antennas and Wireless Propagation Letters*, vol. 7, pp. 753--756, 2008.
- [37] Colombel, Franck and Castel, Xavier and Himdi, Mohamed and Legeay, G{\'e}rard and Vigneron, Sonia and Cruz, E Motta, "Ultrathin metal layer, ITO film and ITO/Cu/ITO multilayer towards transparent antenna," *IET science, measurement \& technology*, vol. 3, no. 3, pp. 229--234, 2009.
- [38] Hashiba, Junki and Kawajiri, Toru and Shibuya, Ryota and Ishikuro, Hiroki, "Shield effects of metal plate and mesh in wireless power delivery system," *2015 IEEE International Symposium on Radio-Frequency Integration Technology (RFIT)*, pp. 235--237, 2015.
- [39] Yan-Jun, Sun and Hao, Chang and Song-hang, Wu and Yan-Bing, Leng and Li, Wang, "Study on electromagnetic shielding of infrared/visible optical window," *Modern Applied Science*, vol. 9, no. 13, p. 231, 2015.
- [40] Hautcoeur, Julien and Colombel, Franck and Himdi, Mohamed and Castel, Xavier and Cruz, Eduardo Motta, "Large and optically transparent multilayer for broadband H-shaped slot antenna," *IEEE Antennas and Wireless Propagation Letters*, vol. 12, pp. 933--936, 2013.
- [41] Park, Junho and Lee, Seung Yoon and Kim, Jongmin and Park, Dongpil and Choi, Woo and Hong, Wonbin, "An optically invisible antenna-on-display concept for millimeter-wave 5G cellular devices," *IEEE Transactions on Antennas and Propagation*, vol. 67, no. 5, pp. 2942--2952, 2019.
- [42] Nosrati, Mehrdad and Tavassolian, Negar, "Miniaturized circularly polarized square slot antenna with enhanced axial-ratio bandwidth using an antipodal Y-strip," *IEEE Antennas and Wireless Propagation Letters*, vol. 16, pp. 817--820, 2016.
- [43] Gyasi, Kwame Oteng and Wen, Guangjun and Inserra, Daniele and Huang, Yongjun and Li, Jian and Ampoma, Affum Emmanuel and Zhang, Haobin, "A compact broadband cross-shaped circularly polarized planar monopole antenna

Bibliography

- with a ground plane extension," *IEEE Antennas and Wireless Propagation Letters*, vol. 17, no. 2, pp. 335--338, 2018.
- [44] Narbudowicz, Adam and John, Matthias and Sibal, Vit and Bao, Xiulong and Ammann, Max J, "Design method for wideband circularly polarized slot antennas," *IEEE Transactions on Antennas and Propagation*, vol. 63, no. 10, pp. 4271--4279, 2015.
- [45] Ghaffarian, Mohammad Saeid and Moradi, Gholamreza and Mousavi, Pedram, "Wide-band circularly polarised slot antenna by using artificial transmission line," *IET Microwaves, Antennas & Propagation*, vol. 11, no. 5, pp. 672--679, 2016.
- [46] Pourahmadazar, Javad and Ghobadi, CH and Nourinia, J and Felegari, Nader and Shirzad, Hamed, "Broadband CPW-fed circularly polarized square slot antenna with inverted-L strips for UWB applications," *IEEE Antennas and Wireless Propagation Letters*, vol. 10, pp. 369--372, 2011.
- [47] Zhou, Shui-Wei and Li, Ping-Hui and Wang, Yang and Feng, Wei-Hua and Liu, Zong-Quan, "A CPW-fed broadband circularly polarized regular-hexagonal slot antenna with L-shape monopole," *IEEE antennas and wireless propagation letters*, vol. 10, pp. 1182--1185, 2011.
- [48] Jan, Jen-Yea and Pan, Chien-Yuan and Chiu, Kuo-Yung and Chen, Hua-Ming, "Broadband CPW-fed circularly-polarized slot antenna with an open slot," *ieee transactions on antennas and propagation*, vol. 61, no. 3, pp. 1418--1422, 2012.
- [49] Xue, Hai-Gao and Yang, Xue-Xia and Ma, Zhewang, "A novel microstrip-CPW fed planar slot antenna with broadband and circular polarization," *IEEE Antennas and Wireless Propagation Letters*, vol. 14, pp. 1392--1395, 2015.
- [50] Ullah, Ubaid and Koziel, Slawomir, "A geometrically simple compact wideband circularly polarized antenna," *IEEE Antennas and Wireless Propagation Letters*, vol. 18, no. 6, pp. 1179--1183, 2019.
- [51] Ding, Xiaoxiang and Zhao, Zhiqin and Yang, Yaohui and Nie, Zaiping and Liu, Qing Huo, "A compact unidirectional ultra-wideband circularly polarized

Bibliography

- antenna based on crossed tapered slot radiation elements," *IEEE Transactions on Antennas and Propagation*, vol. 66, no. 12, pp. 7353--7358, 2018.
- [52] Bilgic, MM and Yegin, K, "Modified annular ring antenna for GPS and SDARS automotive applications," *IEEE Antennas and Wireless Propagation Letters*, vol. 15, pp. 1442--1445, 2015.
- [53] Yang, Kai-Ping and Wong, Kin-Lu, "Dual-band circularly-polarized square microstrip antenna," *IEEE Transactions on Antennas and Propagation*, vol. 49, no. 3, pp. 377--382, 2001.
- [54] Nayeri, Payam and Lee, Kai-Fong and Elsherbeni, Atef Z and Yang, Fan, "Dual-band circularly polarized antennas using stacked patches with asymmetric U-slots," *IEEE Antennas and Wireless Propagation Letters*, vol. 10, pp. 492--495, 2011.
- [55] Chen, Zhi Ning and Qing, Xianming and others, "Dual-Band Circularly Polarized S-Shaped Slotted Patch Antenna With a Small Frequency-Ratio," *IEEE Transactions on Antennas and Propagation*, vol. 58, no. 6, pp. 2112--2115, 2010.
- [56] Ramirez, M and Parron, J, "Concentric annular ring slot antenna for global navigation satellite systems," *IEEE Antennas and Wireless Propagation Letters*, vol. 11, pp. 705--707, 2012.
- [57] Deng, Changjiang and Li, Yue and Zhang, Zhijun and Pan, Guoping and Feng, Zhenghe, "Dual-band circularly polarized rotated patch antenna with a parasitic circular patch loading," *IEEE Antennas and Wireless Propagation Letters*, vol. 12, pp. 492--495, 2013.
- [58] Zhong, Zeng-Pei and Zhang, Xiao and Liang, Jia-Jun and Han, Chong-Zhi and Fan, Mo-Lin and Huang, Guan-Long and Xu, Wei and Yuan, Tao, "A compact dual-band circularly polarized antenna with wide axial-ratio beamwidth for vehicle GPS satellite navigation application," *IEEE Transactions on Vehicular Technology*, vol. 68, no. 9, pp. 8683--8692, 2019.

Bibliography

- [59] Lee, Sungwoo and Yang, Youngoo and Lee, Kang-Yoon and Hwang, Keum Cheol, "Communication Dual-band Circularly Polarized Annular Slot Antenna With a Lumped Inductor for GPS Applications," *IEEE Transactions on Antennas and Propagation*, 2020.
- [60] Kumar, Kundan and Dwari, Santanu and Mandal, Mrinal Kanti, "Dual-band dual-sense circularly polarized substrate integrated waveguide antenna," *IEEE Antennas and Wireless Propagation Letters*, vol. 17, no. 3, pp. 521--524, 2018.
- [61] Tan, Ming-Tao and Wang, Bing-Zhong, "A dual-band circularly polarized planar monopole antenna for WLAN/Wi-Fi applications," *IEEE Antennas and Wireless Propagation Letters*, vol. 15, pp. 670--673, 2015.
- [62] Wang, Meng-Shuang and Zhu, Xiao-Qi and Guo, Yong-Xin and Wu, Wen, "Miniaturized dual-band circularly polarized quadruple inverted-F antenna for GPS applications," *IEEE Antennas and Wireless Propagation Letters*, vol. 17, no. 6, pp. 1109--1113, 2018.
- [63] Saini, Rohit Kumar and Dwari, Santanu and Mandal, Mrinal Kanti, "CPW-fed dual-band dual-sense circularly polarized monopole antenna," *IEEE Antennas and Wireless Propagation Letters*, vol. 16, pp. 2497--2500, 2017.
- [64] Yuan, Jiade and Zheng, Jiamin and Chen, Zhizhang David, "A compact meandered ring antenna loaded with parasitic patches and a slotted ground for global navigation satellite systems," *IEEE Transactions on Antennas and Propagation*, vol. 66, no. 12, pp. 6835--6843, 2018.
- [65] Sun, Jie and Luk, Kwai-Man, "A wideband low cost and optically transparent water patch antenna with omnidirectional conical beam radiation patterns," *IEEE Transactions on Antennas and Propagation*, vol. 65, no. 9, pp. 4478--4485, 2017.
- [66] Kashanianfard, Mani and Sarabandi, Kamal, "Vehicular optically transparent UHF antenna for terrestrial communication," *IEEE Transactions on Antennas and Propagation*, vol. 65, no. 8, pp. 3942--3949, 2017.

Bibliography

- [67] Zhou, Hengyi and Pal, Arpan and Mehta, Amit and Mirshekar-Syahkal, Dariush and Nakano, Hisamatsu, "A four-arm circularly polarized high-gain high-tilt beam curl antenna for beam steering applications," *IEEE Antennas and Wireless Propagation Letters*, vol. 17, no. 6, pp. 1034--1038, 2018.
- [68] Sundarsingh, Esther Florence and Harshavardhini, A and others, "A compact conformal windshield antenna for location tracking on vehicular platforms," *IEEE Transactions on Vehicular Technology*, vol. 68, no. 4, pp. 4047--4050, 2019.
- [69] Zhang, Wen-Hai and Lu, Wen-Jun and Tam, Kam-Weng, "Circularly polarized complementary antenna with tilted beam based on orthogonal dipoles," *IEEE Antennas and Wireless Propagation Letters*, vol. 17, no. 8, pp. 1406--1410, 2018.
- [70] Tung, Phan Duy and Jung, Chang Won, "Optically transparent wideband dipole and patch external antennas using metal mesh for UHD TV applications," *IEEE Transactions on Antennas and Propagation*, vol. 68, no. 3, pp. 1907--1917, 2019.
- [71] Li, Zheyu and Zhu, Yongzhong and Yang, Hengliang and Peng, Guohao and Liu, Xiaoyu, "A dual-band omnidirectional circular polarized antenna using composite Right/Left-handed transmission line with rectangular slits for unmanned aerial vehicle applications," *IEEE Access*, vol. 8, pp. 100586--100595, 2020.
- [72] Gharaati, Alireza and Goudarzi, Azita and Honari, Mohammad Mahdi and Mirzavand, Rashid and Mousavi, Pedram, "A Novel Single-layer Microstrip Antenna with Tilted Radiation Pattern," *2020 IEEE International Symposium on Antennas and Propagation and North American Radio Science Meeting*, pp. 1951--1952, 2020.
- [73] Garbacz, R and Turpin, R, "A generalized expansion for radiated and scattered fields," *IEEE transactions on Antennas and Propagation*, vol. 19, no. 3, pp. 348--358, 1971.

Bibliography

- [74] Harrington, R and Mautz, J, "Theory of characteristic modes for conducting bodies," *IEEE Transactions on Antennas and Propagation*, vol. 19, no. 5, pp. 622--628, 1971.
- [75] Chen, Yikai and Wang, Chao-Fu, *Characteristic modes: Theory and applications in antenna engineering*, John Wiley & Sons, 2015.
- [76] Han, Min and Dou, Wenbin, "Compact clock-shaped broadband circularly polarized antenna based on characteristic mode analysis," *IEEE Access*, vol. 7, pp. 159952--159959, 2019.
- [77] Xu, Rui and Gao, Steven Shichang and Liu, Jie and Li, Jian-Ying and Luo, Qi and Hu, Wei and Wen, Lehu and Yang, Xue-Xia and Sumantyo, Josaphat Tetuko Sri, "Analysis and Design of Ultrawideband Circularly Polarized Antenna and Array," *IEEE Transactions on Antennas and Propagation*, vol. 68, no. 12, pp. 7842--7853, 2020.
- [78] Lin, Feng Han and Chen, Zhi Ning, "Low-profile wideband metasurface antennas using characteristic mode analysis," *IEEE Transactions on Antennas and Propagation*, vol. 65, no. 4, pp. 1706--1713, 2017.
- [79] Yan, Yi and Ouyang, Jun and Ma, Xiao and Wang, Rui and Sharif, Abubakar, "Circularly polarized RFID tag antenna design for metallic poles using characteristic mode analysis," *IEEE Antennas and Wireless Propagation Letters*, vol. 18, no. 7, pp. 1327--1331, 2019.
- [80] Cabedo-Fabres, Marta and Antonino-Daviu, Eva and Valero-Nogueira, Alejandro and Bataller, Miguel Ferrando, "The theory of characteristic modes revisited: A contribution to the design of antennas for modern applications," *IEEE Antennas and Propagation Magazine*, vol. 49, no. 5, pp. 52--68, 2007.

7. Appendices

7.1 Characteristic Mode Analysis of the Rectangular Slot Antenna

Characteristic modes (CMs) are natural inherent modes of a structure, independent of the geometry and feeding of the design. The idea of characteristic mode analysis was initially introduced in [73] by Garbacz and Turpin, and enhanced by Harrington and Mautz [74]. In recent years, CMA has been very popular among researchers, due to the fact that it is a powerful tool for designing antennas. As a physical interpretation, the CMs are a set of orthogonal modes for expanding any induced currents on a perfect electric conductor (PEC) material, which can be defined as following [75]:

$$J_{total} = \sum_{n=1}^N a_n J_n \quad (5)$$

where a_n are the complex modal expansion coefficients for each mode, and J_n are the characteristic currents. The normalized amplitude of the characteristic currents is called modal significance (MS) which can be shown as:

$$MS_n = \left| \frac{1}{1 + j\lambda_n} \right| \quad (6)$$

obtained by solving the generalized eigenvalue problem:

$$Z = R + jX \quad (7)$$

$$XJ_n = \lambda_n R J_n \quad (8)$$

where λ_n are the eigenvalues, R and X are Hermitian real and imaginary parts of the impedance matrix Z, respectively. Also, characteristic angle (CA) which represents

Appendices

the phase angle between a characteristic current and the associated characteristic field is defined as:

$$CA = 180^\circ - \arctan(\lambda_n) \quad (9)$$

CMA is used for two main purposes. The first purpose of using CMA is to identify the resonance frequencies and capability of the antenna to produce a wide impedance bandwidth. A resonance occurs when the eigenvalue is equal to zero ($MS=1$). Second, it is used as a tool to identify how to produce a wide CP bandwidth. For having a circular polarization, two orthogonal modes should be excited simultaneously with a 90° phase difference. These modes should have the following requirements [76], [77]:

- 1) The MSs should be the same, which means $MS_1 = MS_2$.
- 2) The CAs should have a 90° phase delay, which means $|CA_1 - CA_2| = 90^\circ$.
- 3) The directivities should be the same at the desired angle.
- 4) The current distribution of the two modes should be orthogonal.

With this in mind, CMA is first performed for Ant2. The modal significance and characteristic angles of the first six modes are demonstrated in Fig. 7.1 (a) and (b), respectively. As can be seen, mode 2 is at resonance near 1.4 GHz, modes 3 and 4 are at resonance at 2 GHz, and modes 5 and 6 are near resonance at 2.5 GHz. However, from Fig. 4.5 (a), it is obvious that the antenna is not matched to a 50Ω input. Since the CMA shows the potential resonance frequencies, Ant2 should be modified in such a way that the antenna matches a 50Ω input feedline. Moreover, modes 2 and 4 have the same MS values at 1.75 GHz, while having 64 degrees of phase difference. Since the directivities of the two modes are at the same angle (boresight in the new coordinate system), circular polarization can occur at this frequency. The same

Appendices

scenario applies to 2.35 GHz where modes 4 and 6 meet. However, the axial ratio of Ant2 is still high in the entire bandwidth, since the magnitude ratio and phase difference of E_x and E_y are not appropriate. To make the antenna CP, some changes should be made in the design of the slots. To see where these changes must be made, the summation of surface current magnitudes of modes 2 and 4, and the corresponding far-field radiation pattern at 1.75 GHz are plotted in Fig. 7.1 (c), and the same ones for modes 4 and 6 at 2.35 GHz are plotted in Fig. 7.1 (d), respectively. The summation of the surface currents show the regions where the magnitudes have low values (shown in blue), and regions where the magnitudes have high values (shown in green). This can be a clue and guidance showing the regions where changes should be made (shown with red dash lines) since the magnitude of current is high in those areas. Taking all these into consideration and applying necessary changes result in Ant3.

In the next step, CMA is carried out for Ant3. Like the previous step, we should find the same potential points where the circular polarization is possible for happening. It is worth mentioning that since we are looking for a circular polarization at zenith (in the new coordinate system), the frequencies where two modes have the same MS, an appropriate angle difference, orthogonal surface currents, and the same directivity at the desired angle ($\theta' = 0$) should be found. After checking every possible pair of modes, three pairs of modes have been chosen for more discussion. As can be seen in Fig. 7.2, modes 2 and 4 at 1.75 GHz, modes 3 and 6 at 2.2 GHz and modes 4 and 6 at 2.45 GHz have potential for producing circular polarization.

Appendices

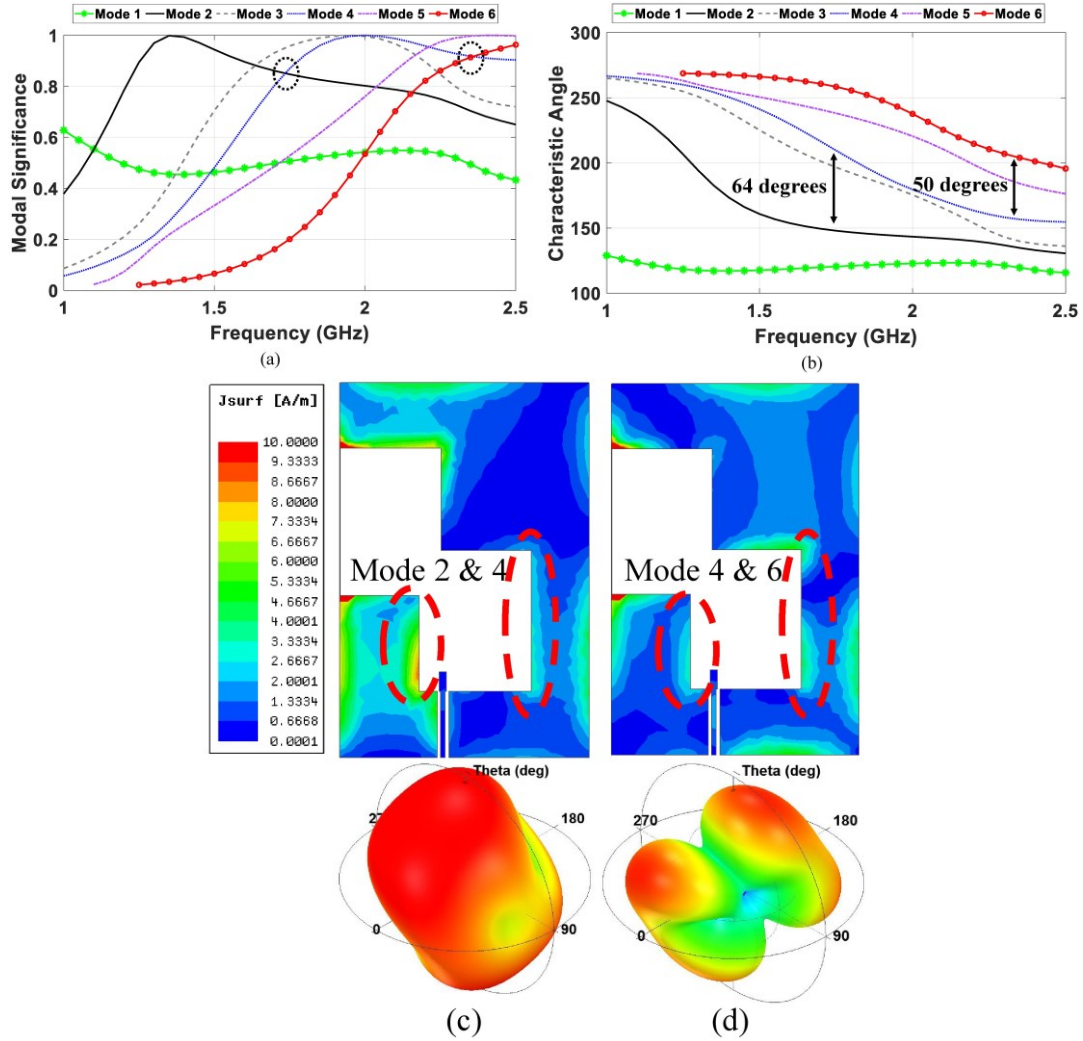


Figure 7.1: Characteristic mode analysis of Ant2 (a) modal significance (b) characteristic angle (c) surface current and directivity of modes 2 and 4 ($\vec{J}_2 + \vec{J}_4$) at 1.75 GHz (d) surface current and directivity of modes 4 and 6 ($\vec{J}_4 + \vec{J}_6$) at 2.35 GHz.

The characteristic angle difference for these three pairs of modes are 64° , 67° , and 38° , respectively. Also, the far-field radiation patterns for the summation of each pair has an acceptable directivity at zenith. This can be verified by plotting the axial ratio of the antenna against the frequency (see Fig. 4.5 (b)). The surface current summation of each pair and corresponding far-field radiation patterns are depicted in Fig. 7.2 (c) to (e). Finally, to match the antenna to a 50Ω input, the surface currents magnitudes

Appendices

for three modes which are at resonance in different frequencies are demonstrated in Fig. 7.3. The regions shown with red dash line can be a hint for making a perturbation at the edges where the currents are higher than other regions. Hence, similar to matching circuits, some perturbations have been added to the antenna, leading to Ant4. Notably, since the CMA is just performed for the PEC radiator without any substrate and feeding, there might be some shifts in the desired frequencies, as can be seen in the CMA results.

In the final step, CMA is performed for both Ant4 and the proposed antenna and since the results are almost the same, only the results of the proposed antenna are displayed (except the surface currents). Ant4 is turned into the proposed antenna by applying mesh grid throughout the design, making it transparent. The mesh grid pattern is almost uniform throughout the structure, except in some regions where the mesh elements cannot fit into the design.

The MS and CA of the proposed antenna are illustrated in Fig. 7.4 (a) and (b), respectively. As can be seen in Fig. 7.4 (a), mode 2 is near 1 at 1.22 GHz, mode 3 and 4 are near 1 at around 1.6 GHz, suggesting resonances at 1.22 GHz and 1.6 GHz, which can be verified by the reflection coefficient of the proposed antenna (see Fig. 4.5 (a)). In addition, as stated earlier, for having a circular polarization, two orthogonal modes should meet four requirements.

The first one is to have equal MS value. Therefore, we should look for the frequencies in which two modes have equal values. For this, 1.5 GHz, and 1.85 GHz are chosen.

Appendices

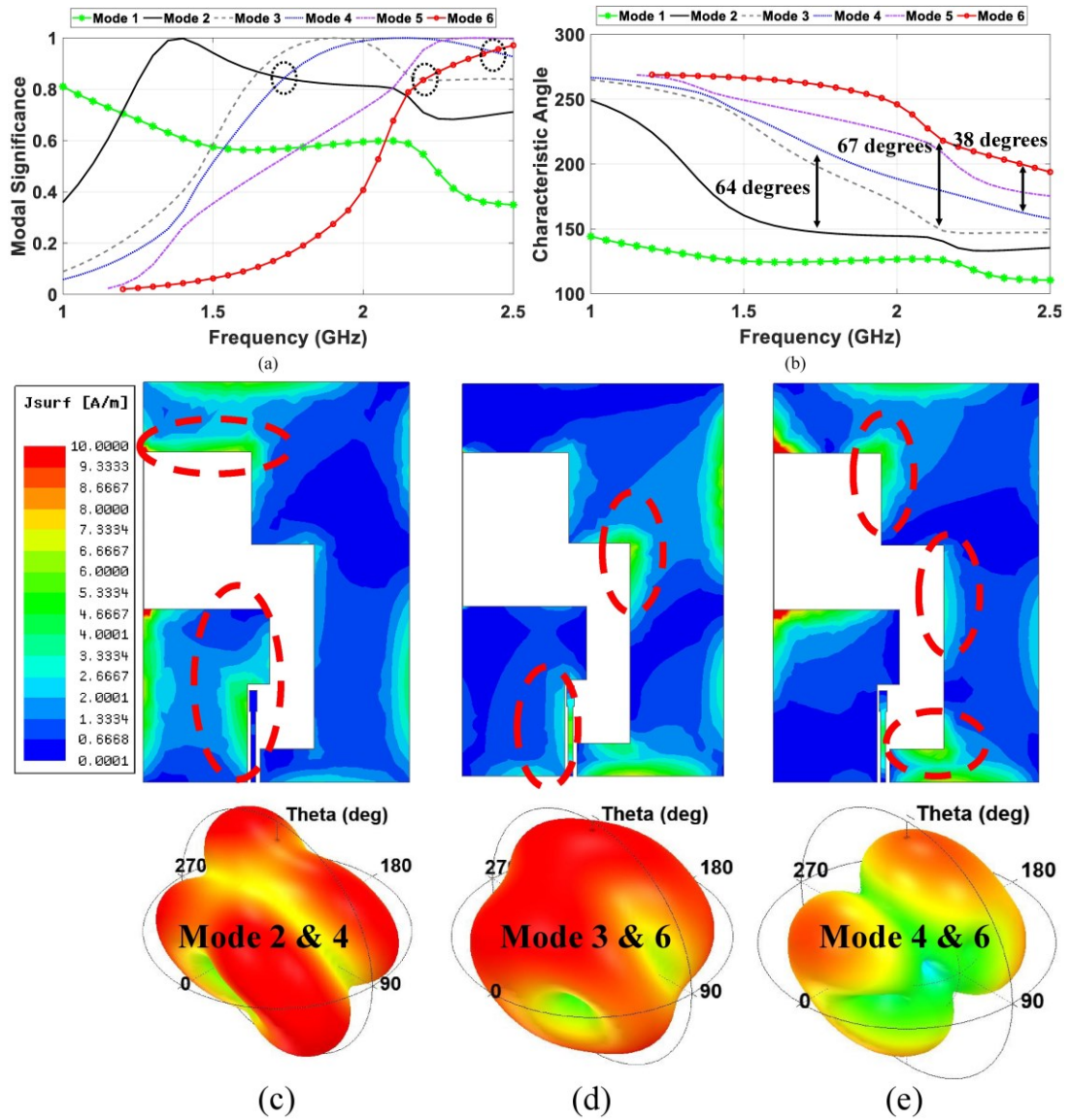


Figure 7.2: Characteristic mode analysis of Ant3, (a) modal significance (b) characteristic angle (c) surface current and directivity of mode 2 and 4 ($\vec{J}_2 + \vec{J}_4$) at 1.75 GHz, (d) surface current and directivity of mode 3 and 6 ($\vec{J}_3 + \vec{J}_6$) at 2.2 GHz (e) surface current and directivity of mode 4 and 6 ($\vec{J}_4 + \vec{J}_6$) at 2.45 GHz.

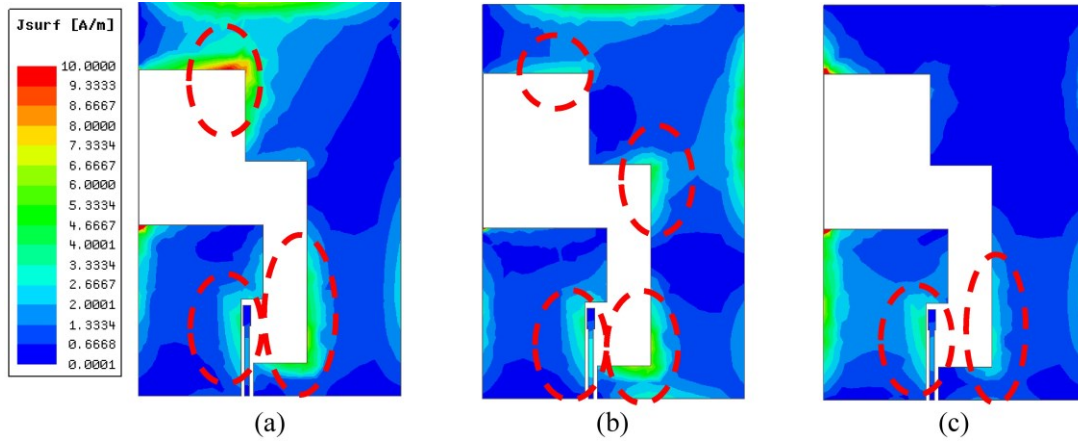


Figure 7.3: Surface current of three different modes of Ant3 at their resonance frequencies, (a) mode 2 at 1.4 GHz (b) mode 3 at 1.9 GHz (c) mode 4 at 2.1 GHz.

Secondly, the CAs should have around 90 degrees of phase delay. As shown in Fig. 7.4 (b), the CA of modes 2 and 4 have 80° phase difference which is capable of producing CP. Also, at 1.85 GHz, the phase difference between modes 4 and 6 is about 85° , all making the antenna potential of producing circular polarization. Thirdly, the directivity of each two orthogonal mode should be the same in the desired angle. In Fig. 7.5, far-field radiation patterns of different desired modes at different frequencies are depicted. All far-field patterns show directivities maximum at $\theta' = 0$, which is the desired angle. Finally, the surface currents for the modes at different frequencies are demonstrated in Fig. 7.6, showing the orthogonality of each pair of modes at the desired frequency. Since the only difference between Ant4 and the proposed antenna geometries is in their transparency and applied mesh grid, the surface current of Ant4 is displayed instead of the proposed antenna.

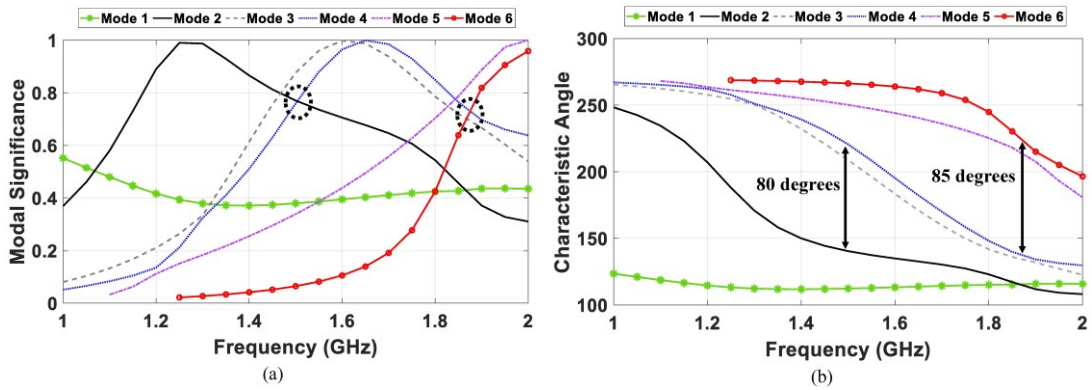


Figure 7.4: Characteristic mode analysis of the proposed antenna, (a) modal significance (b) characteristic angle (CA unit is in degree).

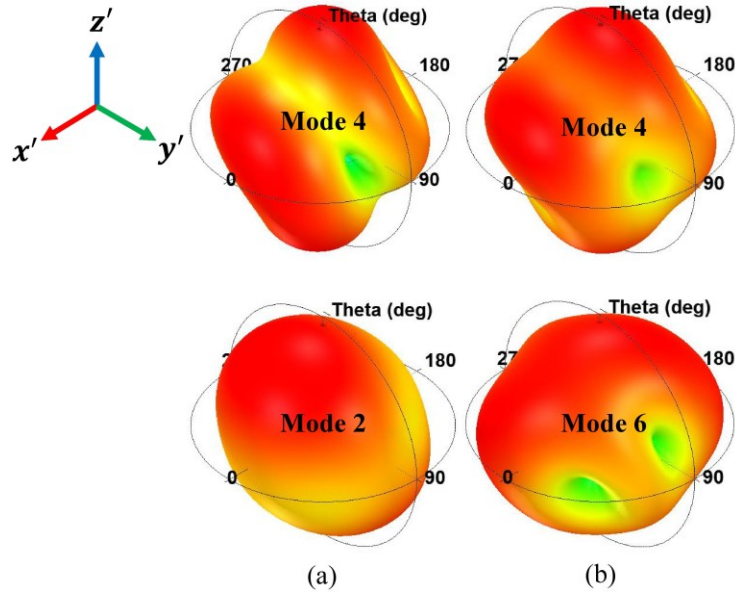


Figure 7.5: Far-field radiation pattern of the different modes of proposed antenna at three different frequencies, (a) 1.5 GHz (b) 1.85 GHz.

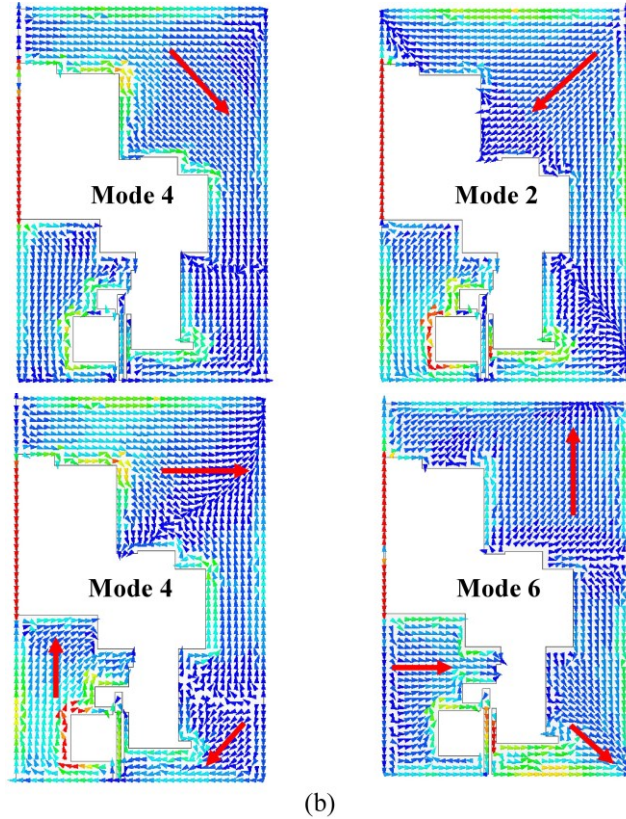


Figure 7.6: Surface currents of different modes of Ant4 at three different frequencies, (a) 1.5 GHz (b) 1.85 GHz.

7.2 Characteristic Mode Analysis of the Spiral Slot Antenna

For a better understanding of how the antenna works, the CMA of the proposed antenna is carried out. Since the focus of this part is not on the theory of the antenna and how it is obtained through the development stages, the CMA for each step is not discussed here, though performed for each step of antenna development for realizing the proposed antenna. As a brief explanation, CMA is carried out for Ant1 and by observing the MS and CA, it is concluded that the antenna has a potential for a

Appendices

wideband impedance bandwidth. Also, the design is capable of producing circular polarization by adjusting the magnitude ratio and phase difference of two orthogonal field components E_x and E_y , or in other words for CMA, the MS and CA of two orthogonal modes. The CMA results suggest that an appropriate excitation can make the antenna wideband in both impedance and axial ratio bandwidth. That is why the L-shaped radiator is added to the design. Furthermore, by observing the CMA results, it can be inferred that for having a wide axial ratio bandwidth in the desired frequency band, a phase difference between E_x and E_y should be added. This will lead to a modification in the L-shaped radiator design, adding some small slots for optimization of the phase difference. All these steps have been done with the help of CMA. From now on, the results are all for the proposed antenna (and the surface current is for Ant3 since the currents of Ant3 can be shown better because of the unity of conductive layer and not being mesh grid). Fig. 7.7 and Fig. 7.8 show the modal significance and the characteristic angle of the first five modes of the antenna in the desired frequency bandwidth, respectively. The MS figure shows the wideband nature of the antenna in terms of impedance bandwidth. The MS of mode 1 is almost 1 at 0.9 GHz, while the MS value of mode 2 and 3 reach near 1 at 1.2 GHz and 1.5 GHz, respectively, and remain almost 1 in a relatively wide bandwidth (400 MHz for each mode). The frequency shift between the full-wave analysis and characteristic mode analysis is because of the fact that CMA is performed only on the conductive PEC layer without considering the effects of dielectric, and feeding structure.

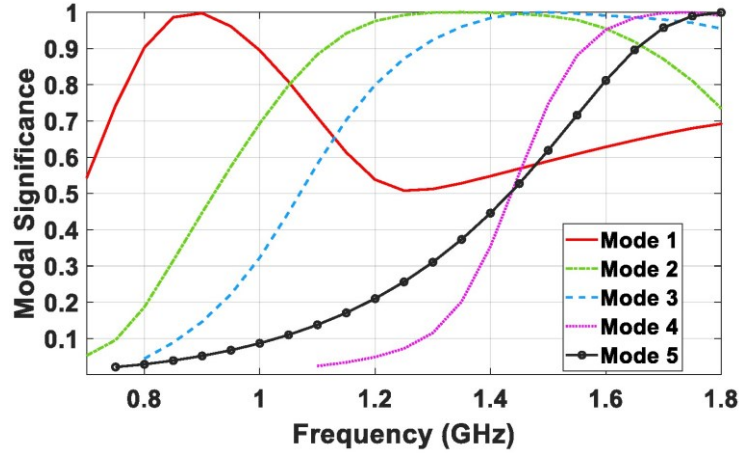


Figure 7.7: Modal significance of the first five modes of the proposed antenna.

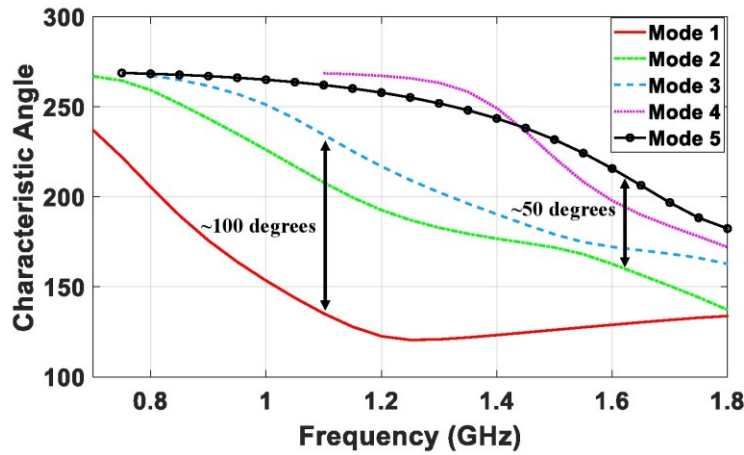


Figure 7.8: Characteristic angle of the first five modes of the proposed antenna

To show the CP behaviour of the tilted beam antenna, far-field radiation patterns which have the most significance effects in tilting the beam are considered. As known, a circular polarization is generated when two modes have equal modal significance values with a 90 degrees phase difference [75]. In addition, both modes should be radiating in the same directivity, or causing a considerable impact on the desired elevation angle. As shown in Fig. 7.7, the MS values of mode 1 and 3 are almost equal at 1.15 GHz, with a CA difference of 100 degrees (see Fig. 7.8). Moreover, as illustrated in Fig. 7.9, the far-field radiation pattern of the antenna for modes 1 and 3

Appendices

at 1.15 GHz show a tilted pattern while the contribution of the other modes for the tilted angle is quite low. Hence, at 1.15 GHz, mode 1 and 3 play the most significant role in generating circular polarization at the tilted angle. It should be noted that the far field patterns are obtained in the primary coordinate system, not the new one.

As another example, modes 3 and 5 have equal MS values at 1.65 GHz, having an approximately 50 degrees of characteristic angle phase difference which can be seen in Fig. 7.8 and 7.9, respectively. Looking at the far-field radiation patterns of mode 1 to 5 at 1.65 GHz, only mode 2 and mode 5 have remarkable impacts at tilted angle in elevation plane (see Fig. 7.9). The surface currents of mode 1 and 3 at 1.15 GHz, and mode 2 and 5 at 1.65 GHz are plotted in Fig. 7.10. The arrows show vector sum of the surface currents at that specific region of the antenna. As can be seen, mode 1 and 3 at 1.15 GHz are orthogonal. Also, mode 2 and 5 at 1.65 GHz present nearly 90 degrees difference between the current vectors, showing the orthogonality of the currents which is a requirement of circular polarization. It is worth mentioning that the surface currents have been depicted for Ant3 to show the currents more obvious, since Ant3 and the proposed antenna characteristics are very close to each other, and the only remarkable difference is in terms of transparency.

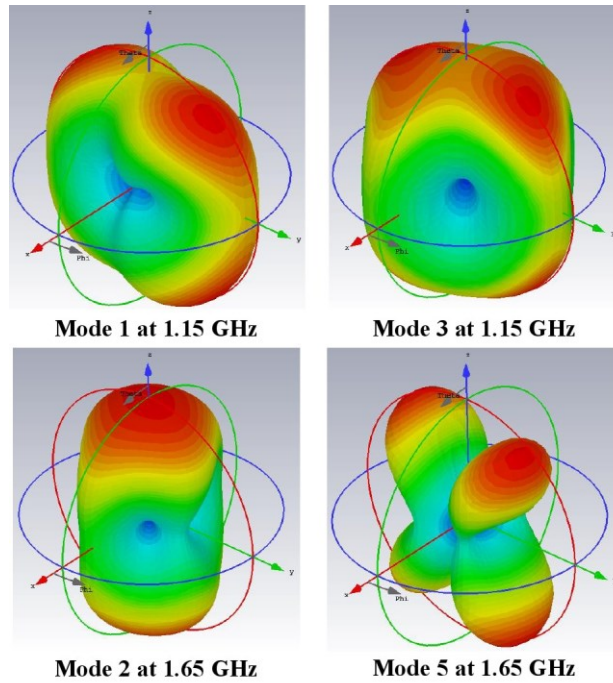


Figure 7.9: Directivity of the proposed antenna in two different frequencies.

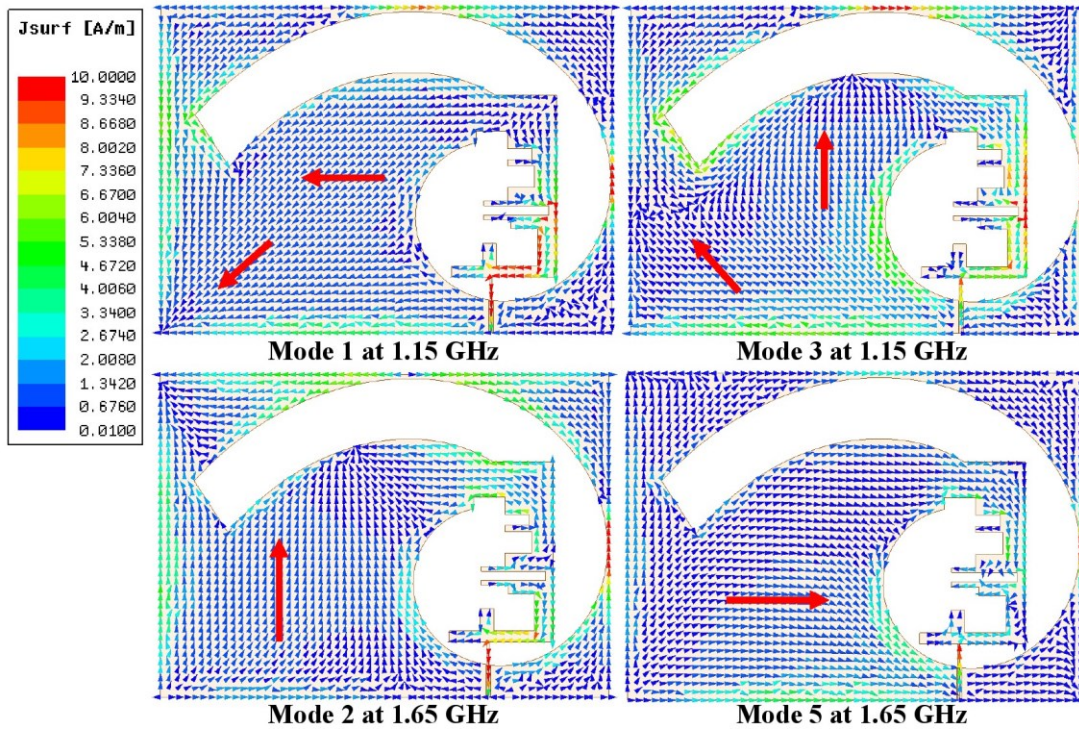


Figure 7.10: Surface currents of mode 1 and mode 3 at 1.15 GHz, and mode 2 and mode 5 at 1.65 GHz of Ant3.

7.3 Conformability Results

7.3.1 Rectangular Slot Antenna

As the windshields are not completely flat, the antenna needs to be conformal. In this case, the conformability of the antenna is investigated through simulations. The more the antenna bends, the worse performance it would have. Fig. 7.11 shows the rectangular slot antenna while it has been curved for a radius curvature of 300 mm, which is definitely more than the radius curvature of regular windshields.

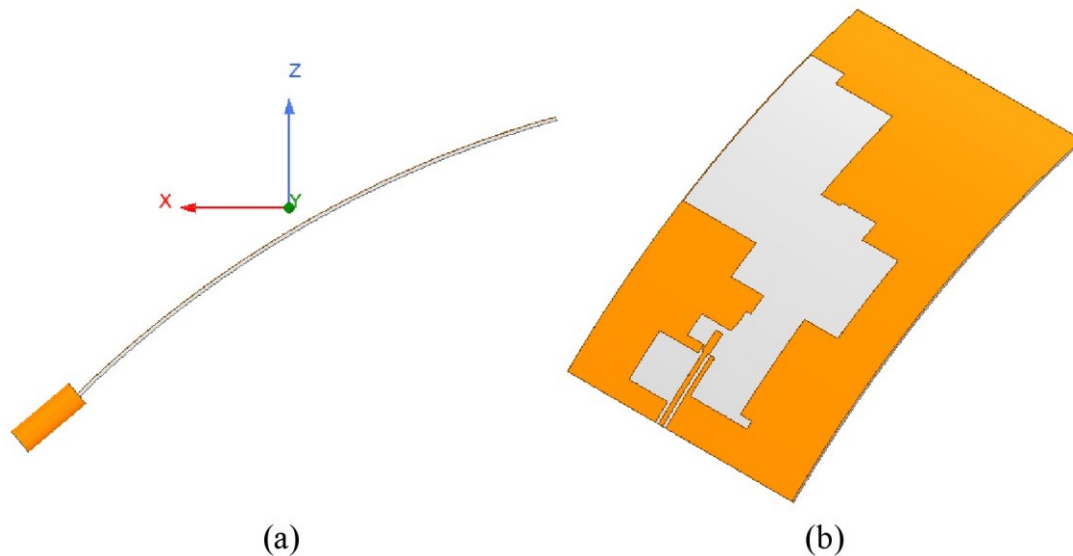


Figure 7.11: Rectangular slot antenna curved with a radius curvature of 300 mm, (a) side view (b) isometric view.

The simulation results of reflection coefficient, axial ratio, and RHCP gain at the second coordinate system ($\theta' = 0^\circ$ and $\phi = 0^\circ$) are illustrated in Fig. 7.12.

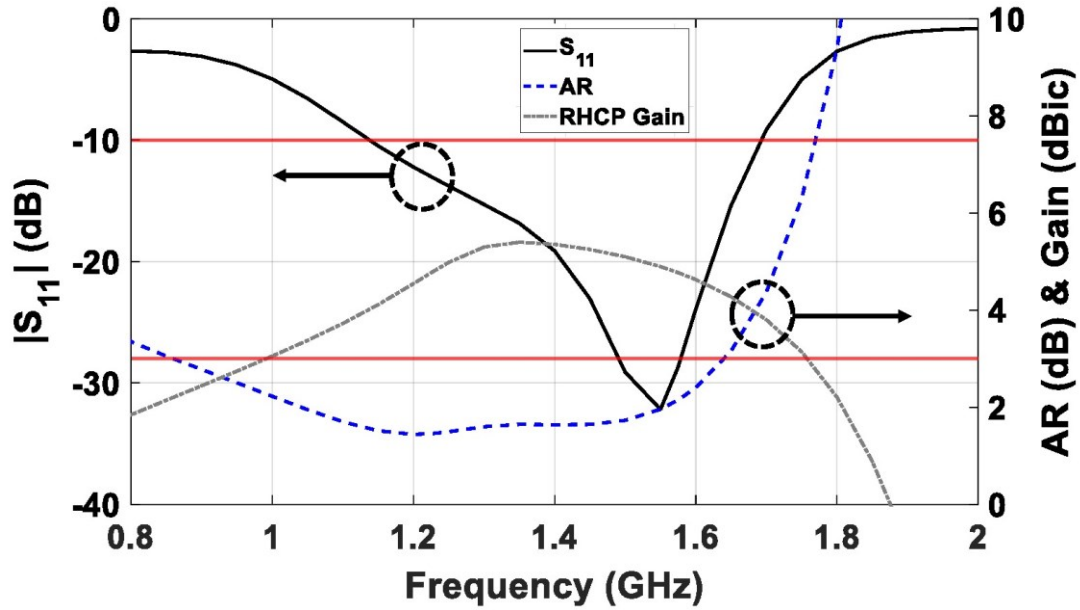


Figure 7.12: Reflection coefficient, axial ratio, and RHCP gain of the curved rectangular antenna in the second coordinate system ($\theta' = 0^\circ$ and $\phi = 0^\circ$), while the antenna is curved with a radius curvature of 300 mm.

As can be seen, the results show that the performance of the antenna in the desired frequency bands are still good and acceptable. Therefore, even by bending the antenna more than enough, the antenna still works properly. The normalized radiation patterns are also depicted in Fig. 7.13 at two GPS L2 and L1 bands.

It is worth mentioning that for conformability results, Ant4 is used instead of the proposed transparent antenna, since the results are very close to each other.

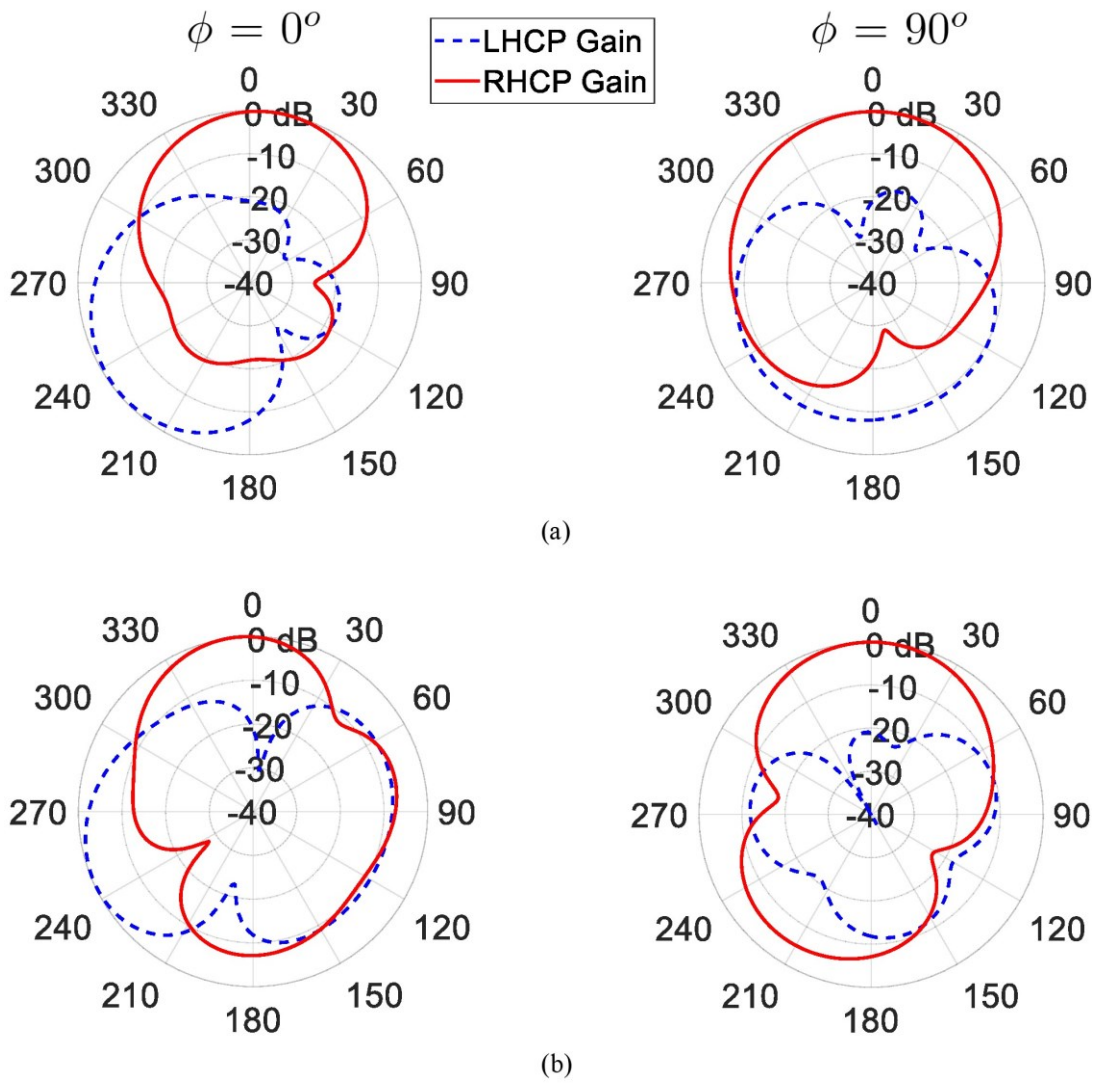


Figure 7.13: Normalized radiation patterns of the curved rectangular slot antenna with a radius curvature of 300 mm at two different planes of $\phi = 0^\circ$ and $\phi = 90^\circ$ (a) 1.227 GHz (b) 1.575 GHz.

7.3.2 *Spiral Slot Antenna*

Same as the rectangular slot antenna, the spiral slot antenna is also investigated in terms of the conformability results. Fig. 7.14 shows the spiral slot antenna while it has been curved for a radius curvature of 200 mm, which is definitely more than the radius curvature of regular windshields.

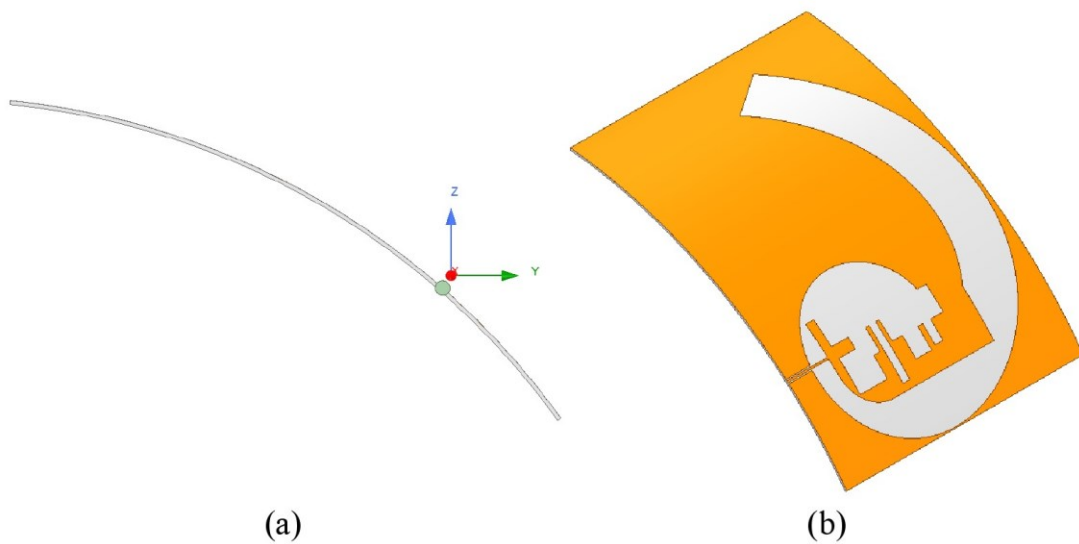


Figure 7.14: Spiral slot antenna curved with a radius curvature of 200 mm, (a) side view (b) isometric view.

The simulation results of reflection coefficient, axial ratio, and RHCP gain at the second coordinate system ($\theta' = 0^\circ$ and $\phi = 0^\circ$) are illustrated in Fig. 7.15.

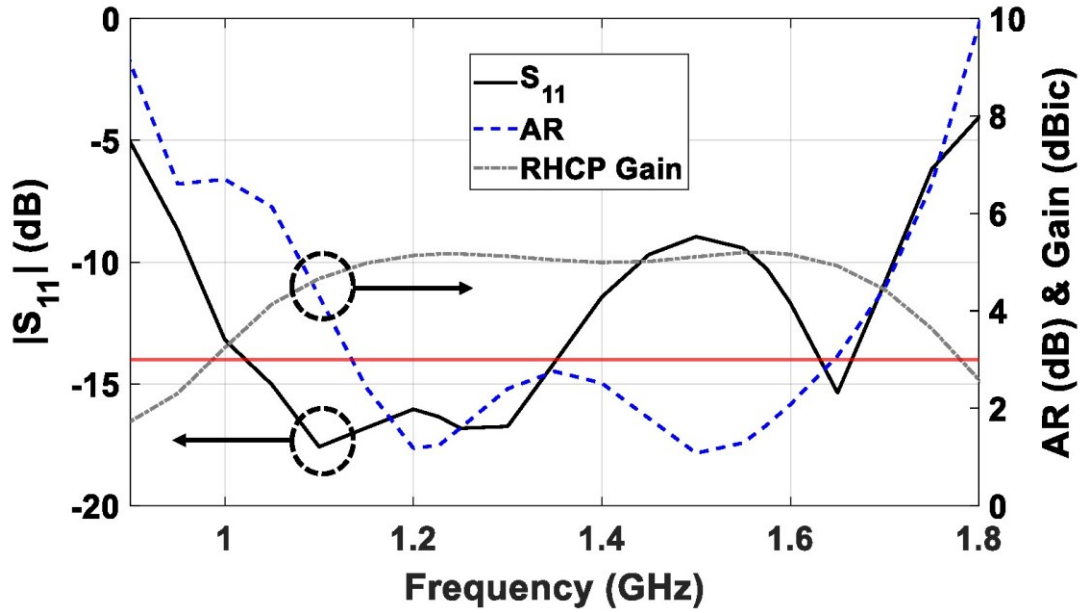


Figure 7.15: Reflection coefficient, axial ratio, and RHCP gain of the curved spiral antenna in the second coordinate system ($\theta' = 0^\circ$ and $\phi = 0^\circ$), while the antenna is curved with a radius curvature of 200 mm.

Again, the results show that the performance of the spiral slot antenna in the desired frequency bands are still good and acceptable. Therefore, even by bending the antenna more than enough, the antenna still works properly. The normalized radiation patterns are also depicted in Fig. 7.16 at two GPS L2 and L1 bands.

Noteworthy, for conformability results, Ant3 is used instead of the proposed transparent antenna, since the results are very close to each other.

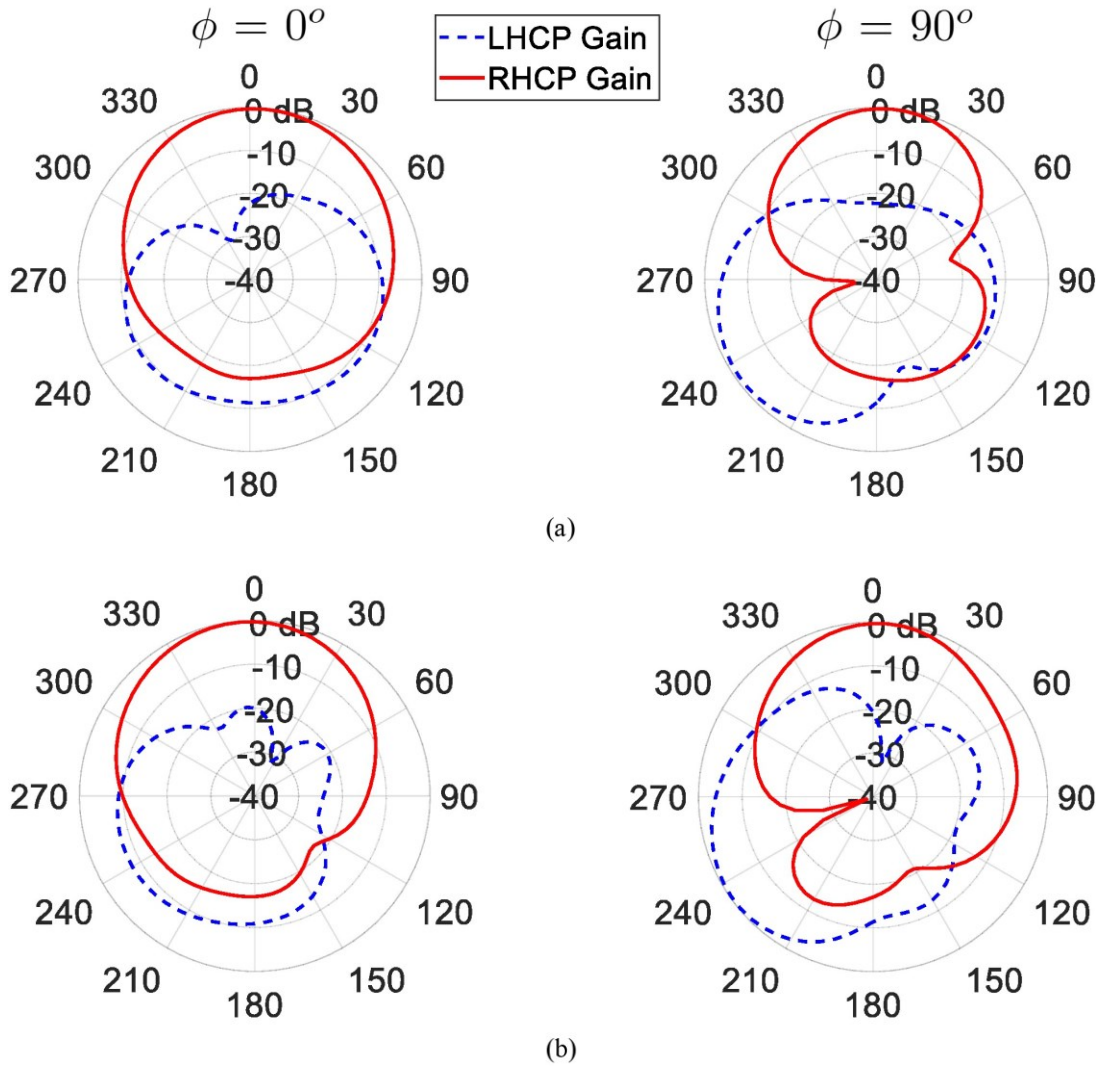


Figure 7.16: Normalized radiation patterns of the curved spiral slot antenna with a radius curvature of 200 mm at two different planes of $\phi = 0^\circ$ and $\phi = 90^\circ$ (a) 1.227 GHz (b) 1.575 GHz.

7.4 Tolerance

7.4.1 Investigation of the Effects of Different Thicknesses and Different Substrate Permittivity Values on Rectangular Slot Antenna

The effects of different thicknesses on the S_{11} , axial ratio value at $\theta' = 0$ and axial ratio beam width for rectangular slot antenna are implemented in Table 7-1.

Table 7-1: Effects of different thicknesses on rectangular slot antenna

	S_{11} @ L2 (dB)	S_{11} @ L1 (dB)	AR @L2 (dB)	AR @ L1 (dB)	AR BeamWidth @L2 (degrees)	AR BeamWidth @L1 (degrees)
h=0.6 mm	-14.89	-14.89	0.86	1.87	25	11
h=0.8 mm	-17.16	-13.99	0.94	1.51	25	14
h=1 mm	-16.72	-13.06	1.10	1.19	26	16
h=1.2 mm	-16.22	-11.79	1.19	1.01	26	16
h=1.4 mm	-15.73	-10.93	1.23	1.11	27	16

Also, the effects of different permittivity values on the S_{11} , axial ratio value at $\theta' = 0$ and axial ratio beam width for rectangular slot antenna are implemented in Table 7-2.

Table 7-2: Effects of different dielectric constants on rectangular slot antenna

	S_{11} @ L2 (dB)	S_{11} @ L1 (dB)	AR @L2 (dB)	AR @ L1 (dB)	AR BeamWidth @L2 (degrees)	AR BeamWidth @L1 (degrees)
$\epsilon_r=5$	-17.45	-14.05	1.00	1.41	26	14
$\epsilon_r=5.2$	-17.18	-13.73	1.04	1.34	26	15
$\epsilon_r=5.4$	-16.93	-13.26	1.08	1.18	26	16
$\epsilon_r=5.5$	-16.72	-13.06	1.10	1.19	26	16
$\epsilon_r=5.6$	-16.64	-12.77	1.13	1.15	26	16
$\epsilon_r=5.8$	-16.51	-12.51	1.15	1.15	27	16
$\epsilon_r=6$	-16.11	-11.63	1.21	1.09	27	16

7.4.2 Investigation of the Effects of Different Thicknesses and Different Substrate Permittivity Values on Spiral Slot Antenna

The effects of different thicknesses on the S_{11} , axial ratio value at $\theta' = 0$ and axial ratio beam width for spiral slot antenna are implemented in Table 7-3.

Table 7-3: Effects of different thicknesses on spiral slot antenna

	S_{11} @ L2 (dB)	S_{11} @ L1 (dB)	AR @L2 (dB)	AR @ L1 (dB)	AR BeamWidth @L2 (degrees)	AR BeamWidth @L1 (degrees)
h=0.6 mm	-13.12	-13.28	0.7	0.56	32	20
h=0.8 mm	-13.36	-12.73	0.4	0.72	30	15
h=1 mm	-13.95	-13.36	0.92	1.42	26	11
h=1.2 mm	-14.89	-14.61	1.52	2.00	21	7
h=1.4 mm	-16.02	-17.80	1.99	2.48	16	3

Also, the effects of different permittivity values on the S_{11} , axial ratio value at $\theta' = 0$ and axial ratio beam width for spiral slot antenna are implemented in Table 7-4.

Table 7-4: Effects of different dielectric constants on spiral slot antenna

	S_{11} @ L2 (dB)	S_{11} @ L1 (dB)	AR @L2 (dB)	AR @ L1 (dB)	AR BeamWidth @L2 (degrees)	AR BeamWidth @L1 (degrees)
$\epsilon_r=5$	-13.49	-12.33	0.62	1.14	29	13
$\epsilon_r=5.2$	-13.71	-12.83	0.70	1.23	28	12
$\epsilon_r=5.4$	-13.86	-13.09	0.86	1.34	26	11
$\epsilon_r=5.5$	-13.91	-13.36	0.92	1.42	26	11
$\epsilon_r=5.6$	-14.00	-13.50	1.00	1.50	26	10
$\epsilon_r=5.8$	-14.26	-13.94	1.12	1.62	25	9
$\epsilon_r=6$	-14.35	-14.54	1.26	1.76	24	8

All the results show that the antennas have a very good tolerance in terms of the substrate thickness and dielectric constant.

7.5 Upper and Lower Hemispheres Energy Division

By using the finite size reflector (100×100 mm in these specific designs), some amount of energy will be reflected to the upper hemisphere. Table 7-5 shows the percentage of energy in upper and lower hemispheres in L2 and L1 center frequency bands for both rectangular and spiral slot antennas. It is worth mentioning that by changing the size of the reflector, the amount of reflected energy would change.

Table 7-5: Amount of energy percentage in upper and lower hemispheres at L2 and L1 center frequency bands.

Hemisphere	Design	reflector	L2 band (1.227 GHz)	L1 band (1.575 GHz)
Upper	Spiral	Yes	82 %	94 %
Lower	Spiral	Yes	18 %	6 %
Upper	Spiral	No	68 %	66 %
Lower	Spiral	No	32 %	34 %
Upper	Rectangular	Yes	78 %	83 %
Lower	Rectangular	Yes	22 %	17 %
Upper	Rectangular	No	63 %	60 %
Lower	Rectangular	No	37 %	40 %